NASA Contractor Report 4323

Prediction of Subsonic Vortex Shedding From Forebodies With Chines

Michael R. Mendenhall and Daniel J. Lesieutre

CONTRACT NAS1-17077
SEPTEMBER 1990

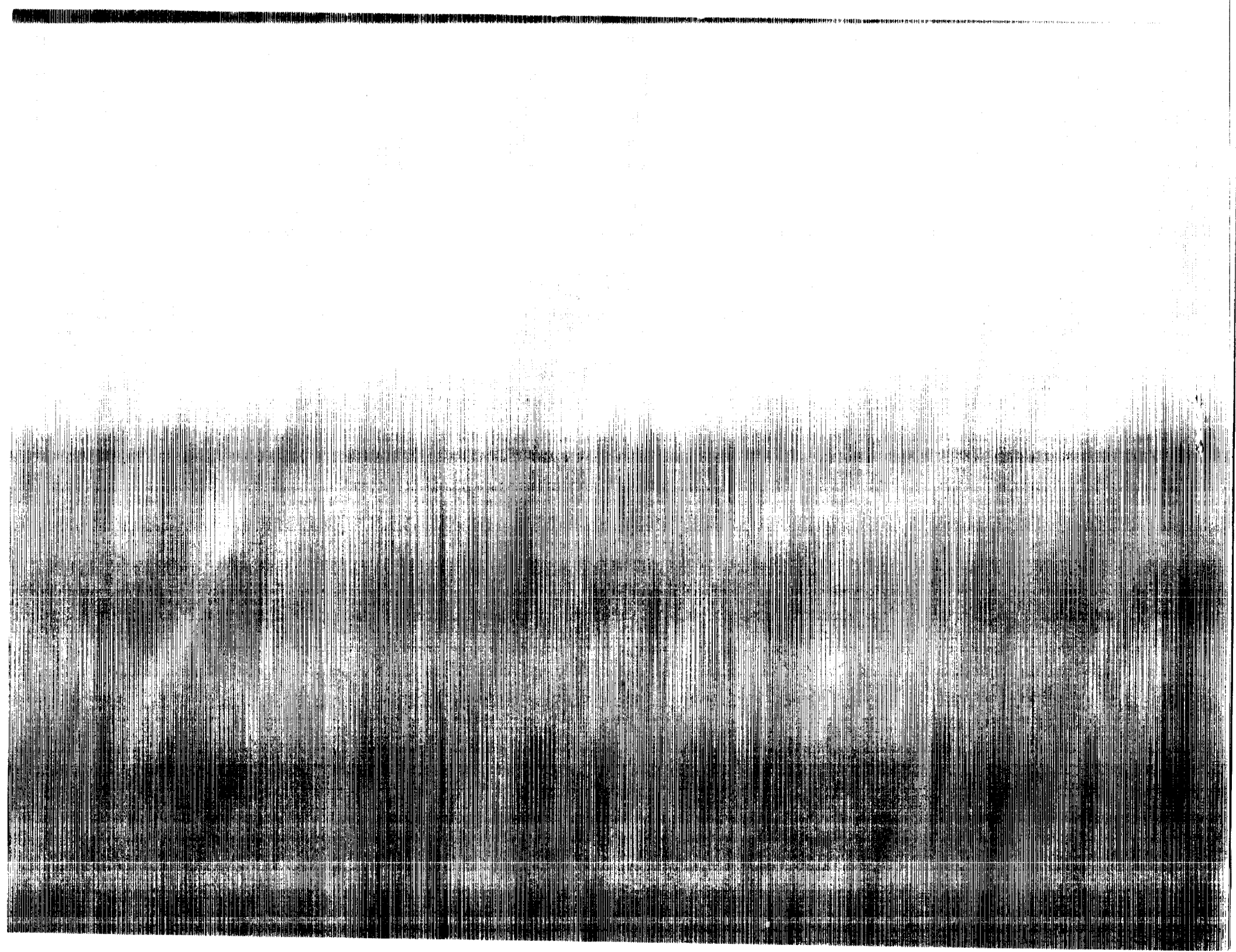

NASA Contractor Report 4323

Prediction of Subsonic Vortex Shedding From Forebodies With Chines

Michael R. Mendenhall and Daniel J. Lesieutre
Nielsen Engineering & Research, Inc.
Mountain View, California

Prepared for
Langley Research Center
under Contract NAS1-17077

National Aeronautics and
Space Administration
Office of Management
Scientific and Technical
Information Division

1990

TABLE OF CONTENTS

PREDICTION OF SUBSONIC VORTEX SHEDDING FROM FOREBODIES WITH CHINES

Michael R. Mendenhall
Daniel J. Lesieutre

Nielsen Engineering & Research, Inc.

SUMMARY

An engineering prediction method and associated computer code VTXCHN to predict nose vortex shedding from circular and noncircular forebodies with sharp chine edges in subsonic flow at angles of attack and roll are presented. Axisymmetric bodies are represented by point sources and doublets, and noncircular cross sections are transformed to a circle by either analytical or numerical conformal transformations. The lee side vortex wake is modeled by discrete vortices in crossflow planes along the body; thus the three-dimensional steady flow problem is reduced to a two-dimensional, unsteady, separated flow problem for solution. Comparison of measured and predicted surface pressure distributions, flow field surveys, and aerodynamic characteristics are presented for noncircular bodies alone and forebodies with sharp chines.

INTRODUCTION

Current flight vehicle applications requiring high aerodynamic performance can involve a variety of noncircular body shapes in subsonic flow at high angles of attack and nonzero roll angles. When these bodies have sharp edges, chines, or wing leading edge extensions, for example, separation is fixed at the sharp edge, and the lee side vortex wake is different from the traditional wake formed by smooth body separation vortices. As in the case of smooth bodies, the chine-body vortex shedding characteristics are directly influenced by the body cross-sectional shape and the local flow conditions. It is desirable to model the lee side vortex wake by means of a rational method capable of considering a variety of body shapes over a wide range of incidence angles and Mach numbers up to the critical speed. It is important that the separation vortex wake-induced effects on the nonlinear aerodynamic characteristics of the configuration be handled properly with a method which correctly represents the physical characteristics of the flow field.

The phenomena of interest are the sheets of vorticity formed when the fluid flow separates from the sharp edges on both sides of the body (Fig. 1). At moderate angles of incidence, the vorticity rolls up into a symmetrical vortex pair, but at higher angles, the vorticity becomes asymmetric and bursting occurs. These latter phenomena are beyond the scope of the current method presented herein.

A method to predict vortex shedding flow phenomena from smooth bodies, both circular and noncircular bodies in subsonic flow, is described in References 1 and 2. The extension of the prediction method to supersonic flow is described in Reference 3. The purpose of this report is to describe an engineering prediction method and associated computer code developed to calculate the nonlinear aerodynamic characteristics and flow fields of noncircular bodies with sharp edges at moderate angles of attack at speeds up to the critical speed. This prediction procedure is based on an extension of the previous methods for smooth bodies (Ref. 1).

The objectives of the method are to use a three-dimensional, attached flow, potential method to represent the body and a two-dimensional, incompressible, separated flow model to calculate the lee side vortex shedding from the body alone at angle of attack and angle of roll. The predicted pressure distribution on the body under the influence of the free stream and the separation vortex wake is used to calculate the aerodynamic loads on the body. Conformal mapping techniques are used to transform noncircular cross sections to a circle for calculation purposes.

The following sections of this report include a discussion of the approach to the problem and a description of the analysis and flow models required to carry out the calculation. The prediction method is evaluated through comparison of measured and predicted results on a variety of body shapes, including elliptical cross sections and forebodies with chines. A user's manual for the computer code is also included. The manual consists of descriptions of input and output and sample cases.

LIST OF SYMBOLS

a	horizontal half axis length of elliptic cross section
A_k	coefficients of conformal transformation, Eq. (8)
b	vertical half axis length of elliptic cross section
c_f	skin-friction coefficient, Eq. (71)
c_n	normal-force coefficient per unit length, Eq. (61)
c_y	side-force coefficient per unit length, Eq. (65)
C_A	axial-force coefficient, Eqs. (70) and (74)
C_l	rolling-moment coefficient, Eq. (69)
C_m	pitching-moment coefficient, Eq. (63)
C_n	yawing-moment coefficient, Eq. (67)
C_p	pressure coefficient, Eq. (53)
C_Y	side-force coefficient, Eq. (66)
C_N	normal-force coefficient, Eq. (62)
D	diameter of circular body, or diameter of noncircular body with equivalent cross section area, $D = 2r_{eq}$
G	complex velocity component, Eq. (38)
K	total number of Fourier coefficients used to describe transformation, Eq. (8)
l_{ref}	reference length
L	model length
M_x	rolling moment about the x-axis
M_y	pitching moment about the y-axis
M_z	yawing moment about the z-axis
M_∞	free-stream Mach number
N	normal force

p	local static pressure
p_∞	free-stream static pressure
q_∞	free-stream dynamic pressure, $(1/2)\rho V_\infty^2$
Q	source strength
r	radial distance from a vortex to a field point
r'	radial distance to a point on a noncircular body, Fig. 4
r_c	vortex core radius, Eq. (76)
r_{eq}	equivalent radius of cross section, $(S_c/\pi)^{1/2}$
r_o	radius of circle in transform plane
Re_ξ	Reynolds number based on boundary layer run length and minimum pressure conditions, $U_m \xi/\nu$
S	reference area
S_c	cross sectional area
u,v,w	velocity components in real plane
u_r	axial perturbation velocity component from body, Eq. (10)
U	local velocity
v_R	radial perturbation velocity from body, Eq. (11)
v_θ	vortex-induced velocity, Eq. (75)
V_∞	free-stream velocity
W	complex potential, Eq. (26)
x,y,z	body coordinate system with origin at the nose: x positive aft along the model axis, y positive to starboard, and z positive up
x_m	axial location of center of moments
Y	side force
α	angle of attack

α_c angle between free-stream velocity vector and body axis

β angle of sideslip; also polar angle in σ-plane, Fig. 4; also $(1-M_\infty^2)^{1/2}$

β' local slope of body surface, Fig. 4

γ ratio of specific heats

γ_r exterior angles of body segment for numerical mapping, Eq. (6)

Γ vortex strength

Δx axial length increment

ζ complex coordinate in an intermediate plane, Fig 2(b)

η vertical coordinate in an intermediate plane, Fig. 2(b)

θ polar angle in ν-plane, Fig. 2(a)

ν complex coordinate in circle plane, Fig. 2(a); also kinematic viscosity

ξ run length, Eqs. (58) and (59); or lateral coordinate in an intermediate plane, Fig. 2(b)

ρ free-stream density

σ complex coordinate in real plane, Fig. 2(a)

τ,λ lateral and vertical coordinates in circle plane, Fig. 2(a)

ϕ roll angle

Φ velocity potential in real plane

ψ stream function in real plane

Subscripts and Superscripts

$(\bar{\ })$ conjugate of complex quantity

$(\ )_m$ vortex m

$(\ )_{cp}$ center of pressure

$(\ )'$ incompressible quantity; or surface values in Fig. 4

GENERAL APPROACH

Smooth forebodies of missiles and aircraft at high angles of attack exhibit distributed vorticity fields on their lee side due to boundary layer fluid leaving the fuselage surface at separation lines. One approach for modeling these distributed vorticity fields has involved the use of clouds of discrete potential vortices. Underlying the basic approach is the analogy between two-dimensional unsteady flow past a body and the steady three-dimensional flow past an inclined body. The three-dimensional steady flow problem is reduced to the two-dimensional unsteady separated flow problem for solution. Linear theory for the attached flow model and slender body theory to represent the interactions of the vortices are combined to produce a nonlinear prediction method. The details of the application of this approach to the prediction of subsonic flow about smooth circular and noncircular forebodies are presented in References 1 and 2. Other investigators have used this approach to successfully model the subsonic flow phenomena in the vicinity of circular cross section bodies (Ref. 4). In spite of the pessimistic outlook, Reference 5 provides a comprehensive review of many of the discrete vortex methods currently available.

The purpose of this report is to document the extension of the subsonic analysis of Reference 1 to predict the vortex shedding characteristics of forebodies with sharp corners or chines. The code VTXCHN was assembled to accomplish the calculation of subsonic vortex shedding from these forebody shapes.

The calculation procedure for smooth bodies is described in detail in Reference 1. The procedure for chined forebodies is carried out in a similar manner. The volume of the body is represented by discrete point sources and doublets, and the strength of the individual singularities is determined to satisfy a flow tangency condition on the body in a nonseparated uniform flow at angle of incidence and roll. Compressibility effects on the body are included by a Gothert transformation which keeps the cross section shape unchanged but stretches the axial body coordinate. Starting at a crossflow plane near the body nose, the pressure distribution on the body is computed using the full compressible Bernoulli equation. The body shape determines the location of separation as the assumption is made that separation occurs at the sharp edge, and the vortex sheet originates at that

point. At the separation points, incompressible vortices with their strengths and positions determined by the requirement that the Kutta condition at the sharp edge be satisfied are shed into the flow field. The trajectories of these free vortices between this crossflow plane and the next plane downstream are calculated by integration of the equations of motion of each vortex, including the influence of the free stream, the body, and other vortices. The pressure and trajectory calculations are carried out by mapping the noncircular cross section shape to a circle using either analytical or numerical conformal transformations. The vortex-induced velocity contribution to the body tangency boundary condition includes image vortices in the circle plane.

At the next downstream crossflow plane, new vortices are shed, adding to the vortex feeding sheet and cloud representing the wake on the lee side of the body. This procedure is carried out in a stepwise fashion over the length of the forebody. The details of the individual methods combined into the prediction method for chines are described in the following sections.

METHODS OF ANALYSIS

Background

Prediction of vortex shedding from configurations with sharp edges at high angles of attack has been an important research area for a number of years because of the dominance of the vortex field on the nonlinear aerodynamics of fighter aircraft and missiles. Most of this work emphasized sharp edged delta wings because of the availability of experimental data and the increasing understanding of the flow phenomena. Unfortunately, forebodies with chines have not experienced this same intensity of study; therefore, the base of knowledge of the flow phenomena is not as well developed.

As part of the current effort, a brief examination of the methods and techniques applied to the prediction of vortex shedding from delta wings and wing-bodies at high angles of attack was made to help put the chine problem into perspective. It is not the purpose of this work to review all the theoretical analyses of delta wings, others have already accomplished

a detailed review (Refs. 5 and 6). It is the purpose of this work to develop an engineering prediction method which does not have some of the limitations and restrictions inherent in some of these available methods, but one which still provides a preliminary design and analysis capability with reasonable accuracy and economy.

An early successful model of the vortex shed from the leading edge of a delta wing is described in Reference 7. In this model, the feeding sheet from the wing leading edge is a straight vortex sheet ending in a concentrated vortex. The effect of the feeding sheet on the crossflow plane is neglected; however, the results are very good for low aspect ratio wings. A more detailed treatment of slender delta wings is presented in Reference 8. In this method, the effect of the feeding sheet is considered, but a conical flow assumption is required which limits the application to low aspect ratios. A more complex vortex model consisting of a cloud of discrete vortices is described in Reference 9 . This model is more flexible in the shape and influence of the feeding sheet and the rolled-up vortex, but it is applicable only to the calculation of the force and center of pressure on thin wings and bodies. This approach has a number of features which make it desirable for bodies with chines, and it is very compatible with the smooth body vortex shedding technique.

The next improvement to the vortex cloud approach is the representation of the wing with a panel method as described in Reference 6. This method has the capability to predict wing pressure distributions under the influence of the shed vorticity, and the capability to consider more complex configurations is available. However, a conical flow assumption is part of the method, and it is not clear if the method is applicable to very small wings or chines. Finally, the use of three-dimensional panel methods to represent both the wing and shed vortex have proved to be very accurate and applicable to a wide variety of configurations (Refs. 10 and 11). These methods require an iterative calculation procedure to converge on the proper vortex strength and position which causes the run times to be excessive in many cases.

The next level of complexity beyond the methods discussed above involves solutions of the Euler and Navier-Stokes equations. There is no doubt that the state of the art in computational fluid dynamics is changing dramatically at this time, and the capability to

handle the forebody with chine is near or even available for research purposes. However, for preliminary design analysis, the CFD methods are still much too expensive and difficult to use. These methods were not considered for the current effort.

Before a prediction method is developed to calculate the vortex shedding from forebodies with chines, a fundamental decision must be made as to whether the configuration is a noncircular body with sharp edges or a body with a low aspect ratio highly swept wing. As discussed later, this distinction affects how the separation vortex wake is perceived and developed. In this effort, in light of the previous work on noncircular bodies, the chine configuration will be considered a noncircular body with a sharp edge; however, for certain purposes (e.g., the starting problem) it will be permitted to have certain characteristics of a wing or leading-edge extension.

General Approach

The development of an engineering method to predict the pressure distributions on arbitrary missile or aircraft forebodies in subsonic flow at high angles of incidence requires the use of a number of individual prediction techniques. In the remainder of this section, the individual methods are described briefly, and the section concludes with a description of the complete calculation procedure.

The following analyses are extensions of the work described in Reference 1; therefore, much of it is repeated from that reference and included here for completeness. The specific modifications required by the chines will be noted as will the minor changes in the method which will affect the prediction of separation from smooth bodies.

Conformal Mapping

The crossflow plane approach applied to arbitrary missile and aircraft forebodies results in a noncircular cross section shape in the presence of a uniform crossflow velocity and free vortices in each plane normal to the body axis. The procedure used to handle the noncircular shapes is to determine a conformal transformation for mapping every point on

or outside the arbitrary body to a corresponding point on or outside a circular body. The two-dimensional potential flow solution around a circular shape in the presence of a uniform flow and external vortices is well known and has been documented numerous places in the literature (Refs. 12 and 13). Thus, the procedure is to obtain the potential solution for the circular body and transform it to the noncircular body. Conformal transformations used are of two distinct types, analytical and numerical.

Analytic transformation.- For very simple shapes like an ellipse [Fig. 2(a)], the transformation to the circle can be carried out analytically as described in Reference 13. For example,

$$\sigma = \nu + \frac{a^2 - b^2}{4\nu} \tag{1}$$

where

$$\sigma = y + iz \tag{2}$$

in the real plane, and

$$\nu = \tau + i\lambda \tag{3}$$

in the circle plane. Two derivatives of the transformation which are required for velocity transformations discussed in a later section follow

$$\frac{d\sigma}{d\nu} = 1 - \left[\frac{a^2 - b^2}{4\nu^2} \right] \tag{4a}$$

$$\frac{d\nu}{dx} = \pm \frac{b \frac{db}{dx} - a \frac{da}{dx}}{2\left[\left(\nu + \frac{a^2 - b^2}{4\nu} \right)^2 - a^2 + b^2 \right]^{1/2}} \tag{4b}$$

A simple wing-body configuration can be considered in the same manner using transformations also available in Reference 13. The transformation for an ellipse is included in the code; therefore, it is shown above for illustrative purposes.

Numerical transformation.- For complex noncircular shapes, the transformation cannot be carried out analytically and a numerical transformation is required. An appropriate numerical transformation procedure which maps the region outside any polygon to the outside of a circle is described in detail in References 14 and 15. A brief summary of the conformal mapping procedure follows.

The sequence of events in the numerical mapping is shown in Figure 2(b). The arbitrary cross section shape of the body in the σ-plane is required to have a vertical plane of symmetry. The transformation of interest will map the region on and outside the body in the σ-plane to the region on and outside a circle in the ν-plane. The first step is a rotation to the ζ-plane so that the cross section is symmetric about the real axis. Thus,

$$\zeta = i\sigma = \xi + i\eta \tag{5}$$

A mapping that transforms the outside of the body in the ζ-plane to the outside of the unit circle is

$$\zeta = \int \frac{1}{\nu^2} \prod_{r=1}^{m} (\nu - \nu_r)^{\gamma_r/\pi} \, d\nu \tag{6}$$

where γ_r are the exterior angles of the m segments of the body cross section. In Equation (6), Π denotes a product series. For a closed body

$$\sum_{r=1}^{m} \gamma_r = 2\pi \tag{7}$$

The transformation implimented is an approximation of Equation (6), and it has the form

$$\sigma = -i \left[\nu + \sum_{k=0}^{K} \frac{r_o^{k+1} A_k}{\nu^k} \right] \tag{8}$$

where the A_k coefficients are obtained through an iterative scheme described in Reference 14, and r_o is the radius of the circle in the ν-plane. The derivatives of the transformation required for velocity calculations described in a later section are

$$\frac{d\sigma}{d\nu} = -i \left[1 - \sum_{k=0}^{K} \frac{r_o^{k+1} kA_k}{\nu^{k+1}} \right] \tag{9a}$$

$$\frac{d\nu}{dx} = \frac{\left[\sum_{k=0}^{K} \frac{(k+1) r_o^{k} A_k}{\nu^k} \right] \frac{dr_o}{dx} + \left[\sum_{k=0}^{K} \frac{r_o^{k+1} dA_k}{\nu^k \, dx} \right]}{- \left[1 - \sum_{k=0}^{K} \frac{r_o^{k+1} kA_k}{\nu^{k+1}} \right]} \tag{9b}$$

The above numerical mapping procedure has been applied to a wide range of general cross section shapes with good success. The mapping works best for shapes which can be considered polygonal, but it does not always handle bodies with negative exterior angles well. More details regarding its use are presented in the description of the code in a later section.

Body Model

A three-dimensional representation of the missile volume is needed for purposes of predicting the absolute pressure coefficient on the surface (Ref. 2). Since the model must be a computationally efficient means of representing both circular and noncircular bodies in compressible flow up to the critical speed, a method using discrete singularities on the body axis is described in this section. As described in Reference 16, a panel method can be used to represent the body surface; however, increased computational requirements make the present approach more desirable for an engineering prediction method in which numerous

calculations may be required for preliminary design and analysis. Though the panel method has advantages for noncircular cross sections, an approximate method using axisymmetric singularities with the conformal transformations described previously has proved to be a reasonable approach for the present method in both surface pressure calculations and vortex tracking.

Circular bodies.- The volume of an axisymmetric body is well represented by a series of point sources and sinks distributed on the axis. A number of models in varying degrees of complexity are available for this task; for example, see References 17-21. For use in VTXCHN, the same discrete source/sink model (Refs. 1 and 20) used for the code VTXCLD was selected for its accuracy, economy, and reliabilty. A new method described in Reference 21 appears to have some promise in modeling axisymmetric bodies, and it should be considered as a possible improvement to the current approach.

Given a series of K point sources and sinks distributed on the missile axis, the induced axial and radial velocities at a point (x,r) are

$$\frac{u_r}{V_\infty \cos\alpha_c} = \sum_{k=1}^{K} \frac{Q_k' \left[\frac{x}{L} - \frac{x_k}{L} \right]}{\left[\left[\frac{x}{L} - \frac{x_k}{L} \right]^2 + \left[\frac{r}{L} \right]^2 \right]^{3/2}} \tag{10}$$

$$\frac{v_R}{V_\infty \cos\alpha_c} = \sum_{k=1}^{K} \frac{Q_k' \left[\frac{r}{L} \right]}{\left[\left[\frac{x}{L} - \frac{x_k}{L} \right]^2 + \left[\frac{r}{L} \right]^2 \right]^{3/2}} \tag{11}$$

where

$$Q_k' = \frac{Q_k}{4\pi L^2 V_\infty \cos\alpha_c} \tag{12}$$

is the dimensionless source strength. Q_k' and x_k are the source strength and axial locations, respectively, of the k-th source. The body surface slope at the j-th body point obtained from Equations (10) and (11) is

$$\left.\frac{dr_{eq}}{dx}\right|_j = \frac{\dfrac{v_{R_j}}{V_\infty \cos\alpha_c}}{1 + \dfrac{u_{r_j}}{V_\infty \cos\alpha_c}} \qquad \text{for } j=1,\ldots,(K-3) \tag{13}$$

Equation (13) produces a set of K-3 linear equations in the unknown source strengths. For a closed body, imposing the condition of the sum of the source strengths to be zero gives the relation

$$\sum_{k=1}^{K} Q'_k = 0 \tag{14}$$

The remaining two conditions are the imposition of stagnation points at the nose and tail of the body. These conditions from Equation (10) are

$$\sum_{k=1}^{K} \frac{Q'_k}{\left[\dfrac{x_k}{L}\right]^2} = 1 \tag{15}$$

$$\sum_{k=1}^{K} \frac{Q'_k}{\left[1 - \dfrac{x_k}{L}\right]^2} = -1 \tag{16}$$

Given the source positions on the missile axis, Equations (13) through (16) comprise the total set of equations to solve for the source strengths. The predicted body shape from the stream function is

$$\psi' = \frac{1}{2}\left(\frac{r}{L}\right)^2 - \sum_{k=1}^{K} Q'_k \left\{ \frac{\left(\dfrac{x}{L} - \dfrac{x_k}{L}\right)}{\left[\left(\dfrac{x}{L} - \dfrac{x_k}{L}\right)^2 + \left(\dfrac{r}{L}\right)^2\right]^{1/2}} \right\} \tag{17}$$

which must be solved by iteration. This procedure is used in the code to calculate the body shape for comparison with the input shape.

The above method has proved successful in modeling a variety of axisymmetric missile bodies; however, some care is required because of the ill-conditioned matrix. Best results are obtained if the discrete sources are spaced at intervals of 60% of the local radius and if the surface slope description of the body is smooth without discontinuities. Boundary conditions are satisfied at points midway between the source locations. The prediction of an appropriate source distribution is an automated part of VTXCLD, and the user must only specify body geometry.

Noncircular bodies.- An appropriate body model for missiles with noncircular cross sections is a surface panel method similar to that described in References 3 and 16; however, the use of a panel model adds significantly to the cost of each computation. For this reason an alternate approach was selected for use with noncircular bodies.

The noncircular body is replaced with an equivalent axisymmetric body having the same cross sectional area distribution as the actual body. There are approximations involved with this model since the induced u-velocity due to noncircular effects is obtained from two-dimensional considerations as described in a later section. This approach is based on a high angle of attack version of slender body theory described in Reference 22. For example, elliptic cross section bodies at $\alpha = 0°$ were modeled with both a panel method and the axis singularity method with correction for noncircular effects, and the surface pressure results are nearly identical. These results are presented in a later section.

Compressibility effects.- The selection of a compressibility correction scheme must take into consideration the configurations of interest and the calculation procedure. For example, vortex sheddirg and tracking is very dependent on cross sectional shape, and numerical transformations add significantly to computation time; therefore, it is advantageous that the compressibility transformation used have no effect on the cross sectional shape. With this guideline and based on similar experiences and requirements

(Ref. 20), a transformation which modifies only the axial coordinate is needed. The Gothert Rule, described in Volume I of Reference 23 and others, is the choice for the compressibility transformation. A brief description of the method included in VTXCHN follows.

The transformation from the compressible (x,y,z) coordinate system to the incompressible (x′,y′,z′) system is

$$x' = x/\beta$$

$$y' = y$$

$$z' = z \tag{18}$$

where

$$\beta = \sqrt{1 - M_\infty^2} \tag{19}$$

As a result of Equation (18), the body slope and angle of attack become

$$\frac{dr'}{dx'} = \beta \frac{dr}{dx} \tag{20}$$

$$\alpha' = \beta\alpha \tag{21}$$

and the velocity fields are related by

$$u = u'/\beta^2$$

$$v = v'/\beta$$

$$w = w'/\beta \tag{22}$$

The vortex shedding scheme in VTXCHN requires that the compressibility correction be applied in a manner slightly different from the usual. At the initiation of the calculation, the actual missile body is transformed to the incompressible shape by the above stretching procedure, and the source distribution is obtained as described previously. The modified incompressible flow conditions are used to calculate the velocity field associated with the body. This velocity field is transformed back to the compressible domain (Eq. (22)) so that it is available for use in vortex tracking and compressible pressure coefficient calculations. The compressible pressure coefficient is used to locate separation and define the shed vorticity. Since the compressibility transformation has no direct effect on the cross sectional shape or the discrete wake vortices, the separation and vortex tracking calculations take place in the compressible domain. No compressibility effects are considered for the vortex-induced velocities.

Vortex Shedding Model

The body vortex shedding model for forebodies with chines is significantly different from the model for smooth bodies described in References 1 and 2. The major difference is in the formation of the discrete vortices themselves. Since the chine is the origin of separation, it is no longer necessary to predict the separation location; however, there are other problems associated with the specification of the vortex characteristics that are different for chines. These will be described in this section.

In the development of the prediction method for forebodies with chines, some improvements to the vortex shedding method for smooth bodies were determined. VTXCHN can be used for smooth bodies, but these improvements are noted, and the recommendation is made that they be included in the code VTXCLD (Ref. 1).

Equations of motion.- The equations of motion of a shed nose vortex in the presence of other free vortices in the vicinity of a body in a uniform stream follow. In the circle (ν) plane, the position of a vortex, Γ_m, is

$$\nu_{m_\Gamma} = \tau_m + i\lambda_m \tag{23}$$

and an image of Γ_m is located at

$$\nu_{m_{-\Gamma}} = \frac{r_o^2}{\bar{\nu}_m} \tag{24}$$

to satisfy the flow tangency condition on the body surface. In the real plane, the position of the vortex Γ_m is

$$\sigma_{m_\Gamma} = y_m + iz_m \tag{25}$$

The complex potential in the real plane is

$$W(\sigma) = \Phi - i\Psi \tag{26}$$

and the corresponding velocity at Γ_m is

$$v_m - iw_m = \frac{dW_m(\sigma)}{d\sigma} = \frac{d}{d\nu}\left[W_m(\sigma) \right]\frac{d\nu}{d\sigma}\Bigg|_{\substack{\sigma=\sigma_m \\ \nu=\nu_m}} \tag{27}$$

The complex potential of Γ_m is not included in Equation (27) to avoid the singularity at that point. The derivative of the transformation required in the above equations is obtained from Equations (4) or (9).

The differential equations of motion for Γ_m in complex form are

$$\frac{d\bar{\sigma}_m}{dx} = \frac{v_m - iw_m}{V_\infty \cos\alpha_c + u} \tag{28}$$

where

$$\bar{\sigma}_m = y_m - iz_m \tag{29}$$

Therefore, the two equations which must be integrated along the body length to determine the trajectory of Γ_m are

$$\frac{dy_m}{dx} = \frac{v_m}{V_\infty \cos\alpha_c + u} \tag{30a}$$

and

$$\frac{dz_m}{dx} = \frac{w_m}{V_\infty \cos\alpha_c + u} \tag{30b}$$

where u is the axial perturbation velocity in the flow field. Details of the calculation of the required velocity components are discussed in the following section.

There are a pair of equations like (30) for each vortex in the field. As new vortices are shed, the total number of equations to solve increases by two for each added vortex. These differential equations are solved numerically using a method which automatically adjusts the step size to provide the specified accuracy.

Velocity Field.- The velocity components at all points in the flow field are needed for pressure calculation and vortex tracking. The following summarizes the procedure for determining the u,v,w-components of velocity from all singularities in the flow field. For purposes of this section, the velocity components required for vortex tracking are shown to illustrate the procedure.

The complex potential in the crossflow (circle) plane consists of the following components.

Crossflow due to α:

$$W_1(\sigma) = -i\nu V_\infty \sin\alpha \tag{31}$$

Crossflow due to β:

$$W_2(\sigma) = -\nu V_\infty \sin\beta \tag{32}$$

Cylinder in α flow (two-dimensional doublet):

$$W_3(\sigma) = i\,(r_o^2/\nu) V_\infty \sin\alpha \tag{33}$$

Cylinder in β flow (two-dimensional doublet):

$$W_4(\sigma) = -\,(r_o^2/\nu) V_\infty \sin\beta \tag{34}$$

Discrete vortices outside a circle:

$$W_5(\sigma) = -i \sum_{n=1}^{N} \frac{\Gamma_n}{2\pi} \ln\,(\nu - \nu_n) \tag{35}$$

Images of discrete vortices:

$$W_6(\sigma) = i \sum_{n=1}^{N} \frac{\Gamma_n}{2\pi} \ln \left(\nu - \frac{r_o^2}{\bar{\nu}_n} \right) \tag{36}$$

Note that the image at the center of the circle as required by the circle theorem is omitted from the potential (Ref. 24). When a vortex is shed from a cylinder, it must leave an equal and opposite circulation on the cylinder. This is contrary to the situation when an external vortex is brought to the cylinder from infinity, in which case, the center image vortex is required. When a vortex or cloud of vortices breaks from the feeding sheet in an asymmetric condition, then it may appear to downstream planes that these vortices did not originate on the body, and the center vortex is required as part of the solution. In most practical missile situations when the shedding is symmetric, the above point is academic to the method.

The next term is that due to a two-dimensional source representing a growing cylinder in the crossflow plane. It is required for the incremental noncircular perturbation effects on the u-velocity to be described later. Note that the axisymmetric body contribution to all velocity components is included through the three-dimensional source/sink distribution described previously in Equations (10) and (11).

Expanding cylinder (two-dimensional source):

$$W_7(\sigma) = r_{eq} \frac{dr_{eq}}{dx} \ln\nu \; V_\infty \cos\alpha \tag{37}$$

The velocity components in the crossflow plane are obtained from the derivative of the complex potential as shown in Equation (27). The total velocity at Γ_m in the crossflow plane is written as

$$\frac{v_m - iw_m}{V_\infty} = G_\alpha + G_\beta + G_n + G_m + G_T + G_r \tag{38}$$

where each term in Equation (38) represents a specific velocity component in the σ-plane corresponding to the appropriate complex potential. The first term, from Equations (31) and (33), represents the uniform flow due to angle of attack.

$$G_\alpha = -i \sin\alpha \left[1 + \left(\frac{r_o}{\nu_m} \right)^2 \right] \left. \frac{d\nu}{d\sigma} \right|_{\sigma=\sigma_m} \tag{39}$$

The second term, from Equations (32) and (34), represents the uniform flow due to angle of yaw.

$$G_\beta = -\sin\beta \left[1 - \left(\frac{r_o}{\nu_m} \right)^2 \right] \left. \frac{d\nu}{d\sigma} \right|_{\sigma=\sigma_m} \tag{40}$$

In compressible flow, the velocity components from Equations (39) and (40) used in the surface pressure calculations include effects of the compressibility transformation described in a previous section.

The next term, from Equations (35) and (36), represents the influence of all vortices and their images, with the exception of Γ_m . When velocity components are required elsewhere in the field, Γ_m is included in the calculation.

$$G_n = i \sum_{n=1}^{N} \frac{\Gamma_n}{2\pi r_o V_\infty} \left[\frac{1}{(v_m/r_o) - (r_o/\bar{v}_n)} - \frac{1}{(v_m/r_o) - (v_n/r_o)} \right]_{n \neq m} \left. \frac{dv}{d\sigma} \right|_{\sigma=\sigma_m} \quad (41)$$

The next term, from Equation (36), is due to the image of Γ_m . This term is required only for vortex tracking purposes.

$$G_m = i \frac{\Gamma_m}{2\pi r_o V_\infty} \left[\frac{1}{(v_m/r_o) - (r_o/\bar{v}_m)} \right] \left. \frac{dv}{d\sigma} \right|_{\sigma=\sigma_m} \quad (42)$$

The fifth term in Equation (38) represents the potential of Γ_m in the σ-plane (Routh's Theorem, Ref. 24) and is written as

$$G_T = -i \frac{\Gamma_m}{2\pi V_\infty} \left[\frac{1}{2}\right] \frac{d}{dv}\left[\frac{dv}{d\sigma}\right]_{\sigma=\sigma_m} \quad (43)$$

The last term in Equation (38) corresponds to the velocity components induced by the three-dimensional source singularities representing the volume effects from Equation (11).

$$G_r = \frac{v_r - iw_r}{V_\infty} \quad (44)$$

where v_r and w_r are appropriate components of v_R.

It has been demonstrated with panel methods that the u-velocity perturbation due to noncircular effects is important in the calculation of surface pressures and flow field velocities (Ref. 16). Since all the singularities in the flow model are two-dimensional, with the exception of the axisymmetric body volume model, it is necessary to calculate the u-velocity components from the complex potentials defined in Equations (31) through (34) and (37). The u-velocity contribution of the vortex field is neglected in the flow field, but it is included in the surface pressure calculation as described in a later section. The following is a description of the calculation of the various components of the u-velocity at any point in the flow field.

The axial velocity, given the complex potential, is

$$u = \frac{d\phi}{dx} = \frac{d}{dx}\left[\text{Real}(W)\right] = \text{Real}\left[\frac{dW}{dx}\right] \tag{45}$$

From Equations (31) through (34), the noncircular contributions to Equation (45) are

$$\frac{dW_1}{dx} = -i\, V_\infty \sin\alpha \frac{dv}{dx} \tag{46}$$

$$\frac{dW_2}{dx} = -V_\infty \sin\beta \frac{dv}{dx} \tag{47}$$

$$\frac{dW_3}{dx} = i\, V_\infty \sin\alpha \left[\frac{2vr_o \frac{dr_o}{dx} - r_o^2 \frac{dv}{dx}}{v^2}\right] \tag{48}$$

$$\frac{dW_4}{dx} = -V_\infty \sin\beta \left[\frac{2vr_o \frac{dr_o}{dx} - r_o^2 \frac{dv}{dx}}{v^2}\right] \tag{49}$$

Since the body source singularities given by Equation (12) are three-dimensional, they contribute an induced axial velocity, u_r, given by Equation (10). However, as noted previously, these axial velocities are axisymmetric, and they exhibit no direct effect of the

noncircular shape. This deficiency can be corrected using the techniques of high angle-of-attack slender-body theory described in Reference 22. An approximation to the perturbation u-velocity due to the growing noncircular shape is described below.

The equivalence rule described in Section 6-4 of Reference 25 states that (1) the flow far away from a general slender body becomes axisymmetric and equal to the flow around an equivalent axisymmetric body, and (2) near the slender general body, the flow is different from that around the equivalent axisymmetric body by a two-dimensional component that is required to satisfy the tangency boundary condition. Or, the difference between the velocity potential for the noncircular body and that for the equivalent body of revolution is equal to the increment of the velocity potential due to the noncircular effect. Thus,

$$\Phi_n - \Phi_{eq} = \Phi_{\Delta n} \tag{50}$$

Applying Equation (45) to Equation (37) for both terms on the left side of Equation (50), remembering that $dv/dx = 0$ for circular cross sections, the contribution due to the growing noncircular forebody becomes

$$\left.\frac{dW_7}{dx}\right|_{\Delta n} = V_\infty \cos\alpha \left[\frac{r_{eq}}{v} \frac{dr_{eq}}{dx} \frac{dv}{dx} \right] \tag{51}$$

This velocity represents the increment in the axial velocity caused by the noncircular shape of the body.

Finally, the u-velocity in the flow field of a noncircular body is calculated by including Equations (46) through (49) and (51) in Equation (45). This approach, though slightly different from that presented in Reference 22, produces results that are in excellent agreement with high angle-of-attack slender-body theory as applied to ellipsoids.

Surface pressure distribution.- The surface pressure distribution on the body is required to calculate the forces on the body and the separation points. The surface pressure coefficient is determined from the Bernoulli equation in the form

$$C_p = \frac{2}{\gamma M_\infty^2} \left\{ \left[1 + \frac{\gamma-1}{2} M_\infty^2 (C_{p_I}) \right]^{\frac{\gamma}{\gamma-1}} - 1 \right\} \tag{52}$$

where

$$C_p = \frac{p - p_\infty}{\frac{1}{2}\rho V_\infty^2} \tag{53}$$

and

$$C_{p_I} = 1 - \left[\frac{U}{V_\infty} \right]^2 - \frac{2\cos\alpha_c}{V_\infty} \frac{d\Phi}{dx} \tag{54}$$

where U is the total velocity (including V_∞), velocity components from Equation (38), and u velocity components from Equations (46) through (49) and (51) at a point on the body.

The last term in Equation (54) represents the axial velocity missing from the two-dimensional vortices representing the shed vortex field. This "unsteady" term in Equation (54), evaluated on the body surface, is

$$\frac{d\Phi}{dx} = \text{Real} \left. \frac{dW(\nu)}{dx} \right|_{r=r_o} \tag{55}$$

The contribution of the discrete vortices in the flow field, using Equation (35) and (36), becomes

$$\frac{d\Phi}{dx} = \sum_{n=1}^{N} \frac{\Gamma_n}{2\pi} \left\{ - \left[\frac{(\tau - \tau_n)\frac{d\lambda_n}{dx} - (\lambda - \lambda_n)\frac{d\tau_n}{dx}}{(\tau - \tau_n)^2 + (\lambda - \lambda_n)^2} \right] \right.$$

$$- \left[\frac{(\tau r_n^2 - \tau_n r_o^2)\left[2\lambda\tau_n \frac{d\tau_n}{dx} + 2\lambda\lambda_n \frac{d\lambda_n}{dx} - r_o^2 \frac{d\lambda_n}{dx} - 2r_o\lambda_n \frac{dr_o}{dx} \right]}{\left(\tau r_n^2 - \tau_n r_o^2 \right)^2 + \left(\lambda r_n^2 - \lambda_n r_o^2 \right)^2} \right]$$

$$\left. + \left[\frac{(\lambda r_n^2 - \lambda_n r_o^2)\left[2\tau\lambda_n \frac{d\lambda_n}{dx} + 2\tau\tau_n \frac{d\tau_n}{dx} - r_o^2 \frac{d\tau_n}{dx} - 2r_o\tau_n \frac{dr_o}{dx} \right]}{\left(\tau r_n^2 - \tau_n r_o^2 \right)^2 + \left(\lambda r_n^2 - \lambda_n r_o^2 \right)^2} \right] \right\} \quad (56)$$

where

$$r_n^2 = \tau_n^2 + \lambda_n^2 \quad (57)$$

There are several options available for the use of the information defined in Equation (56) and in the previous section. Practical aspects of the calculation of pressure coefficients, velocity fields, and vortex trajectories dictate the manner in which these velocities are most efficiently considered. This is discussed in detail in the section on Calculation Procedures to follow.

Separated wake.- The separated wake on the lee side of the body is represented by a large number of discrete vortices, each vortex originating from separation locations at each axial marching step in the calculation. The major portion of the lee side vortex wake has its origin at the primary separation points on each side of the body. The remainder of the wake originates from the secondary separation points located in the reverse flow region on the lee side of the body. Both of these points are illustrated in the sketch of a typical crossflow plane of an elliptic cross section body shown in Figure 3. The mechanics of the calculation of the individual vortices for both smooth forebodies and forebodies with chines are described to illustrate the differences in the prediction methods.

For smooth bodies, References 1 and 2, the separation causing the vortex shedding into the lee-side wake is of a type traditionally associated with boundary layer separation. Prediction of the separation locations on smooth bodies has been presented in the above references, but a brief description is included here for completeness.

The predicted pressure distribution for the primary flow in the crossflow plane is referenced to the conditions at the minimum pressure point, and a virtual origin for the beginning of the boundary layer is calculated. The adverse pressure distribution downstream of the minimum pressure point is considered with either Stratford's laminar (Ref. 26) or turbulent (Ref. 27) separation criterion to determine whether or not separation has occurred. These criteria, based on two-dimensional, incompressible, flat plate data, are adjusted empirically for three-dimensional crossflow effects in Reference 2. The laminar separation criterion states that the laminar boundary layer separates when

$$\sqrt{C_p} \left[\xi \frac{dC_p}{d\xi} \right] \simeq 0.087 \sin\alpha_c \tag{58}$$

In a turbulent boundary layer, separation occurs when

$$C_p \left[\xi \frac{dC_p}{d\xi} \right]^{1/2} (Re_\xi \times 10^{-6})^{-0.1} \simeq 0.350 \sin\alpha_c \tag{59}$$

The $\sin\alpha_c$ in Equations (58) and (59) is the three-dimensional modification.

If the criteria indicate a separation point, the vorticity flux across the boundary layer at separation is shed into a single point vortex whose strength is

$$\frac{\Gamma}{V_\infty} = \frac{u_e^2}{2V_\infty^2} \frac{\Delta x}{\cos\alpha_c} \delta \tag{60}$$

assuming no slip at the wall. δ is the vortex reduction factor described previously, and it is generally set equal to 0.6 for ogive-cylinder configurations and 1.0 for bodies with closed boattails (Ref. 1). For bodies with chines or other sharp edges initiating separation, $\delta = 1$.

For smooth bodies, the initial position of the shed vortex is determined such that the surface velocity in the crossflow plane at the separation point is exactly canceled by the shed vortex and its image. When this criterion results in a vortex initial position that is too near to the body surface, certain numerical problems can cause difficulty in calculating the trajectory of this vortex. If the initial position of the vortex is nearer than five percent of the body radius from the surface, the vortex is generally placed five percent of the equivalent body radius from the surface.

For bodies with chines or other sharp edges, the primary separation location is fixed at the sharp edge, thus negating the need to predict separation as described above for smooth bodies. The appropriate boundary condition is to assume the flow leaves the sharp edge smoothly; that is, the Kutta condition is satisfied at the edge. This boundary condition transforms to a stagnation point in the circle plane at the separation point.

The common difficulty for all vortex cloud methods applied to sharp edges (e.g., Refs. 5, 6 and 9), including the present method, lies in the solution for the shed vortex at each time step. Only one equation is available from the Kutta condition to solve for two unknowns, the vortex strength and its position. In the smooth body analysis, an external boundary condition provides the missing equation. This condition is the determination of the strength of the vortex from the vorticity in the boundary layer prior to separation as given by Equation (60). In some methods noted above, the analysis was developed with the assumption of conical flow to provide the necessary information. Several different approaches were examined in the present work, and these are discussed below.

The initial approach is based on the method developed by Sacks (Ref. 9). At the first shedding station on the forebody and chine, there is no vorticity in the field; therefore, the chine edge is a singularity and it is not possible to calculate a realistic v-velocity near the edge. In Reference 9, the solution is started by assuming the velocity outboard at the chine

edge is approximately represented by $v = 0.5\sin\alpha$, and the shed vortex is convected outboard a distance $v\Delta t$. In this work, the pressure distribution is calculated at the initial station with no vorticity in the field; therefore, there is a singularity at the chine edge. The average v-velocity over the outer 10-percent of the chine, excluding the singularity, is used to locate the initial shed vortex. Placing the vortex at this position satisfies the requirement for one of the two equations, and the remaining equation can be used to calculate the strength of the vortex such that the Kutta condition at the chine edge is satisfied. With a vortex in the field which satisfies the Kutta condition, it can be convected with the local flow field during the next time step. Now, though the Kutta condition is not satisfied after the vortex moves, the v-velocity can be calculated at several points on the forebody near the chine edge. The velocities on the outer ten percent of the chine semispan are averaged to find a convecting velocity for the next shed vortex. As before, when the position is known it is possible to determine the strength by satisfying the Kutta condition at the chine edge.

The method of convecting the shed vortex to its initial position has been the subject of much discussion between investigators, and there are nearly as many methods as there are investigators. When a sheet of vorticity is shed from the trailing edge of an airfoil in unsteady motion, a case is made in Reference 28 that the sheet should leave the edge tangent to the surface. In Reference 29, a procedure for locating the shed vortex next to the edge of a cambered plate is described. In this case, the vortex is located at a point in the field which produces the proper flow field in the vicinity of the edge. Unfortunately, this approach requires a significant iterative computational effort for each different geometry; therefore, it is not practical for an engineering method which must be available to use for changing geometries without large set-up times. In the current version of VTXCHN, the former method is used in which the shed vortex is convected to its initial position along a line tangent to the windward surface of the chine.

An alternate approach in which the chine is approximated as a lifting surface is also available to start the solution. In this method, the chine is represented as a single panel lifting surface on the transformed circular body as shown in Figure 5. The single panel is oriented along the mean line of the chine to approximate the local incidence to the free-stream velocity. The no-flow boundary condition is satisfied at a single point on the panel,

and the strength of the vortex at the panel edge is the result. With the strength known, there is a single point along the projection of the panel used to model the chine at which the vortex can be located to satisfy the Kutta condition at the chine edge. This provides the necessary starting solution so that the remainder of the calculation can be carried out as described above.

The mechanics of the panel approximation are very simple. After some investigation, the best location to satisfy the boundary condition is at half the chine semispan. It is also best to use this approximation only for the starting solution, even though it can be applied at any number of axial stations. This latter limitation is imposed because the strength of the vortex determined from the panel solution is significantly weaker than the vortex shed by the previously described method. For example, in Figure 6, the build-up of shed vortex strength from the two methods is compared for a typical chine forebody configuration at $\alpha = 20°$. Notice that the strength differential caused by the initial shed vortex specified by the panel approximation is never recovered, but the difference over the length of the forebody is minimal and has almost no effect on the forebody loads.

The chine shedding solution was further studied by specifying the strength of the shed vortex in a manner similar to that used for smooth bodies. The velocity distribution tangent to the lower surface of the chine near the outer ten-percent of the semispan was calculated and averaged to approximate the velocity near the chine edge. Assuming that separation occurs at the chine edge, but also assuming that the vorticity in the boundary layer at the chine edge determines the strength of the shed vortex as on a smooth body, a vortex can be placed in the outer flow to satisfy the Kutta condition at the edge as described above. A preliminary calculation with this method resulted in a total vortex strength very similar to the other methods described, but the vortex shedding rate seemed to be erratic. This may be caused by the difficulty in calculating a smooth velocity distribution necessary to determine vortex strength in a region where the local velocities can change quickly as the discrete vortices move in and out of influence of the chine edge. There was also difficulty satisfying the Kutta condition at the chine edge; therefore, this method was abandoned.

The calculation of secondary separation on the lee side of a forebody with a chine is carried out in the same manner as described above for primary separation on smooth bodies. It is necessary that a reverse flow region exist on the lee side of the body and that a second minimum pressure point be found in this region. For purposes of this analysis, the reverse flow is assumed to be laminar from the lee side stagnation point to the secondary separation point, and Stratford's laminar criterion is used to locate secondary separation. Laminar separation in the reverse flow region is expected because of the low velocities on this portion of the body. The vortex released into the flow at the secondary separation point has the opposite sign of the primary vortex and is generally weaker in strength.

In theory, secondary separation is a straightforward concept; however, in practice, it is very difficult to implement. This has been noted by other investigators (Ref. 29) for various body shapes. The computational difficulties are caused by both the separation and the tracking portions of the method. The separation problems are caused by the variations in the pressure distributions on the lee side of the chine caused by the influence of the primary chine vortex. It is not unusual that a second minimum pressure is not observed at some axial stations; as a consequence, a secondary separation point is not predicted and a "hole" is left in the secondary vortex sheet. This problem can be overcome by forcing secondary separation, a common procedure in vortex cloud methods. The tracking problems are caused by the large primary vortex capturing the smaller secondary vortices and pulling them away from the chine surface. When this happens, the induced effects of the secondary separation disappear, and there is no advantage to including these additional vortices in the solution. In addition, though not a primary consideration in this discussion, the secondary vortices have a significant influence on the computation time since each vortex adds two more differential equations to the set to be solved.

Forces and moments.- The forces and moments on the body are computed by integration of the pressure distribution around the body. At a specified station on the body, the normal-force coefficient on a Δx length of the body is

$$c_n = \frac{\left[\frac{dN}{dx}\right]}{q_\infty D} = \frac{1}{D}\int_0^{2\pi} C_p r' \cos\beta' \, d\beta \qquad (61)$$

where r′ is the distance from the axis of the body to the body surface and β' is the local slope of the body in the crossflow plane. This is illustrated in the sketch in Figure 4. For circular bodies, $r' = r_o$ and $\beta' = \beta$. The total normal force coefficient on the body is

$$C_N = \frac{N}{q_\infty S} = \frac{D}{S} \int_0^L c_n \, dx \tag{62}$$

and the pitching-moment coefficient is

$$C_m = \frac{M_y}{q_\infty S l_{ref}} = \frac{D}{S} \int_0^L c_n \left[\frac{x_m - x}{l_{ref}} \right] dx \tag{63}$$

The center of pressure of the normal force is

$$\frac{x_{cp_n}}{l_{ref}} = \frac{x_m}{l_{ref}} - \frac{C_m}{C_N} \tag{64}$$

Similarly, the side-force coefficient on a Δx length of the body is

$$c_y = \frac{\left[\frac{dY}{dx} \right]}{q_\infty D} = -\frac{1}{D} \int_0^{2\pi} C_p r' \sin\beta' \, d\beta \tag{65}$$

The total side-force coefficient on the body is

$$C_Y = \frac{F_y}{q_\infty S} = \frac{D}{S} \int_0^L c_y \, dx \tag{66}$$

and the yawing-moment coefficient is

$$C_n = \frac{M_z}{q_\infty S l_{ref}} = -\frac{D}{S}\int_0^L c_y \left[\frac{x_m - x}{l_{ref}}\right] dx \qquad (67)$$

The center of pressure of the side force is

$$\frac{x_{cp_y}}{l_{ref}} = \frac{x_m}{l_{ref}} + \frac{C_n}{C_Y} \qquad (68)$$

A noncircular body at an arbitrary roll angle may experience a rolling moment caused by the nonsymmetry of the loading around the body. The total rolling moment on the body is calculated by summing the moments of the individual components of normal force and side force around each cross section and integrating over the body length. The rolling moment coefficient is calculated as

$$C_l = \frac{M_x}{q_\infty S l_{ref}} = \frac{1}{S l_{ref}}\int_0^L \int_0^{2\pi} (yC_p r' \cos\beta' - zC_p r' \sin\beta') \, d\beta \, dx \qquad (69)$$

Though the primary purpose of the vortex shedding method is not to predict drag or axial force on the missile, a procedure to estimate both pressure drag (excluding base drag) and skin friction is included. The pressure contribution to the axial-force coefficient is

$$C_{A_p} = \frac{1}{S}\int_0^L \int_0^{2\pi} (C_p \frac{dr'}{dx}) \, d\beta \, dx \qquad (70)$$

The local skin-friction coefficient, based on the assumption of a 1/7th power law velocity profile in the boundary layer, is

$$c_f = .0592 \left(\frac{V_\infty x}{\nu} \right)^{-.2} \tag{71}$$

which produces a drag coefficient due to friction

$$C_{D_f} = \frac{2\pi}{S} \int_0^L r_{eq} c_f \, dx \tag{72}$$

At high angles of incidence, streamlines around the body are inclined at approximately

$$\alpha_s = \tan^{-1}(2\tan\alpha_c) \tag{73}$$

therefore, the axial component of the friction drag is

$$C_{A_f} = C_{D_f} \cos\alpha_s \tag{74}$$

The total axial-force coefficient is the sum of Equations (70) and (74).

Vortex core. - The diffusion core model (Ref. 2) for the point vortex- induced velocities removes the singularity at the vortex origin and effectively reduces the velocities near the vortex. The tangential velocity induced by a single point vortex is written as

$$\frac{v_\theta}{\Gamma} = \frac{1}{2\pi r} \left[1 - \exp\left(\frac{r^2 V_\infty}{4x\nu} \right) \right] \tag{75}$$

where r is the distance from the vortex to the field point and x is a measure of the age of the vortex. The induced velocity from this core model is illustrated in the following sketch.

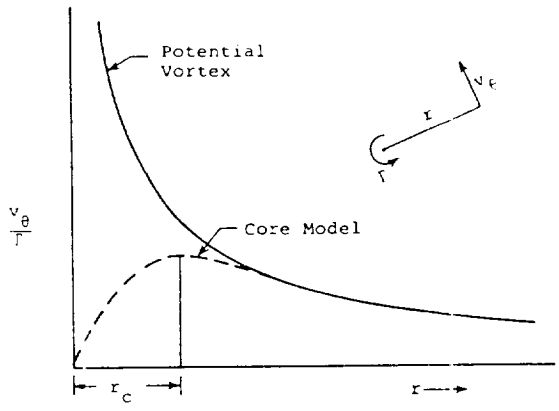

Sketch - Vortex-Induced Velocity

The vortex core model represented by Equation (75) has received considerable attention in the context of body vortex-induced effects, and it has a number of shortcomings. Since the exponential term is a function of r, the flow medium (ν) and the age of the vortex (x), the core is constantly changing size as the vortex moves through the field. Under certain conditions, the core radius, denoted as r_c in the sketch, can become very small and the induced velocity becomes unrealistically large. In an attempt to further modify the core model to keep the induced velocities within physically realistic limits, the following modification was made in Reference 3. The location of the maximum induced velocity, r_c in the sketch, is fixed at a specific radius to be selected by the user. Given a core radius, the vortex-induced velocity is

$$\frac{v_\theta}{\Gamma} = \frac{1}{2\pi r}\left[1 - \exp\left(-1.256\,\frac{r^2}{r_c^2}\right)\right] \qquad (76)$$

The core model described by Equation (76) is included in the version of the code described in this report, and in a later section, guidelines for the selection of an appropriate core radius are presented. Results indicate that this simple core model provides adequate smoothing for the necessary velocity calculations.

Other investigations of discrete vortex models must use a core model of some type. Although there are many different core models, all serve the same purpose as those

described above, and nearly all are directed at eliminating the singularity and reducing the maximum induced velocity. The code VTXCHN described in this report is easily modified to incorporate another core model if the user desires.

Calculation Procedures

As a part of the chine investigation described herein and based upon the experience of the authors in working with vortex cloud methods, several interesting changes in the calculation procedures have been studied. These changes were identified during a study of computational efficiency and accuracy in the anticipation that both could be increased. The following paragraphs discuss the results of this study.

Unsteady pressure term.- Practical aspects of calculating the pressure distribution on chined forebodies for preliminary design and analysis dictates the requirement for a fast computational method. As has been described by a number of investigators, discrete vortex methods can be time consuming and computationally inefficient, particularly when the number of vortices is large. For example, prediction of the pressure distribution from Equation (56) can require a significant amount of computer time on bodies with a large number of vortices simply because each vortex contributes to this term at each point on the body. When a noncircular body is being considered, the computation time is increased further because each vortex must be mapped numerically to the circle plane. Computation time notwithstanding, it has also been noted by the authors that this unsteady pressure term can cause a number of other problems. For example, when an individual discrete vortex is very near the surface of the body, it can have a very large local effect on the pressure distribution both through the induced velocity effect and the unsteady effect. The unsteady pressure term can be large even when an individual vortex in the cloud has occasion to move rapidly in the field because of interaction with another vortex. In both these cases, the local pressure coefficient may have a saw-tooth distribution and can exhibit extreme jumps or spikes. The goal of this study was to find a means to smooth the predicted pressure distribution and achieve faster computational times with no significant change in accuracy.

Since the major contributor to the computation time of the unsteady pressure term, Equation (56), is the summation over all the vortices in the field for each point on the body, this is where the study began to increase computational efficiency. Two approaches were examined. In the first, all shed vorticity was concentrated into a single vortex at the centroid of the cloud for purposes of evaluating the vortex contribution of Equation (56). In the second approach, the feeding sheet was represented by a number of discrete vortices and the remainder of the cloud was concentrated into a single vortex located at the centroid of the cloud. This latter approach is illustrated in Figure 7.

Before any evaluation of computational savings of the modifications, it is important to understand the effect on the accuracy of predicted results. To this end, comparisons of measured and predicted pressure distributions on an axisymmetric ogive-cylinder body (Ref. 30) were used to evaluate the calculation procedures. An axisymmetric body without chines was selected to avoid any special problems created by the noncircular shape and the associated mapping and to take advantage of well-tested experimental data in which confidence exists.

A series of comparisons at $\alpha = 20°$ is shown in Figure 8 where the circumferential pressure distribution at a number of axial stations along the body are considered. For purposes of this evaluation, three different cases are shown. The first, denoted by NVPHI=-1, corresponds to the traditional calculation procedure in which all vortices in the cloud are included in the summation in Equation (56). The second, denoted by NVPHI=0, represents the condition in which all shed vortices at each axial station are collected into a single vortex at the centroid of the vortex field. Finally, the last case, denoted by NVPHI=5, represents a combination of the previous two cases in which the feeding sheet consists of five vortices and the remainder of the cloud is collapsed into a single vortex. Remember that the individual vortices in the cloud are collapsed into their centroid only for the evaluation of Equation (56), and for all other computations, the entire cloud of discrete vortices is used.

In Figure 8(a), there is no difference in the predicted pressure distribution near the nose. In Figure 8(b), there is a difference in the pressure distribution between the traditional results (NVPHI=-1) and those results obtained when all the discrete vortices are collapsed

into a single vortex at the centroid (NVPHI=0). There is no effect of keeping the feeding sheet and cloud separate because the total number of vortices in each field is less than seven; therefore, this method and the traditional method are identical at this point.

As the number of vortices shed from the body increases, the difference between the traditional results and the alternative methods becomes larger, and as seen in Figures 8(c, d, and e), collapsing all the vortices into a single vortex produces significantly inferior pressure results. Keeping the feeding sheet intact and collapsing the cloud vortices is in better agreement with the original method, but it appears that, as the number of vortices becomes large, the agreement between the methods begins to deteriorate. It is apparent from these comparisons that the success of the vortex cloud method in predicting accurate pressure distributions is due to the distribution of the discrete vortices throughout the flow field.

As a consequence of these comparisons, the decision was made to keep the traditional approach of separate and distinct discrete vortices for the entire pressure calculation. The feeding sheet is obviously an important feature of the flow model, and the minimal savings in computational efficiency observed is not worth the loss of accuracy in the predictions. The options to use these modifications have been retained in the code in the event the user wishes to test the modified method for other configurations.

Vortex tracking.- Calculation of the motion of the discrete vortices after they are shed from the body is a key component of the prediction method. The location of the vortices and the cloud formed influences the strength and subsequent positions of later vortices shed from the body, and ultimately, the tracked positions of the vortices determines the induced loading on the body. As noted by other investigators (Ref. 27), it is common for tracking problems to arise during the normal calculation of the motion of the individual vortices. The usual nature of these problems is a vortex inside the body, and the usual solution is to simply eliminate the offending vortex from the flow field. In the code presented herein and in Reference 1, the solution is to replace the vortex back into the flow field outside the body and allow it to continue as part of the cloud. This procedure has been reasonably successful on axisymmetric bodies, though the problem occurs so infrequently in most configurations examined by the authors that it is difficult to test the validity of this approximate solution.

This procedure did not prove very successful in the case of the chine configurations; therefore, some work was directed at understanding the mechanics of the tracking problem in the anticipation that it could be eliminated.

The equations of motion of the vortices are shown in Equation (30). The motion of a vortex is determined by integrating these equations, along with those for the other vortices, from one axial station to the next, a distance dx. For most purposes, dx is a constant over the entire length of the body; although, as discussed in Reference 3, dx can be a variable length. When the tracking procedure was originally developed, the u-velocity in the denominator was included to correct for the effect of a growing body near the nose; that is, for axisymmetric bodies, the u-velocity was determined by the source singularities representing the body (Eq. (10)). This velocity was essential for the successful tracking of vortices shed near the nose, and, upon a brief analysis, it becomes obvious why this is the case. Equation (30) represents to first order the slope of the vortex filament between the two axial stations. If a vortex is very near the body surface, the slope must be the same as the body slope or greater, or the vortex will be tracked inside the body; therefore, near the body nose the u-velocity from the sources (which is opposite in sign from $V_\infty \cos\alpha_c$) is necessary to decrease the magnitude of the denominator and increase the slope of the filament, thus keeping the vortex from penetrating the body surface during tracking.

For noncircular bodies, the effect of the body shape on the v- and w-velocities in Equations (30a) and (30b) is included by means of the conformal transformations described previously. In the original work (Refs. 1 and 2), the u-velocity was included as an axisymmetric effect from the equivalent body, and there was no noncircular effect on the u-velocity. In this extension of the work of Reference 1, the approximate contribution of the noncircular shape to the u-velocity is determined from Equation (45). When the full u-velocity, described in the section containing Equation (45), was included in the tracking, the vortices tracked inside the body on a regular basis. The difficulty appears to be a subtle violation of one of the basic assumptions inherent in the vortex cloud procedure.

The unsteady analogy used in the vortex cloud method of modeling the lee-side vorticity assumes that all the vortices are moving at the same u-velocity such that they

traverse the dx-distance between axial stations in the same time. When the u-velocity consists of a free-stream component and a volume or source component, this assumption is nearly correct for all vortices near the body, even when the body is noncircular and there is a small variation in u-velocity around the body. However, when the doublet effects are included, the u-velocity can vary significantly around the body and with distance from the body. In this case, the vortices are not all traversing axially at nearly the same velocity, and the unsteady analogy approximation is not strictly correct. The numerical problems can be explained using Equation (30). On the lee side of the body, the doublet singularities represent the acceleration of the u-velocity on that side of the body, the denominator becomes very large near the body, and the slope of the vortex filament decreases until it can be less than the slope of the body. As a consequence, the vortex tracking calculation forces the vortices inside the body.

For purposes of the prediction method in the code VTXCHN, the u-velocity used for tracking purposes does not include the doublet terms. These terms are included in the surface pressure calculation and the velocity field calculations.

RESULTS

For purposes of evaluating the accuracy and range of applicability of the subsonic vortex shedding model for forebodies with chines and the associated computer code VTXCHN, comparisons of measured and predicted aerodynamic characteristics are presented. Since the major objective is the validation of the prediction method, not all predicted results are in good agreement with experiment to illustrate to the user where problems may occur during general use of the code. Typical results from the prediction method follow.

Circular Bodies

Though not specifically part of the stated objective of the reported work, the prediction method is applicable to axisymmetric bodies and noncircular bodies without chines. The

code, VTXCHN, can be used to predict vortex shedding from forebodies alone in exactly the same manner as the predecessor code, VTXCLD, in Reference 1. For circular bodies, VTXCHN should produce results similar to VTXCLD, but because of minor improvements in the separation calculation, the results may not be identical. For practical engineering purposes, the results from the two codes are so nearly the same, additional comparisons with experiment for circular bodies will not be included in this report.

Measured and predicted pressure distributions on an ogive-cylinder model (Ref. 30) in subsonic flow at an angle of attack of 20 degrees has already been presented in Figure 8. The configuration has a 3-caliber ogive nose and a 7.7-caliber cylindrical afterbody, and as described in Reference 1, the model is represented by 61 point sources and sinks on the axis, and the ogive nose is used to close the model at the base. Laminar separation is used for all predictions for this model; however, there is some indication of both laminar and turbulent separation in the data.

At $\alpha = 20°$, a reasonable vortex field is developed on the lee side and has a significant effect on surface pressure distributions on most of the body. Some of the roughness in the predicted results is caused by individual vortices moving too near the body surface during the trajectory calculation. The vortex core model does tend to smooth the vortex-induced effects, but there can still be a large local effect. These local irregularities have a minimal effect on the integrated loads.

Noncircular Bodies

The noncircular body options (without chines) in VTXCHN have been tested for a number of different cross section shapes, both elliptic and arbitrary, to verify the transformation procedures. Since these are nearly identical to those reported in Reference 1, they are not repeated. It should be noted that the changes in the u-velocity caused by the noncircular body effects now included will cause the results from VTXCHN to be slightly different from those obtained from VTXCLD. Examples of the predicted differences in the pressure distributions on a 2:1 cross section elliptic body (Ref. 31) are shown in Figure 9. In Figure 9(a), the circumferential pressure distribution near the nose is shown at $\alpha = 0°$ to

eliminate the influence of all but the noncircular source contribution to the pressure. The dashed curve is the result from VTXCLD (Ref. 1), the solid curve is the result from a panel method (Ref. 16), and the dotted curve is the result from VTXCHN including the noncircular u-velocity modification described previously. The VTXCHN result is in very good agreement with the panel result, and it shows a significant improvement over the previous result without the u-velocity correction.

The predicted pressures on the same configuration at $\alpha = 10°$ are compared in Figure 9(b). In this case, no separation is included in any of the results to permit comparison of potential flow effects only. Now the angle of attack effects dominate the pressures, and the body volume effects are small; however, the VTXCHN results are still in good agreement with the panel results and show an improvement over the original VTXCLD results.

A thorough examination of noncircular bodies without chines was beyond the scope of the present work; therefore, the results presented in Reference 1 were not repeated for this report. The user should be aware that VTXCHN will produce slightly different results than VTXCLD because of the modifications in the noncircular u-velocity terms.

Forebodies With Chines

Comparison of measured and predicted aerodynamic characteristics on typical forebodies with chines is the most reliable means to evaluate the strengths and weaknesses of the engineering method embodied in the code VTXCHN. Since pressure distributions provide the best assessment of the capabilities of a prediction method, the configuration and experimental data of Reference 32 provide a wide range of information for verification of the method. The forebody model with the three specific axial stations at which pressures are measured is shown in Figure 10. The experimental data shown in the following figures were measured with a 60-degree delta wing in place aft of the forebody, but it appears that the wing had only minimal influence at the last pressure station on the body. The effect of the wing is not modeled in the prediction method.

Measured and predicted pressure coefficients on the upper surface of the forebody are shown in Figure 11 for the configuration at $\alpha = 10°$. Predicted pressures on the lower surface are shown in these figures, and the predicted vortex cloud pattern at each station is also shown to provide some perspective of the region of influence of the lee side vortex. In Figure 11(a), the measured and predicted pressure coefficients at the first forebody station, $x \approx 7$ inches from the nose, are compared. The predicted pressures have the correct characteristics on the suction side of the body, but the suction peak caused by the vortex seems to be spread over a larger region than that measured. The pressure on the lower surface is nearly constant. The predicted pressure distribution without vortex effects is shown as a dashed curve. At this low angle of attack, the vortex-induced effects are confined to the upper surface of the chine.

In Figure 11(b), the second axial station, $x \approx 13.5$ inches from the nose, exhibits lower suction pressures on the upper surface, and the predicted results are in very good agreement with experiment except for the suction peak near the chine edge.

The last axial station at $x = 20$ inches in Figure 11(c) shows good agreement between the measured and predicted pressure distributions on the upper surface. The vortex-induced effects are less at this station than at the previous station even though the vortex strength has increased. This is caused by the increased distance between the rolled-up vortex and the chine upper surface. The change in vortex shape between the two axial stations is determined by the angle at which the vortices leave the chine edge, and it is apparent that the vortices from the aft station are leaving the edge at a smaller angle. This causes the rolled-up vortex to be displaced outboard and upward from the chine edge, thus decreasing the vortex-induced pressure.

Measured and predicted results on the same configuration at $\alpha = 20°$ are presented in Figure 12 for the same three axial stations. As before, the predicted pressure distribution on the forebody without separation is shown as the dashed curve to illustrate the induced effects of the vortices. As expected from the vortex fields, the influence of the chine vortex is concentrated on the chine and the region of the chine-body junction.

In general, the results at $\alpha = 20°$ with separation effects included are the same as shown in the previous figures for the first two axial stations. The agreement between measured and predicted pressures is very good. At the aft axial station, the predicted suction pressure on the lee side is significantly lower than that measured. The explanation is not obvious at this time, but the problem could be with the predicted strength and/or position of the shed vortex, or it could be due to some external influence such as the wing. There is not sufficient experimental data available to determine the reasons for the observed problems.

When the angle of attack is increased to 30 and 40 degrees in Figures 13 and 14, respectively, the results become very consistent at all stations on the forebody. The predicted pressure distribution is in good agreement with the measurements on the fuselage upper surface away from the chine, but the agreement is generally poor everywhere on the chine. The predicted suction pressure is always less than that measured; therefore, the integrated normal force will be less than that measured at the higher angles of attack. The problem on the chine could be caused by the vortex position. It is apparent from the vortex fields shown on each figure that as the angle of attack increases, the vortex moves farther from the body thus reducing its effect. Comparison of the predicted pressures with and without the vortex field shows that the method represents the qualitative effects of the vorticity even though the actual pressure levels are not in good agreement with experiment.

It is possible that secondary separation on the lee side of the forebody can be changing the vorticity distribution in the flow field sufficiently to have a measurable effect on the pressure distribution. Secondary separation effects were not included in these calculations.

When the forebody at angle of attack is yawed to some nonzero sideslip flow angle, the separation becomes asymmetric. The assumption is made that separation still occurs at the chine on both sides of the forebody, but the asymmetric flow field changes the tracking and subsequent vortex distributions. This assumption is good for moderate yaw angles, but when the yaw angle approaches the angle of attack, the flow is approaching the windward chine at a low incidence angle, and separation occurs on the body surface rather than at the chine edge.

In Figures 15 and 16, the predicted pressure distributions on the forebody at $\beta = 10°$ and $\alpha = 20°$ and $30°$, respectively, are compared with experiment. The agreement at the first axial station is reasonable on the chines at both angles of attack, and it is clear that the vortices are not having enough influence on the local pressures on the lee side of the chine. Some of the difficulties with these results can be explained by studying the vortex field, also shown in the figures. At the first station, the vortex on the right side of the body seems to be spread out over a large region of the lee side of the body, and the influence of the vortex on the surface pressure reflects this phenomenon. The predicted vortex induces a low pressure over more of the upper surface than is measured, but the pressure peak near the chine edge for $\alpha = 30°$ is lower than indicated by the experiment. As for the $\beta = 0°$ described above, the pressure level at the lower angle of attack is in better agreement with the measured pressures. On the left side of the body the vortex is rolled up in a loose fashion and is concentrated away from the body surface. As a consequence, the predicted suction pressure peak is significantly lower than that measured. Another interesting result at this first station is the presence of a single vortex from the right chine on the left side of the body.

At the second axial station shown in Figures 15(b) and 16(b), the vortex on the right side is much stronger than at the previous station, it is tightly rolled up, and, as a consequence, the suction peak is in better agreement with experiment. The vortex on the left side is also tightly rolled up, but it is concentrated away from the body and its influence on the pressure distribution is less than that measured at the higher angle. As at the previous station, the pressure peak on the left side is less than the measured value at both angles of attack.

Finally, at the third axial station shown in Figures 15(c) and 16(c), the vortex is tightly rolled up near the body, and the predicted pressure peak on the chine is in good agreement with experiment. Though the left chine vortex is rolled up a large distance from the chine surface, the pressure levels are in reasonable agreement with the measurements except for a region on the body near the junction with the chine.

The discrete vortex fields shown in the above pressure figures help illustrate the extent of the vorticity shed from the chine, but these results do not provide much information on the nature of the physics of the flow in the vicinity of the forebody. To better understand the full effect of the shed vorticity, flow field calculations provide a direct visualization of the velocity field. A representative set of velocity vectors in the flow field adjacent to the forebody at $\alpha = 20^\circ$ is shown in Figure 17. The accuracy of the flow vectors inside the vortex or very near individual vortices will be in question because of the influence of the discrete vortices, but the overall character of the flow field is correct. These vector plots are most useful in visualizing the region of influence of the vortex, particularly if there is concern about vortex-induced loads on other components of the airframe.

If there is interest in estimating these vortex-induced loads, the strength of the shed vorticity is needed. This detailed information is also available from the prediction method. The strength of the vortex shed from the forebody at various angles of attack is shown in Figure 18 to illustrate this capability.

PROGRAM VTXCHN

General Description

This section provides a general description of program VTXCHN and its various subroutines. The code is written in modular form so that, as improvements in flow models become available or as other modifications are required, they are easy to incorporate. The flow of the calculation is described in this report, and detailed comments are provided throughout the code to assist the user in understanding the order of calculation.

The computer code consists of the program VTXCHN and 45 subroutines. The overall flow map of the program is shown in Figure 19 where the general relationship between the subroutines and external references can be seen. Communication between the program modules is handled primarily by named common blocks. A cross reference table for the

calling relationship between the program subroutines is shown in Figure 20. A similar table for the named common blocks is shown in Figure 21.

The program is written in standard FORTRAN. Execution on a VAX 11/750 can vary from 10 seconds to more than 45 minutes depending on various factors such as the geometry, the integration interval (DX), the number of shed vortices, the use of flow symmetry, and the flow conditions.

Subroutine Description

This section briefly describes the main program VTXCHN and its various subroutines.

VTXCHN This is the main program for calculating the forces and moments on a slender body in a steady flow condition including the nonlinear effects of lee side separation vorticity.

AMAP Transforms a specified point in the circle plane to its corresponding point in the body plane.

ASUM Calculates the velocity term due to transformation for noncircular bodies.

BMAP Sets up a table of points on the actual body corresponding to specified points on the circle.

BODY Organizes the flow through VTXCHN. It organizes calls to predict vortex shedding, to calculate surface velocities and pressures, and to calculate the overall forces and moments on the body.

CHNGAM Calculates the strengths and locations of vortices shed from a chine cross section body.

CHNINI Calculates the initial strengths and locations of vortices shed from a chine cross section body. This is done by approximating the body with chine as a circular body with a strake modeled by a vortex lattice.

CMAP Transforms a specified point in the body plane to its corresponding point in the circle plane.

COMBIN Combines vortices which are separated by a distance less than or equal to "RGAM". (The resulting vortex strength is the sum of the individual strengths, and its location is the centroid of the combined vortices).

CONFOR Calculates the coefficients of the numerical conformal mapping function. Transforms the region outside of a polygonal shape with a vertical plane of symmetry to the region outside of a circle.

CPPOT Calculates a potential pressure distribution at a given x station (the effects of separation vortices are not present in the C_p calculation). This is used in determining a turbulent separation point for the transition region.

DFEQKM Obtains vortex paths between stations x and $x + \Delta x$ using a Kutta-Merson integration scheme.

DNUDX Calculates the noncircular mapping derivative $\partial \nu / \partial x$.

DPHIDT Calculates the two-dimensional unsteady pressure term for use in the unsteady Bernoulli equation.

DZDNU Calculates the differential of the transform of a polygonal shape to a circle.

F Calculates the derivatives of the vortex equations of motion which are used in conjunction with DFEQKM to obtain the vortex paths.

FDPSDR Calculates the axial velocity due to a three-dimensional source distribution.

FORCEP Calculates the forces and moments on the body by an integration of the surface pressure distribution.

FPSI Calculates the axisymmetric body shape represented by a three-dimensional source distribution.

FPVEL Calculates the velocity at specified field points.

INPT Reads in and prints out the body geometry, the flow conditions, various program options, and restart quantities.

INVERS Solves simultaneous linear equations, $[A]\bar{x} = \bar{b}$.

PLOT Creates a line printer plot of the body and its vortex wake at any given x station. It is composed of the following subroutines: PLOTV, PLOTA2, PLOTA5, PLOTA6, PLOTA7, and PLOTA8.

RDRDX Calculates r and dr/dx at a given x station.

RDRDXI Initializes the calculation of r and dr/dx for subroutine RDRDX.

SEPRAT Predicts the position in the crossflow plane where separation occurs based on the Stratford criteria for laminar and turbulent flows.

SHAPE Determines the body geometric parameters from a table look-up of input data.

SKIN Estimates the axial skin friction force on the body.

SORDIS Calculates the source distribution representing an axisymmetric body of revolution given the body shape and slope at each x station.

SORVEL Calculates perturbation velocities due to a three-dimensional source distribution. Used by subroutine SORDIS in calculation of the source distribution.

SRCVEL Calculates perturbation velocities due to a three-dimensional source distribution.

SUM Analytical mapping of an elliptical cross section.

TRANSN Calculates the body separation points in the transition region.

UMAP Calculates the axial velocity, $\partial\Phi/\partial x$, due to noncircular mapping and two-dimensional singularities.

VCENTR Calculates the centroid of each vortex field.

VCNTR Calculates the centroid of any set of vortices. This routine is used for the $d\phi/dt$ calculation.

VCNTRP Calculates the actual centroid of vorticity for subroutines VCNTR and VCENTR.

VINFLU Calculates the influence of a unit strength vortex and its image.

VLOCTY Calculates the velocity components in the cross flow plane at a specified field point.

VTABLE Sets up the arrays of free vorticity for two cases: (1) The vorticity in the working array GAM is distributed into the individual arrays GAMP, GAMM, GAMR, GAMA, or (2) the vorticity in the individual arrays GAMP, GAMM, GAMR, GAMA is distributed into the working array, GAM, in the proper order.

Z Calculates the transformation of a polygonal shape to a circle of radius RZ.

Program Limitations and Suggestions

Program VTXCHN predicts the aerodynamic forces acting on slender bodies alone at high angles of attack, with some limitations. Certain of the limitations that follow are basically rules-of-thumb for the use of the program which have been determined through program verification and experience with the code.

Chine cross section bodies.- There are several things that are required when modeling bodies with chine cross sections. First, because of limitations in the numerical conformal mapping procedure, the input geometry specification of the chine cross section may have to be simplified. If the numerical mapping fails to converge or if the message "ERROR IN THE SUM OF EXTERIOR ANGLES" occurs, the number of points specifying the cross section may need to be reduced while maintaining the general shape of the cross section.

The source distribution input for a chine body must correspond to an equivalent area distribution body. The equivalent area distribution radius, r_{eq}, must be calculated external to the program. The mapped radius, r_o, is also required by the program. The only method to obtain the mapped radius is to run the program. It is only necessary to run the code for the first axial station (i.e. set XI = XF) since all of the mapping information is calculated at the beginning. The input requires that the mapped radius be input with the same resolution as the equivalent radius; therefore, this may require an effort or utility program external to VTXCHN to obtain r_o at the axial station specified for r_{eq}.

With a chine cross section it is possible for tracking problems to occur, and a STOP 40 will occur. The chine cross sections are more prone to this problem than circular or elliptic cross sections. If this problem is encountered, the following variables can be altered to alleviate the tracking problems:

E5	tolerance for vortex tracking
RCORE	vortex core size normalized by body diameter
DX	axial spacing between tracking stations

Mach number.- The major limitation in the program is the Mach number or compressibility correction. The compressibility correction added to VTXCHN is based on small perturbation theory which restricts the body to be slender, the angle of attack to be small, and the Mach number to be approximately 0.8 or less. Program VTXCHN including the compressibility correction models subsonic flow with linear theory and is not capable of modeling mixed subsonic/supersonic flows or shock waves. These restrictions result from the assumptions made for small perturbation theory, and any cases outside these restrictions should be viewed with caution; however, VTXCHN has been applied to blunt nose shapes such as spheroids or ellipsoids with good success. Typical missile shapes with slender noses pose no problems to the method.

Source distribution.- The following suggestions should be observed when using the source distribution calculation in VTXCHN. The source distribution in VTXCHN places three-dimensional point sources on the axis of the body (or equivalent body in a noncircular case). For subsonic Mach numbers, it is necessary to close the body to calculate a smooth source distribution. Generally, the body can be closed at its base by including a smooth boattail, and a successful technique for most cases is to close the model with its nose. The source distribution does not handle rapid changes or discontinuities in body slope well.

The source distribution calculation often has a problem with short pointed noses as well. Short blunted noses seem to cause no difficulty because they resemble the nose of a Rankine body, a single point source in a uniform stream. Sharp pointed noses often cause an oscillation in the source strength on the afterbody resulting in an oscillation in the

velocities and thus an oscillation in the axial pressure distribution. This has been observed with a 2-caliber ogive nose but was not apparent for a 2.5-caliber ogive. The oscillations were minor in their effect on the total calculation and result, but the user should be aware of their possibility.

Incidence angle.- The well-known and little-understood phenomenon of wake asymmetry at large incidence angles ($\alpha_c > 30°$) is available as an option in VTXCHN. As described in Reference 1, the naturally symmetric nature of the vortex shedding analysis must be perturbed to produce an asymmetric solution. The user must be aware of the limitations associated with this portion of the code in order to apply appropriate judgement in the evaluations of the results. Based on the author's experience with asymmetry, care must be taken in the choice of the perturbation parameter and its effect on the results. This is to serve as a warning, and the user should be aware that this portion of the code is in need of additional development.

Transition.- The transition capability included in the code for smooth bodies is in an early stage of development. The character of the vortex wake, whether originating from laminar or turbulent separation points, has an important effect on the predicted nonlinear aerodynamics characteristics. As previously discussed (Ref. 1), additional development is needed to better understand the origin and length of the transition regions. The user is cautioned to be very careful in the interpretation of predicted results in flow regimes which may be in a transition region as defined by Lamont in Reference 33.

The transition option in the program is not applicable to chine cross sections. With chine cross sections, separation is fixed at the sharp edges.

Secondary separation.- The capability to predict secondary separation or separation in the reverse flow region on the lee side of the body is included in VTXCHN. As discussed in a later section, there are certain flow conditions in which secondary separation has an important role; for example, asymmetric shedding at large incidence angles. Numerical problems associated with tracking the secondary vorticity have been observed, and some additional effort is required to make secondary separation a useful option. Therefore, it is

recommended that this option be treated as a research feature and not used for production calculations.

Error Messages and Stops

The code VTXCHN has numerous internal error messages. These messages are generally explicit and are described below. There are several execution terminations at numbered stops within the program. These are described in the table below with some suggestions to correct the problem.

The error message "CONVERGENCE NOT OBTAINED IN INTEGRATION" is printed out when the trajectory calculation does not converge within the specified tolerance, E5. Also printed out is the axial station, XI, and the integration interval, H. This error results in a STOP 40 which is discussed in the table to follow.

In the calculation of the source distribution it is possible to get the message "MATRIX IS SINGULAR." This occurs when one of the pivot elements in the influence matrix is zero. This error results in a STOP 300.

The other major error messages are found in the numerical conformal mapping routine CONFOR. The message "***ERROR IN THE SUM OF EXTERIOR ANGLES***" is printed if the routine has difficulty calculating appropriate body angles within a specified tolerance. Another message "***COEFFICIENT AN(1) = __ GREATER THAN +- 0.0001 AFTER ITERATIONS OUT OF __" is printed on the rare occasions when the mapping procedure is having difficulty converging on a solution. These messages are informational and do not result in a program STOP. However, the user is advised to check the transformed shape carefully with the actual shape before using the results.

Termination Message	Description
STOP 1	This is the normal stopping condition. Program VTXCHN

STOP 40 The vortex trajectory integration has failed to converge at an axial station. This problem is usually caused by: (1) two or more vortices in close proximity rotating about one another so rapidly that the integration subroutine cannot converge on a solution, or (2) a vortex is too near the body surface. These situations are often dependent on specific flow conditions and the body shape. The following steps should be tried to resolve the problem. Increase the integration tolerance E5, or increase the size of the combination parameter RGAM so that it is greater than the distance between the troublesome vortices. It often helps to increase the integration interval DX and restart the calculation procedure from a previous station. Subroutine BODY

STOP 41 The vortex trajectory calculation has resulted in a vortex inside the body This is a rare but serious problem which indicates a major problem with the solution. Subroutine BODY

STOP 44 The total number of shed vortices exceeds 200. To correct this, combine some vortices and restart the calculation, or increase the integration interval, DX, so that fewer vortices are shed. Subroutine BODY

STOP 45 The maximum number of positive or negative primary separation vortices exceeds 70. Use the same remedy as for STOP 44. Subroutine BODY

STOP 46 The maximum number of positive or negative secondary (reverse flow) separation vortices exceeds 30. Use the same remedy as for STOP 44 but only combine like vortices. If one of the above steps does not work, the reverse flow calculation can be turned off by setting NSEPR = 0. Subroutine BODY

STOP 201,202 There is an error in the vortex tables in subroutine VTABLE. Check the input values of NBLSEP, NSEPR, NVP, NVM, NVA, NVR, and RGAM in Items 1 through 6.

STOP 300 There is a singular influence matrix in the solution for the three-dimensional source distribution. Check the input geometry for errors. Subroutine INVERS

STOP 301 The maximum number of iterations is exceeded in the source calculation. Check the input geometry. This problem can occur if the body has a long slender nose followed by a cylindrical section and then a long slender tail. If this is the case, one solution is to close the body off with a blunter and/or shorter tail. Subroutine SORDIS

Input Description

This section describes the input data and format required by program VTXCHN. The input formats are shown in Figure 22, and the definitions of the individual variables are provided in the following paragraphs. Note that some length parameters in the input list are dimensional variables; therefore, special care must be taken that all lengths and areas are input in a consistent set of units.

The remainder of this section includes a description of each of the input variables and indices required for the use of program VTXCHN. The order follows that shown in Figure 22 where the input format for each item and the location of each variable on each input line is presented. Data input in I-format are right justified in the fields, and data input in F-format may be placed anywhere in the field and must include a decimal point.

Item 1 is a single input line containing 15 integer flags. These flags are right justified in a five column field and are used to specify several options available in VTXCHN.

Item	Variable	Description
1 (15I5)	NCIR	Cross section flag, determines the type of body cross section. = 0, circular body = 1, elliptical body = 2, arbitrary body, similar cross section at all axial stations = 3, arbitrary body, nonsimilar cross sections
	NCF	Mapping flag, specifies whether the required mapping is input or calculated. (NCIR = 2 or 3) = 0, calculate mapping = 2, input mapping
	ISYM	Vortex shedding symmetry flag. = 0, symmetric shedding, (assumes symmetry to save computation time) = 1, nonsymmetric shedding, (if PHI ≠ 0 in item 5 ISYM = 1)
	NBLSEP	Separation flag. = 0, no separation = 1, laminar separation = 2, turbulent separation
	NSEPR	Reverse flow or secondary separation flag. = 0, no reverse flow separation (preferred) = 1, reverse flow separation
	NDFUS	Vortex core model flag. = 0, potential vortex model = 1, diffuse vortex model (preferred)

NDPHI — Two-dimensional unsteady pressure term flag.

= 0, omit $\partial\phi/\partial x$ term in C_p equation

= 1, include $\partial\phi/\partial x$ term (preferred)

INP — Nose force flag.

= 0, estimate nose forces ahead of the first axial station (preferred)

= 1, zero nose forces ahead of the first axial station (for restart calculation)

NXFV — Number of x stations at which the flow field is calculated and/or special output is generated. ($0 \le NXFV \le 8$)

NFV — Number of field points for flow field calculation. ($0 \le NFV \le 500$)

NVP — Number of $+\Gamma$ vortices on +y side of body for a restart calculation. ($0 \le NVP \le 70$)

NVR — Number of reverse flow vortices on +y side of body for a restart calculation. ($0 \le NVR \le 30$)

NVM — Number of $-\Gamma$ vortices on -y side of body for a restart calculation. ($0 \le NVM \le 70$)

NVA — Number of reverse flow vortices on -y side of body for a restart calculation. ($0 \le NVA \le 30$)

NASYM — Asymmetric vortex shedding flag. (not used on chine portion of body)

= 0, no asymmetry

= 1, forced asymmetry (not recommended)

Item 2 is a single input line containing 3 integer flags. The first flag NVPHI controls how $d\phi/dx$ is calculated for the vortices, the second flag specifies whether the body has a chine shaped section, and the third flag specifies whether the dA_k/dx term of Equation (9b) is included in dv/dx.

Item	Variable	Description
2 (3I5)	NVPHI	$d\phi/dx$ flag, specifies how vortices are treated in the $d\phi/dx$ calculation. =-1, all vortices are considered independent for the $d\phi/dx$ calculation (preferred) ≥ 0, the most recent NVPHI vortices (on each side of the body) are considered independent for the $d\phi/dx$ calculation, and the remaining vortices are included by a centroid representation. The NVPHI vortices considered independently can be considered as the feeding sheet. NVPHI =-1 is suggested.
	NCHINE	chine flag, determines whether the body has a chine shaped cross section. = 0, no chine section, body determined by NCIR = 1, chine section for all or part of the body
	NDADT	flag which determines whether the term in Equation (9b) involving dA_k/dx is included in the calculation of dv/dx. dA_k/dx is calculated numerically by the program. = 0, dA_k/dx term not included in dv/dx = 1, dA_k/dx term is included in dv/dx

Item 3 is a single input line containing 10 integer flags/parameters. These values are used to specify several options available in VTXCHN.

Item	Variable	Description
3 (10I5)	NHEAD	Number of title lines in Item 3. (NHEAD > 0)
	NPRNTP	Pressure distribution print flag. = 0, pressure distribution output only at special output stations (NXFV > 0) = 1, pressure distribution output at each x station
	NPRNTS	Vortex separation print flag. = 0, no separation output = 1, separation point summary (preferred) = 2, detailed separation calculation (for diagnostic purposes only)
	NPRNTV	Vortex field summary output flag. = 0, vortex field is printed at special output stations only (NXFV > 0) = 1, vortex field is printed at every x station
	NPLOTV	Vortex field printer-plot flag. = 0, no plots = 1, plot full cross section, constant scale = 2, plot half cross section, constant scale = 3, plot full cross section, variable scale

NPLOTA — Additional output flag. Option to have pressure distribution, vortex field summary, and a plot of the vortex field regardless of the above set options.

= 0, no additional output

= 1, additional output only at special x stations (NXFV > 0)

= 2, additional output at each station

NTH — Numerical conformal mapping angle flag.

= 0, calculate circle θ's for mapping at 5° increments (preferred)

= 1, input θ's

NCORE — Vortex core radius flag.

= 0, maximum allowable local vortex core size is .05*D

= 1, no upper limit on the local vortex core size, the vortex core size is given by RCORE*D

NSKIN — Axial skin friction drag estimation flag.

= 0, no skin friction estimation

= 1, axial skin friction estimated

NCOMP — Compressibility correction flag.

= 0, incompressible calculation

= 1, compressibility correction applied (Mach number must be input in Item 6)

Item 4 is a set of NHEAD title/summary lines which are printed at the top of the first output page. They are reproduced in the output just as they are input.

Item	Variable	Description
4 (20A4)	TITLES	NHEAD title/summary lines to be output on first page.

Item 5 is a single input line containing reference information needed to form the aerodynamic coefficients.

Item	Variable	Description
5 (5F10.5)	REFS	Reference area, S_{ref}. REFS > 0.
	REFL	Reference length, l_{ref}. REFL > 0.
	XM	Axial position of the moment center, measured from the body nose.
	SL	Body length, L.
	SD	Maximum body diameter, D.

Item 6 is a single input line containing the flow conditions.

Item	Variable	Description
6 (3F10.5)	ALPHAC	Angle of incidence (degrees). ($0^\circ \leq \alpha_c < 90^\circ$)
	PHI	Angle of roll, ϕ (degrees). For chine bodies the user should be aware that separation is forced at the sharp edge of the chine regardless of the value of PHI. It is the user's responsibility to determine the limit of PHI for a given chine shape.

	RE	Reynolds number based on maximum body diameter, $(V_\infty D/\nu)$.
	MACH	Free-stream Mach number.

Item 7 is a single input line which specifies the axial extent of the run, the transition region, and parameters associated with the vortex wake

Item	Variable	Description
7 (8F10.5)	XI	Initial x station, XI > 0, dimensional quantity. (Note: XI ≥ DX/2)
	XF	Final x station, XF > XI, dimensional quantity.
	DX	x increment for vortex shedding calculation. Typical value, DX ≈ D/2. For bodies with chine cross sections it is recommended that DX be between 0.10*D and 0.25*D
	XTR1	Beginning of transition region, dimensional quantity. This option is not available on a chine portion of the body.
	XTR2	End of transition region, dimensional quantity. This option is not available on a chine portion of the body.

EMKF — Minimum shed vortex starting distance from the body surface. This value is not used on a chine portion of the body.

= 1.0, shed vortices located according to stagnation point criterion

> 1.0, minimum radii position of shed vortices. Typical value, EMKF = 1.05

RGAM — Vortex combination factor.

= 0.0, vortices are not combined (preferred)

> 0.0, radial distance within which vortices are combined

VRF — Vortex reduction factor, δ_1 to account for observed decreases in vortex strength.

= 0.6, for bodies with bases

= 1.0, for closed bodies

If NCHINE = 1, this parameter is not used.

Item 8 is a single input line containing the integration tolerance, asymmetry perturbation information, alternate separation criteria, and the core radius.

Item	Variable	Description
8 (8F10.5)	E5	Error tolerance for the vortex trajectory calculation. Typical range, E5 = 0.01 to 0.05, or larger if appropriate.
	XTABL	Location at which a table of points on the body and on the circle is printed. = 0.0, no table of points is printed (preferred) > 0.0, table of points for all x < XTABL

XASYMI — Initial x station for asymmetric perturbation. This option is not available on a chine portion of the body.

XASYMF — Final x station for asymmetric perturbation. This option is not available on a chine portion of the body.

DBETA — Angular displacement of separation points for asymmetry perturbation. This option is not available on a chine portion of the body.

SEPL — Stratford laminar criterion. (not used on chine portion of body)
= 0.0, program uses SEPL = .087 (preferred)
> 0.0, program uses input value

SEPT — Stratford turbulent criterion. (not used on chine portion of body)
= 0.0, program uses SEPT = .350 (preferred)
> 0.0, program uses input value

RCORE — Ratio of the local core radius to the local body diameter. Default value is .025. Maximum allowable value is $.025*D/r_o$.

Item 9 is a single input line containing two flags for the source distribution. The source distribution may be input (NSOR > 0), calculated from the body geometry (NSOR = -1), or omitted from the solution (NSOR = 0). If the Mach number is not equal to zero (NCOMP > 0), then a different source distribution is required for each Mach number.

Item	Variable	Description
9 (2I5)	NSOR	Source distribution flag. =-1, calculate the source distribution from the geometry input = 0, no sources (not recommended) > 0, number of sources to be input
	NPRT	Source distribution print flag. = 0, output source locations and strengths = 1, above output plus input and source geometry comparison = 2, above output plus source-induced surface velocities

Omit Items 10 and 11 if NSOR ≤ 0.

Items 10 and 11 contain the nondimensional source locations and nondimensional source strengths, respectively.

Item	Variable	Description
10 (6E12.5)	XSRC	Nondimensional source locations, x/L. (NSOR values, 6 per input line) x/L may be greater than 1.0.

Item	Variable	Description
11 (6E12.5)	QS	Nondimensional source strengths, $Q/4\pi L^2 V_\infty \cos\alpha_c$.

Items 12 through 15 contain the body geometry information. This information must be included for all bodies whether circular or noncircular.

Item	Variable	Description
12 (I5)	NXR	Number of entries in the body geometry table. ($1 \leq NXR \leq 101$)

Item	Variable	Description
13 (8F10.5)	XR	Nondimensional axial stations in the geometry table, x/L. (NXR values, 8 per input line)

Item	Variable	Description
14 (8F10.5)	R	Nondimensional equivalent area body radius at the NXR x/L-stations, r_{eq}/L (NXR values, 8 per input line).

Item	Variable	Description
15 (8F10.5)	DR	Body slope at the NXR x/L-stations, dr_{eq}/dx. (NXR values, 8 per input line)

Omit Items 16 and 17 if NCIR ≠ 1.

Items 16 and 17 contain the nondimensional horizontal and vertical half axis lengths if the cross sections are elliptical, NCIR = 1.

Item	Variable	Description
16(a) (8F10.5)	AE	Nondimensional horizontal half axis length of the elliptical cross section at the NXR x/L-stations, a/L. (NXR values, 8 per input line)

Item	Variable	Description
16(b) (8F10.5)	BE	Nondimensional vertical half axis length of the elliptical cross section at the NXR x/L-stations, b/L. (NXR values, 8 per input line)

Item	Variable	Description
17(a) (8F10.5)	DAE	Slope of horizontal meridian of the elliptical cross section at the NXR x/L-stations, da/dx. (NXR values, 8 per input line)

Item	Variable	Description
17(b) (8F10.5)	DBE	Slope of vertical meridian of the elliptical cross section at the NXR x/L-stations, db/dx. (NXR values, 8 per input line)

Omit Items 18(a) and 18(b) if NCIR = 0.

Items 18(a) and 18(b) contain the mapped body geometry information at the NXR x/L-stations specified in Item 13.

Item	Variable	Description
18(a) (8F10.5)	RO	Nondimensional transformed (mapped) body radius at the NXR x/L-stations, r_o/L (NXR values, 8 per input line). For an ellipse, $r_o = (a + b)/2$.

Item	Variable	Description
18(b) (8F10.5)	DRO	Body slope at the NXR x/L-stations, dr_o/dx. (NXR values, 8 per input line)

Omit Items 19 through 27 if NCIR < 2.

Items 19 through 27 are used to specify a body of arbitrary cross section shape. This body should also be polygonal in shape (i.e., negative interior angle can cause problems in the numerical conformal mapping procedure).

Omit Item 19 if NTH = 0.

Item	Variable	Description
19 (8F10.5)	TH	Special table of circle angles for arbitrary body mapping, (i = 1, 73), to be used only if the density of points on the cross section needs adjusting to improve the resolution of pressure distribution. Not recommended under normal conditions.

Item	Variable	Description
20(a) (2I5)	MNFC	Number of mapping coefficients for the arbitrary body. (MNFC ≤ 100). Generally good mappings can be obtained with 20 to 30 coefficients.
	MXFC	Number of axial stations at which the arbitrary body is specified. (1 ≤ MXFC ≤ 10). For a similar shape at all cross sections, MXFC=1.

Item	Variable	Description
20(b) (8F10.5)	XFC	x stations at which the arbitrary body is specified. (MXFC values, 8 per input line). For a similar cross section body, MXFC=1, XFC(1) ≤ XI.

Omit Item 21 if NCHINE ≤ 0

Item 21 is a set of MXFC integers to indicate which input corner point of each input cross section is to be considered as the chine edge. Figure 23(b) illustrates a chine and the choice of NCSEP. The input corner points are read in Items 22 and 23. (MXFC values, 10 per input line).

Item	Variable	Description
21 (I5)	NCSEP	Number of the input corner point defining the chine edge. Corner points are read in items 22 and 23. It is recommended that NCSEP be the same for all input chine cross sections. 0 ≤ NCSEP ≤ NR. Omit item 21 if NCHINE ≤ 0.

Omit Items 22 and 23 if NCF > 0.

Items 22 and 23 are repeated for each of the MXFC axial stations when the transformation coefficients are to be calculated (NFC = 0).

Item	Variable	Description
22 (I5)	NR	Number of points describing the arbitrary body cross section ($2 \leq NR \leq 30$). (Note: NR must be the same for all x stations.)

Item	Variable	Description
23(a) (6E12.5)	XRC	Horizontal coordinates of the arbitrary body cross section. (NR values, 6 per input line). The convention for ordering the coordinates from bottom to top in a counter-clockwise fashion is observed, Figure 23. This corresponds to inputting the +y side geometry. Right/left body symmetry is required.
23(b) (6E12.5)	YRC	Vertical coordinates of the arbitrary body cross section. (NR values, 6 per input line). See Figure 23.

Omit Items 24 through 27 if NCF = 0.

Items 24 through 27 are repeated as a group for each of the MXFC axial stations if the numerical transformations are available from a previous calculation. The only purpose for providing the option to input the mapping parameters is to eliminate the need to recompute the numerical mapping in subsequent runs and save computation time.

Item	Variable	Description
24 (2F10.5)	ZZC	Mapping offset distance.
	RZC	Radius of transformed cross section.

Item	Variable	Description
25 (I5)	NR	Number of points describing the arbitrary body cross section (NR ≤ 30). (Note: NR must be the same for all x stations.)

Item	Variable	Description
26(a) (6E12.5)	XRC	Horizontal coordinates of the arbitrary body cross section. (NR values, 6 per input line). See Figure 23 and convention for Item 23.
26(b) (6E12.5)	YRC	Vertical coordinates of the arbitrary cross section. (NR values, 6 per input line). See Figure 23.
26(c) (6E12.5)	THC	Circle angles, θ, of body points. (NR values, 6 per input line)

Item	Variable	Description
27 (6E12.5)	AFC	Mapping coefficients. (MNFC values, 6 per input line)

The derivative of the mapping required in Equation (9b) is calculated by the program.

Omit Items 28 - 29 if NCHINE ≤ 0.

Item 28 is a single input line containing information required to start the solution by approximating the chine as a thin strake on a circular body.

Item	Variable	Description
28 (I5,F10.5)	NSTRTC	number of axial stations at which the vortex lattice approximation of the chine is used to start the solution. A value between 0 and 5 generally works the best, but the user is encouraged to investigate the effect of this parameter.
	FVCHN	fraction of the exposed strake span where the boundary condition is applied to determine the initial chine strength using a vortex lattice approximation. Suggested value 0.50.

Item 29(a) is a single input line containing the starting and ending axial stations of the chine portion of the body.

Item	Variable	Description
29(a) (2F10.5)	XCHNB	axial station at which chine separation begins.
	XCHNE	axial station at which chine separation ends.

Item 29(b) is a single input line containing three values of NCIR for a chine body. See input Item 1 for a description of NCIR.

Item	Variable	Description
29(b) (3I5)	NCH(1)	value of NCIR for portion of body in front of axial station XCHNB. Only NCIR = 0, 2 ,or 3 is available here. If the body has an elliptical nose section, it should run as a noncircular body (NCIR = 2 or 3).

	NCH(2)	value of NCIR for portion of body between axial station XCHNB and XCHNE. For the chine section, NCIR is 2 or 3. If NCH(1) = 0 and NCH(2) = 3, then the first input body cross section should be a circle with a radius equal to the body radius at the start of the chine section. This is required to ensure transition from the circluar portion of the body to the chine portion.
	NCH(3)	value of NCIR for portion of body after axial station XCHNE. Only NCIR = 0, 2 ,or 3 is available here. If the body has an elliptical afterbody section, it should run as a noncircular body (NCIR = 2 or 3).

Item 29(c) is a single input line containing two values of NBLSEP for a chine body. See input Item 1 for a description of NBLSEP.

Item	Variable	Description
29(c) (2I5)	NCBL(1)	value of NBLSEP for portion of body in front of axial station XCHNB.
	NCBL(3)	value of NBLSEP for portion of body after axial station XCHNE.
		The value of NCBL(2) is set in the code but is not used.

Item 29(d) is a single input line containing two values of VRF for a chine body. See input Item 7 for a description of VRF.

Item	Variable	Description
29(d)(2F10.5)	VRFC(1)	value of VRF for portion of body in front of axial station XCHNB. See input Item 7 for recommended values.
	VRFC(3)	value of VRF for portion of body after axial station XCHNE. See input Item 7 for recommended values.
		The value of VRFC(2) is set in the code but is not used.

Omit Items 30 and 31 if NXFV = 0.

Item 30 is a single input line containing the x stations at which additional output is printed and/or calculated if NXFV > 0.

Item	Variable	Description
30 (8F10.5)	XFV	x stations at which additional output is printed or calculated. (NXFV values, 8 values maximum)

Omit Item 31 if NFV = 0.

Item 31 is a set of NFV input lines which contains the coordinates of the field points where the velocity components are to be calculated at each of the axial stations in Item 30.

Item	Variable	Description
31 (2F10.5)	YFV,ZFV	y and z coordinates of the field points for the velocity field calculation. (NFV input lines, maximum of 500). It is recommended that all points lie outside the body surface at all axial stations.

Omit Items 32 through 37 if NVP + NVR + NVM + NVA = 0

Items 32 through 36 provide information needed to restart the calculation procedure. It is not necessary to input all four types of vorticity in a restart calculation. Note that program VTXCHN write a file to FORTRAN Unit 1 which contains the required input for Items 32 through 36.

Item 32 is a single input line containing the nose force and moment coefficients at the restart point; that is, X = XI. These values may be set equal to zero, but the resulting forces and moments from the current calculation will be in error.

Item	Variable	Description
32 (5F10.5)	CN	Normal-force coefficient
	CY	Side-force coefficient
	CA	Axial pressure force coefficient
	CDI	Axial skin friction force coefficient
	CM	Pitching-moment coefficient
	CR	Yawing-moment coefficient
	CSL	Rolling-moment coefficient

Omit Items 33 if NVP = 0.

Item 33 is a set of NVP input lines which specify a cloud of positive primary body separation vorticity, usually on the right side of the body. The variable XSHEDP associated with each vortex is used only to identify individual vortices and permit the user to follow individual vortices during the calculation.

Item	Variable	Description
33 (4F10.5)	GAMP	+y primary vorticity, Γ/V_∞.
	YGP	Horizontal coordinate, y, of vortex.
	ZGP	Vertical coordinate, z, of vortex.
	XSHEDP	Origin of the vortex.

Omit Item 34 if NVR = 0.

Item 34 is a set of NVR input lines which specify a cloud of reverse flow (secondary) body separation vorticity. This array is a convenient way to put an arbitrary cloud of additional vorticity which is to be maintained separately from the other body vorticity in the field.

Item	Variable	Description
34 (4F10.5)	GAMR	+y reverse flow vorticity, Γ/V_∞.
	YGR	Horizontal coordinate, y, of vortex.
	ZGR	Vertical coordinate, z, of vortex.
	XSHEDR	Origin of the vortex.

Omit Item 35 if ISYM = 0 or NVM = 0.

Item 35 is a set of NVM input lines which specifies a cloud of negative primary body separation vorticity, usually on the left side of the body. In the case of a symmetric flow field (ISYM=0), this block of vorticity is automatically defined as the mirror image of the positive vorticity input in Item 33.

Item	Variable	Description
35 (4F10.5)	GAMM	-y primary vorticity, Γ/V_∞.
	YGM	Horizontal coordinate, y, of vortex.
	ZGR	Vertical coordinate, z, of vortex.
	XSHEDR	Origin of the vortex.

Omit Item 36 if ISYM = 0 or NVA = 0.

Item 36 is a set of NVA input lines which specifies a cloud of reverse flow (secondary) body separation vorticity. This block of vorticity is analogous to Item 34, and it is omitted if NVA = 0 or if ISYM = 0. As with the previous item, this block of vorticity is automatically defined as the mirror image of the negative vorticity input as Item 34 if symmetry is required by ISYM = 0.

Item	Variable	Description
36 (4F10.5)	GAMA	-y reverse flow vorticity, Γ/V_∞.
	YGA	Horizontal coordinate, y, of vortex.
	ZGA	Vertical coordinate, z, of vortex.
	ZSHEDA	Origin of the vortex.

Item 37 contains the pressure distribution at the initial x station for a restart calculation. These values should be obtained from a previous run. If a symmetric case is being considered, ISYM=0, only half of the pressure distribution is needed (37 points). for a asymmetric case 73 points are required.

Item	Variable	Description
37 (3F10.5)	YBO	y body coordinate.
	ZBO	z body coordinate.
	CPO	pressure coefficients at (YBO, ZBO).

This concludes the input deck for a single run of VTXCHN. The code is not set up to stack input for multiple cases because of the sometimes long and often unpredictable run times.

Input Preparation

In this section, some additional information is provided to assist the user in the preparation of input for certain selected problems. The previous section on the input description must be used to understand the individual variables which go into VTXCHN, and this section will permit the user to select the appropriate input to get optimum results from the code.

Numerical mapping.- The specification of the appropriate numerical mapping parameters (Items 18 through 28) depends on the shape of the cross section. In the interest of optimum computation time, the fewest possible terms in the transformation series (MNFC in Item 19) should be used which will produce an adequate mapping. Each different shape should be checked by the user to determine the proper number of coefficients. For example, a simple cross section which is similar to a circle may require as few as 10 coefficients. Others may require as many as 30 coefficients for an excellent mapping. If a large number of calculations are to be made for a noncircular shape, it is worthwhile for the user to try different numbers of coefficients in an effort to find an optimum number. Not only should the shapes be compared carefully, the unseparated flow pressure coefficients should be compared to evaluate the quality of the mapping.

The numerical mapping now included in VTXCHN has been used for a variety of cross section shapes, and some problems have been observed. One general problem area is bodies with concave sides. The mapping procedure has difficulty converging on a set of coefficients. Usually the body shape can be modified slightly, to give the concave region a flat or slightly convex shape, and the mapping converges easily. This small change in the shape probably has very little effect on the predicted pressure distribution. This is an example of the type of problem for which the user should be alert. For chine cross sections,

several problems can occur due to concave or drooped sides. The user may need to be ceative in coming up with the best approximation of the real cross section. This may require specifying fewer points to describe the body cross section in order to obtain a good numerical mapping.

Integration interval.- Choice of the appropriate integration interval (DX in Item 7) depends to a large extent on the type of results of interest. If the user is interested in detailed nose loads and separation on the nose where the radius is changing rapidly, the interval should be smaller than the recommended D/2. On very long bodies, the recommended interval is usually adequate for accurate predictions. For chine bodies the interval is recommended to be smaller than D/4 and as small as D/10, but smaller intervals can cause numerical problems.

Vortex core.- The core size specification is referenced to the local body diameter (RCORE in Item 8). The default value is 0.025, and this value is adequate for most cases. The larger the core radius specified, the more the vortex effects are reduced. To eliminate the possibility of negating the vortex effect entirely, a maximum vortex core of .05 times the maximum body diameter is built into the code. Except in unusual situations, the default value is recommended.

Chine Sample Cases

In this section, two sample input cases are described to illustrate the use of program VTXCHN to model bodies with chine cross section shapes. Nine sample case inputs dealing with circular, elliptic, and noncircular bodies are presented in Reference 1. The purpose of the following sample cases is to point out the available features and options for chine shaped bodies. and to provide a range of sample inputs which will help users prepare input for specific cases.

Sample Case 1.- Chine Sample Case 1, Figure 24, is a test run based on the chine body in Reference 32. This run will also be used as the sample output case in the next section. It

is recommended that this case be run initially to provide a check with the results presented in a following section.

Input Item 1 indicates that the case consists of a body with noncircular/nonsimilar cross sections, NCIR = 3, and a symmetric vortex wake, ISYM = 0. The mapping flag NCF = 0 indicates that the numerical mapping is calculated. The separation criteria is laminar, NBLSEP = 1, but no reverse flow separation is to be computed, NSEPR = 0. A diffuse vortex core model is to be used, NDFUS = 1, and the two-dimensional unsteady pressure term is included in pressure calculation, NDPHI = 1. INP = 0 indicates that the nose forces ahead of the first axial station will be estimated. NXFV = 0 and NFV = 0 indicate that no special output stations or field points are to be read in Items 30 and 31. No inital vortices are to be read, NVP = NVR = NVM = NVA = 0, and asymmetric shedding is not forced, NASYM = 0.

Input Item 2 contains three additional flags. NVPHI = -1 indicates that all vortices are considered independent for the $d\phi/dt$ calculation, NCHINE = 1 indicates that the body has a chine cross section portion, and NDADT = 0 indicates that the dA_k/dx term in Equation (9b) is omitted. The chine flag will require further input which will overide some of the program control flags in input item 1. When a body with a chine section is being investigated, the forced asymmetry (NASYM) option is not available. For chine bodies the values of NCIR and NBLSEP are reset by information read in input Items 29(b) and (c).

Input Item 3 indicates there will be four title cards input in Item 4. NPRNTP = 1 specifies the pressure distribution be output at all x stations, and NPRNTS = 1 causes a summary of the separation points to be output at all x stations. The flag NPRNTV = 1 results in a summary of the vortex field at all axial stations. NPLOTV = 3 and NPLOTA = 2 specifies that a line printer plot of the vortex field is created at all x stations if separation has occurred. NTH = 0 indicates that the circle θ's are calculated every 5 degrees by the program, and NCORE = 0 set the maximum core size to 0.05*D. NSKIN = 0 suppresses estimation of the skin friction on the body, and NCOMP = 0 specifies an incompressible calculation.

Input Item 4 is a set of four title/summary cards which are printed at the top of the first output page.

Input Item 5 contains the reference information for the run. The reference area is REFS = 22.145, the reference length is REFL = 8.70, and the moment center, XM, is located at station 23.00. The length of the body, SL, is 73.40, and the maximum body diameter, SD, is 8.70.

Item 6 contains the flow conditions. The angle of attack, ALPHAC, is 20 degrees, and there is no roll angle, PHI = 0.0. The Reynolds number, RE, is 1000000, and the Mach number is 0.0.

Item 7 specifies run parameters. The calculation procedure begins at x station, XI, 0.50 and continues to station, XF, 14.5 in DX increments of 0.50. A transition region is not specified, XTR1 = XTR2 = 0.0. Separation vortices are initially placed a minimum 1.05 radii, EMKF, from the axis of the missile. Vortices will not be combined, RGAM = 0.0. The vortex reduction factor, VRF, is set to 1.0. For chine bodies the value of VRF is reset by information read in input Item 29(d). For chine bodies the input values of XTR1, XTR2, and EMKF are not used.

The only items of interest in input Item 8 are the tolerance for the vortex trajectory calculation, E5, and the vortex core size, RCORE. E5 is set to 0.05, a typical value, and RCORE is set to 0.05. Some additional comments on the tolerance parameter E5 are contained in the previous section on Error Messages and Stops.

Input Item 9 contains the flags for the source distribution calculation. NSOR = -1 specifies the source distribution is unknown and is to be calculated by VTXCHN. NPRT = 2 provides for additional output regarding the source distribution. This output includes a comparison of the input geometry and the geometry calculated from the source distribution which provides a good means of checking the calculated source distribution. Also printed are the surface velocities calculated by the source distribution.

Input Item 12 contains NXR, the number of entries in the body geometry table. Items 13, 14, and 15 are the axial stations, XR, the corresponding body radii, R, and the body slopes, DR, respectively. The axial stations and the radii are nondimensionalized with respect to the body length, SL. The values of R and DR should correspond to an equivalent area body.

Input Items 18(a) and 18(b) contain the mapped body radius, RO, and slope, DRO, at the axial stations specified in Item 13.

Input Item 20(a) specifies that 30 mapping coefficients are used, MNFC, and the body cross section shape is specified at 3 axial stations, MXFC. The three axial stations where the cross sections are specified are read in input Item 20(b), XFC = 7.19, 13.56, 19.94.

Input Item 21 is included for chine bodies. Three integers are specified, NCSEP, which indicate that the seventh corner point is taken as the chine edge for the three cross section shapes to be read in Items 22 and 23.

Input Items 22 and 23 are repeated for each input cross section (MXFC = 3). Item 22, NR, specifies that 12 corner points are used to describe the cross section. XRC and YRC in Items 23(a) and 23(b) are the corner points describing the cross section.

Input Items 28 and 29 are included for chine bodies. Item 28 contains information to start the chine solution. Item 28, NCSTRT, indicates that the chine initialization routine is to be used for the first 8 axial stations, and the boundary condition is applied at 0.25, FVCHN, of the exposed strake span.

Input Item 29(a) specifies that the chine cross section starts at axial station 0.00, XCHNB, and that it end at axial station 30.00, XCHNE.

Input Item 29(b) contains values of NCIR for the portion of the body in front of XCHNB, for the portion of the body between XCHNB and XCHNE, and for the body

sections after XCHNE. NCH (NCIR) is set to 3 for all sections of the body. The values of NCIR specified here overide the value specified in input Item 1.

Input Item 29(c) specifies the boundary layer flag, NBLSEP, for the portions of the body before XCHNB and after XCHNE. Since the entire body has a chine cross section, these values are not significant.

Input Item 29(d) specifies the vortex reduction factor, VRF, for the portions of the body before XCHNB and after XCHNE. Since the entire body has a chine cross section, these values are not significant.

Sample Case 2.- Chine Sample Case 2, Figure 25, is an example of a body with a circular nose followed by a growing chine section.

Input Item 1 indicates that the case consists of a body with noncircular/nonsimilar cross sections, NCIR = 3, and a symmetric vortex wake, ISYM = 0. The mapping flag NCF = 0 indicates that the numerical mapping is calculated. The separation criteria is laminar, NBLSEP = 1, but no reverse flow separation is to be computed, NSEPR = 0. A diffuse vortex core model is to be used, NDFUS = 1, and the two-dimensional unsteady pressure term is included in pressure calculation, NDPHI = 1. INP = 0 indicates that the nose forces ahead of the first axial station will be estimated. NXFV = 0 and NFV = 0 indicate that no special output stations or field points are to be read in Items 30 and 31. No inital vortices are to be read, NVP = NVR = NVM = NVA = 0, and asymmetric shedding is not forced, NASYM = 0.

Input Item 2 contains two additional flags. NVPHI = -1 indicates that all vortices are considered independent for the $d\phi/dt$ calculation, and NCHINE = 1 indicates that the body has a chine cross section portion.

Input Item 3 indicates there will be five title cards input in Item 3. NPRNTP = 1 specifies the pressure distribution be output at all x stations, and NPRNTS = 1 causes a summary of the separation points to be output at all x stations. The flag NPRNTV = 1

results in a summary of the vortex field at all axial stations. NPLOTV = 3 and NPLOTA = 2 specifies that a line printer plot of the vortex field is created at all x stations if separation has occurred. NTH = 0 indicates that the circle θ's are calculated every 5 degrees by the program, and NCORE = 0 set the maximum core size to 0.05*D. Skin friction is not estimated, NSKIN = 0, and NCOMP = 0 specifies an incompressible calculation.

Input Item 4 is a set of five title/summary cards which are printed at the top of the first output page.

Input Item 3 contains the reference information for the run. The reference area, REFS = 3.14159, is the cross sectional area at the end of the circular portion of the body, the reference length, REFL = 2.00, is the diameter at the end of the circular portion of the body, and the moment center, XM, is located at station 10.00. The length of the body, SL, is 20.00.

Item 6 contains the flow conditions. The angle of attack, ALPHAC, is 20 degrees, and there is no roll angle, PHI = 0.0. The Reynolds number, RE, is 1000000, and the Mach number is 0.0.

Item 7 specifies run parameters. The calculation procedure begins at x station, XI, 0.50 and continues to station, XF, 13.0 in DX increments of 0.50. A transition region is not specified, XTR1 = XTR2 = 0.0. Separation vortices are initially placed a minimum 1.05 radii, EMKF, from the axis of the missile. Vortices will not be combined, RGAM = 0.0. The vortex reduction factor, VRF, is set to 1.0. For the circular portion of the body the vortex reduction factor will be reset in input Item 29(d).

The only items of interest in input Item 8 are the tolerance for the vortex trajectory calculation, E5, and the vortex core size, RCORE. E5 is set to 0.03, a typical value, and RCORE is set to 0.05.

Input Item 9 contains the flags for the source distribution calculation. NSOR = -1 specifies the source distribution is unknown and is to be calculated by VTXCHN. NPRT = 2 provides for additional output regarding the source distribution..

Input Item 12 contains NXR, the number of entries in the body geometry table. Items 13, 14, and 15 are the axial stations, XR, the corresponding body radii, R, and the body slopes, DR, respectively. The axial stations and the radii are nondimensionalized with respect to the body length, SL. The values of R and DR should correspond to an equivalent area body.

Input Items 18(a) and 18(b) contain the mapped body radius, RO, and slope, DRO, at the axial stations specified in Item 13.

Input Item 20(a) specifies that 25 mapping coefficients are used, MNFC, and the body cross section shape is specified at 5 axial stations, MXFC. The five axial stations where the cross sections are specified are read in input Item 20(b), XFC = 6.00, 7.00, 13.00, 19.00, and 20.00.

Input Item 21 is included for chine bodies. Three integers are specified, NCSEP, which indicate that the tenth corner point is taken as the chine edge for the five cross section shapes to be read in Items 22 and- 23.

Input Items 22 and 23 are repeated for each input cross section (MXFC = 5). Item 22, NR, specifies that 19 corner points are used to describe the cross section. XRC and YRC in Items 23(a) and 23(b) are the corner points describing the cross section.

Input Items 28 and 29 are included for chine bodies. Item 28, NCSTRT, indicates that the chine initialization routine is not used.

Input Item 29(a) specifies that the chine cross section starts at axial station 6.00, XCHNB, and that it end at axial station 20.00, XCHNE.

Input Item 29(b) contains values of NCIR for the portion of the body in front of XCHNB, for the portion of the body between XCHNB and XCHNE, and for the body sections after XCHNE. NCH (NCIR) is set to 0 (circular) for the portion of the body in front

of station XCHNB. For XCHNB < X < XCHNE NCH is set to 3, and for the portion of the body after XCHNE NCH is set to 0.

Input Item 29(c) specifies the boundary layer flag, NBLSEP, for the portions of the body before XCHNB and after XCHNE. For both portions of the body the separation criteria is laminar, NCBL(1) = NCBL(3) = 1.

Input Item 29(d) specifies the vortex reduction factor, VRF, for the portions of the body before XCHNB and after XCHNE. For both portions of the body the vortex reduction factor is VRFC(1) = VRFC(3) = 0.6.

Output Description

A typical chine body output file from VTXCHN is described in this section. In general, the output quantities from VTXCHN are labeled and each page is headed with approximate descriptive information. The output from Chine Sample Case 1, Figure 24, requires 151 pages, and it will be described briefly page by page. Representative pages are shown in Figure 26.

The first output page contains the title/summary cards, the reference quantities, the flow conditions, the initial run conditions, and the run flags. Page 1, Figure 26(a), is simply an echo of the input parameters. Also contained on this page are the force and moment definitions. Page 2, Figure 26(b), echos the input body geometry, XR, R, and DR. The dimensional X and R values are also printed. For noncircular bodies, R and DR, correspond to an equivalent area body.

Pages 3 through 9, Figures 26(c) - 26(i), contain information from the three-dimensional source distribution calculation. Page 3, Figure 26(c), is a summary of the source placement and the body geometry at these locations. Page 4, Figure 26(d), shows the source locations and strengths, and pages 5 and 6, Figures 26(e) and 26(f) are a comparison of the input geometry shape, R/L(INPT), and the shape calculated from the source distribution R/L(S.D.). This comparison is indicative of the quality of the source distribution. A second

indication of difficulties with the source distribution will show up in the number of iterations required to find the proper shape, M-INDEX. If this number is less than four or five, the chances are good the source distribution is a good representation of the body. If this number is large, examine the input and predicted shapes carefully for problems. Pages 7 and 8, Figures 26(g) and 26(h), are the surface velocities calculated by the source distribution, and they should be examined to ensure that no exceedingly large velocities occur, another indication of a problem with the body model. Small oscillations in the velocities on the cylindrical portion of a body are to be expected.

Page 9, Figure 26(i), contains a summary of source locations and strengths, and the values on this page are in the correct format for input into VTXCHN for additional cases using the same geometry and Mach number. Also shown on this page are the mapped radius, RO and slope DRO.

Pages 10 through 23, Figures 26(j) - 26(w), contain output from the numerical mapping portion of the program. Page 10, Figure 26(j), contains the input and mapped corner points for the first noncircular chine cross section input, X = 7.19. Page 11, Figure 26(k), contains the mapping coefficients calculated, and pages 12 and 13, Figure 26(l) and 26(m), display the circle and body points used in the pressure calculation. For chine cross sections the chine edge point is indicated. Pages 14 through 21, Figures 26(n) - 26(u), contain the same information as pages 10 through 13, Figure 26(j) - 26(m), for the two additional chine sections input, X = 13.56 and 19.94.

Pages 22 and 23, Figures 26(v) and 26(w), contain a summary of the numerical mapping corner points and mapping coefficients. The information on these two pages can be used as input to the code if the same body needs to be run for different flow conditions.

Page 24, Figure 26(x), contains a summary of chine information. Information on this page describes how the chine solution is started, beginning and end of chine section, and program control variables for the different parts of the body.

Page 25, Figure 26(y), shows the pressure distribution at the first axial station before a vortex has been placed to satisfy the Kutta condition at the chine edge. The vortex required to satisfy the Kutta condition is printed at the bottom of this page.

Page 26, Figure 26(z), starts the output from the analysis part of the code. The first numeric line on page 26 contains the axial locations, the local radius, the body slope, and the transition Reynolds number, RETR. The predicted results on page 26 are a summary of the velocities and pressures on the circumference at this particular x station. The coordinates are dimensional, and the velocities are made dimensionless by the freestream velocity. The pressure coefficient is followed by the unsteady term $\partial\phi/\partial t$, velocities in the circle plane, and the value of the numerical mapping CS. The sharp chine edge is indicated.

Following the pressure distribution is a summary of the section loadings and the overall loadings up to the current section. CN(X), CY(X), and CA(X) are the normal-, side-, and axial-force coefficients per unit length, respectively. CN, CY, and CA are the overall normal-, side-, and axial-force coefficients from the nose to the current x station, respectively. CM, CR, and CSL are the pitching-, yawing-, and rolling-moment coefficients, respectively. XCPN and XCPY are the x locations of the centers of pressures for the normal and side forces, respectively.

Page 27, Figure 26(aa), contains a line printer plot of the vortex field at the first x station. The tracking of the vortex to the next axial station takes place after this line printer plot.

Page 28, Figure 26(ab), a summary of the vortex field at the next axial station, X = 1.0. The new vortex required to satisfy the Kutta condition at this station follows the summary of the vortex field table.

Pages 28 - 117 contain output for axial stations 1.0 to 14.5. The output for each axial station has the same form as that described for axial station 0.5 on pages 26 through 28, Figures 26(z) - 26(ab). The output for axial stations 4.5 and 14.5 are shown on pages 50 - 53, Figure 26(ac) - 26(af), and 114 - 117, Figures 26(ag) - 26(aj), respectively.

Page 118, Figure 26(ak), of the output file depicts the vortex field at the final axial station and contains a summary of the overall loads. Page 119, Figure 26(al), shows the pressure distribution at the final output station. This pressure distribution is required if a restart calculation is to be run starting at this final station.

CONCLUSIONS

An engineering prediction method based on a rational flow modeling technique and the associated code VTXCHN to predict the vortex shedding from forebodies with chines in subsonic flow at angles of attack and roll are described. Comparisons of measured and predicted aerodynamic characteristics and flow field quantities are used to verify the flow model and prediction method for a variety of configurations under a wide range of flow conditions. The method has proved successful in representing the principal features of the complex flow field on the lee side of these configurations at moderate angles of attack; therefore, it has application as an engineering or preliminary design technique directed at the prediction of nonlinear aerodynamic characteristics resulting from high angle of attack flows.

The prediction method described herein has further application as one component of a larger prediction method for complete configurations consisting of an arbitrary body and multiple fins. The ability to model the correct flow field in the vicinity of the body leads to the capability to calculate body separation wake-induced interference effects on fins and other control surfaces. The vortex shedding analysis and prediction techniques are also applicable for use in other codes; for example, the methods developed in this investigation can be transferred to higher order codes such as panel codes. This was demonstrated in the vortex shedding work reported in Reference 3 and 16.

Finally, the prediction method presented in this report must be considered as preliminary. Even though verification of the method by comparisons with experiment has demonstrated some success, there are configurations and flow conditions which must be

approached with caution. For this reason, several recommendations for improvements to the method are suggested in the following section.

RECOMMENDATIONS

In the course of development and verification of the code VTXCHN, several specific areas requiring additional work were identified. Since the additional effort was beyond the scope of the present investigation, they are noted below as recommendations for future work.

The first and most important recommendation is for a thorough testing and further verification of VTXCHN. The code should be applied to a variety of configurations and flow conditions for which experimental results are available for comparison purposes. This should better define the operational limits of the method. The major difficulty will be the lack of useful experimental results on appropriate forebody configurations.

The numerical difficulty associated with secondary separation discussed in a previous section needs further investigation. A minor modification may correct the problem, but some additional effort is required to understand the source of the problem.

The prediction method may have additional uses which have not been explored. For example, the code has vortex shedding technology built into it which can be transferred to three-dimensional panel codes. The code also has potential use in providing separation line and vortex wake information for starting solutions for higher order prediction methods.

Finally, the prediction method may have application in the investigation of other complex vortex phenomena such as asymmetry and vortex bursting.

ACKNOWLEDGEMENTS

The authors are grateful to Dr. Robert M. Hall and Dr. Michael J. Hemsch of the NASA/Langley Research Center for their constructive comments and able assistance throughout the course of this investigation.

REFERENCES

1. Mendenhall, M. R. and Lesieutre, D. J.: Prediction of Vortex Shedding From Circular and Noncircular Bodies in Subsonic Flow. NASA CR-4037, January 1987.

2. Mendenhall, M. R. and Perkins, S. C., Jr.: Vortex Cloud Model for Body Vortex Shedding and Tracking. Tactical Missile Aerodynamics, Vol. 104 of Progress in Astronautics and Aeronautics, ed. by M. J. Hemsch and J. N. Nielsen, AIAA, 1986.

3. Mendenhall, M. R. and Perkins, S. C., Jr.: Prediction of Vortex Shedding From Circular and Noncircular Bodies in Supersonic Flow. NASA CR-3754, January 1984.

4. Marshall, F. J. and Deffenbaugh, F. D.: Separated Flow Over Bodies of Revolution Using an Unsteady Discrete-Vorticity Cross Wake. NASA CR-2414, June 1974.

5. Sarpkaya, T.: Computational Methods With Vortices - The 1988 Freeman Scholar Lecture. ASME J. Fluids Engineering, March 1989, Vol. 111, pp. 5-52.

6. Oh, S., Tavella, D., and Roberts, L.: Theoretical Studies on Flapped Delta Wings. JIAA TR-85, Stanford University, August 1988.

7. Brown, C. E. and Michael, W. H., Jr.: On Slender Delta Wings with Leading-Edge Separation. NACA TN 3430, 1955.

8. Mangler, K. W. and Smith, J. H. B.: Calculation of the Flow Past Slender Delta Wings with Leading-Edge Separation. RAE Report No. Aero. 2593, May 1957.

9. Sacks, A. H., Lundberg, R. E., and Hanson, C. W.: A Theoretical Investigation of the Aerodynamics of Slender Wing-Body Combinations Exhibiting Leading-Edge Separation. NASA CR-719, March 1967.

10. Hoeijimakers, H. W. M. and Bennekers, B.: A Computational Model for the Calculation of the Flow about Wings with Leading-Edge Separation. AGARD CP-247, 1972.

11. Kandil, O. A.: Computational Technique for Compressible Vortex Flows Past Wings at Large Incidence. J. of Aircraft, Vol. 22, No. 9, pp. 750-755, 1985.

12. Mendenhall, M. R. and Nielsen, J. N.: Effect of Symmetrical Vortex Shedding on the Longitudinal Aerodynamic Characteristics of Wing-Body-Tail Combinations. NASA CR-2473, January 1975.

13. Nielsen, J. N.: Missile Aerodynamics. Nielsen Engineering & Research, Inc., 1988.

14. Skulsky, R. S.: A Conformal Mapping Method to Predict Low-Speed Aerodynamic Characteristics of Arbitrary Slender Re-Entry Shapes. J. of Spacecraft, Vol. 3, No. 2., February 1966, pp. 247-253.

15. Jeffreys, H. and Jeffreys, B.: Methods of Mathematical Physics. Cambridge University Press, 1966, pp. 424-426.

16. Lesieutre, D. J., Mendenhall, M. R., and Torres, T. O.: Missile Stability and Methods Development, Vol. III - Programs SUBVTX and SUPVTX for Determining Aerodynamic Characteristics of Arbitrary Missile Bodies Including Separation Vorticity. NEAR TR 396, August 1989.

17. Wolfe, W. P. and Oberkampf, W. L.: A Design Method for the Flow Field and Drag of Bodies of Revolution in Incompressible Flow. AIAA Paper 82-1359, August 1982.

18. Janikowsky, L. C. and Sarpkaya, T.: Optimized Discrete-Singularity Representation of Axisymmetric Bodies. AIAA Paper 85-0284, January 1985.

19. Christopher, P. A. T.: The Generation of Axi-Symmetric Bodies in Incompressible Flow by Means of Distributions of Complex Sources. Cranfield Report CoA 8304, March 1983.

20. Goodwin, F. K., Nielsen, J. N., and Dillenius, M. F. E.: A Method for Predicting Three-Degree-of-Freedom Store Separation Trajectories at Speeds up to the Critical Speed. AFFDL-TR-71-81, July 1971.

21. Hemsch, M. J.: An Improved, Robust, Axial Line Singularity Method for Bodies of Revolution. AIAA 89-2176, July 1989.

22. Hemsch, M. J.: Comparison of High Angle-of-Attack Slender-Body Theory and Exact Solutions for Potential Flow Over an Ellipsoid, Journal of Aircraft, August 1990.

23. Shapiro, A. H.: The Dynamics and Thermodynamics of Compressible Fluid Flow. The Ronald Press Co., New York, 1953.

24. Milne-Thomson, L. M.: Theoretical Aerodynamics. The Macmillan Co., New York, 1960.

25. Ashley, H. and Landhal, M.: Aerodynamics of Wings and Bodies. Addison-Wesley Pub. Co., Inc., 1965.

26. Cebeci, T., Mosinskis, G. J., and Smith, A. M. O.: Calculation of Viscous Drag and Turbulent Boundary-Layer Separation on Two-Dimensional and Axisymmetric Bodies in Incompressible Flow. McDonnell Douglas Rept. MDC JO 973-01 (Contract N00014-70-C-0099), November 1970.

27. Stratford, B. S.: The Prediction of Separation of the Turbulent Boundary Layer. J. of Fluid Mech., Vol. 5, 1959, pp. 1-16.

28. Giesing, J. P.: Vorticity and Kutta Condition for Unsteady Multienergy Flows. ASME J. Applied Mech., September 1969, pp. 608-613.

29. Mostafa, S. I. M.: Numerical Simulation of Unsteady Separated Flows. Ph.D. Thesis, Naval Postgraduate School, Monterey, CA, June 1987.

30. Tinling, B. E. and Allen, C.Q.: An Investigation of the Normal-Force and Vortex-Wake Characteristics of an Ogive-Cylinder Body at Subsonic Speeds, NASA TN D-1297, April 1962.

31. Schindel, L. H. and Chamberlain, T. E.: Vortex Separation on Slender Bodies of Elliptic Cross Section. MIT Aerophysics Laboratory Technical Report 138, August 1967.

32. Erickson, G. E. and Brandon, J. M.: Low-Speed Experimental Study of the Vortex Flow Effects of a Fighter Forebody Having Unconventional Cross-Section. AIAA 85-1798, August 1985.

33. Lamont, P. J.: Pressure Measurments on an Ogive-Cylinder at High Angles of Attack with Laminar, Transitional, or Turbulent Separation. AIAA 80-1556, August 1980.

Nielsen Engineering & Research, Inc.
Mountain View, CA 94043-2287
December 1989

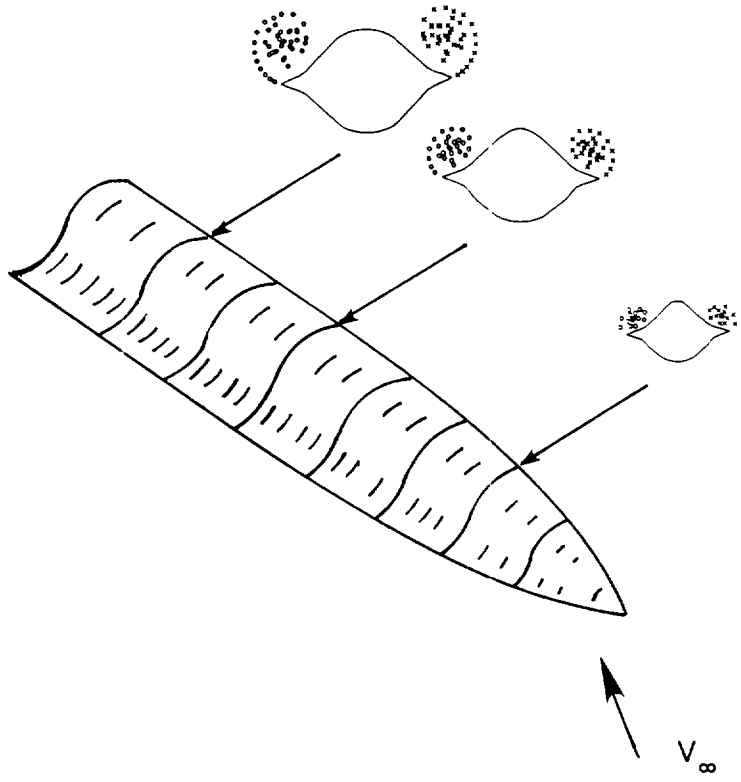

Figure 1.- Lee side vortex formation on a forebody with chine.

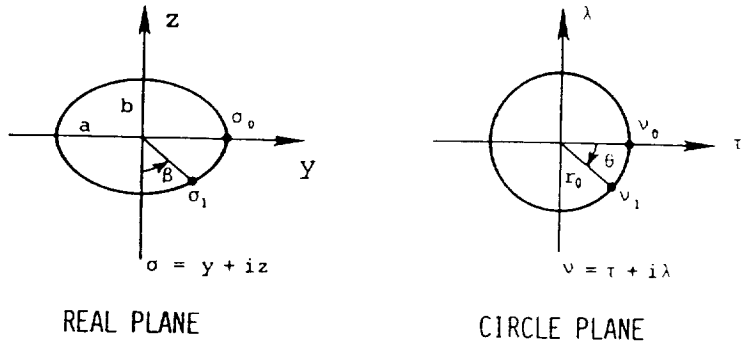

(a) Analytical transformation procedure

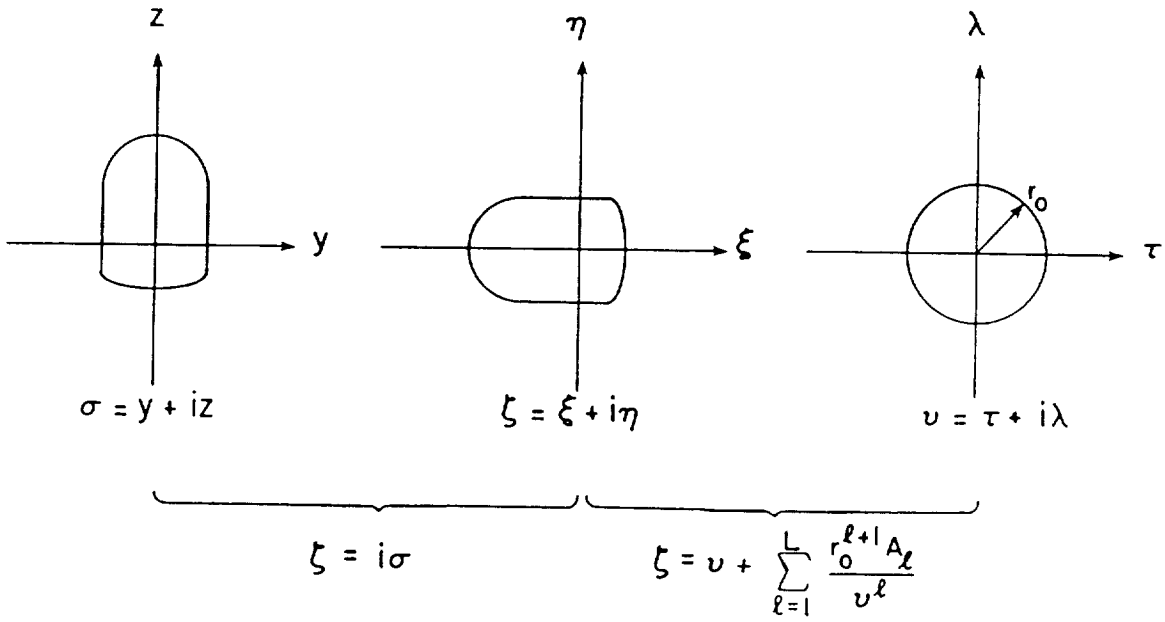

(b) Numerical transformation procedure

Figure 2.- Conformal mapping nomenclature.

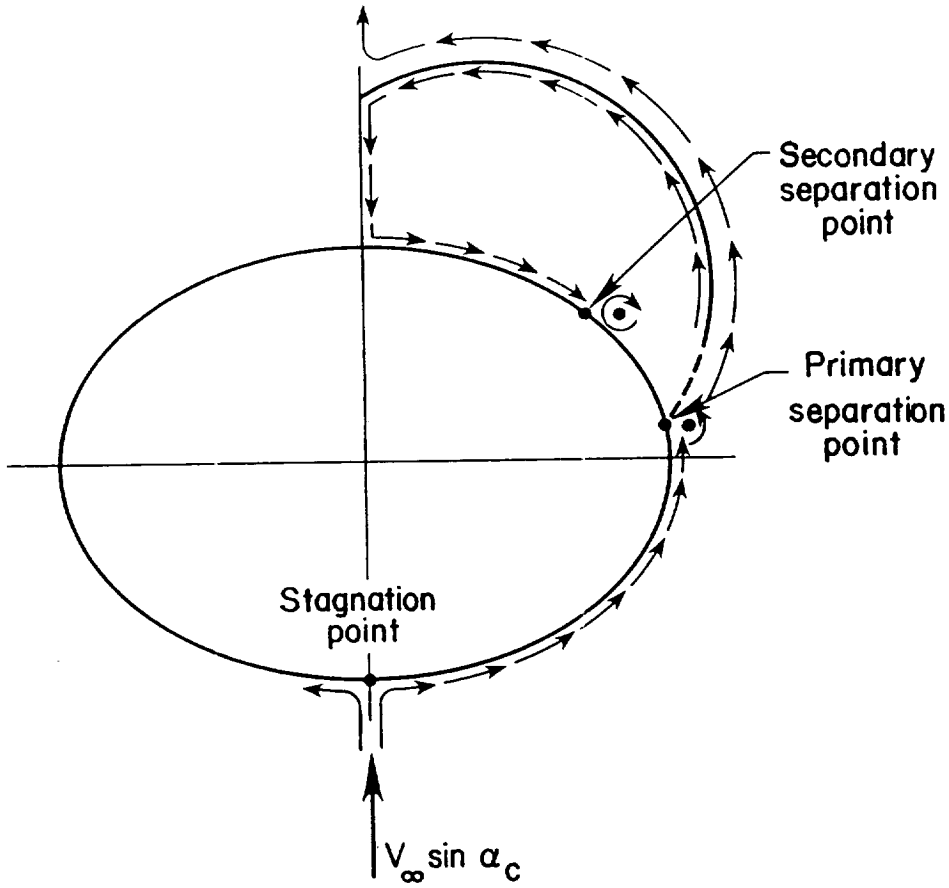

Figure 3. - Sketch of crossflow plane separation points.

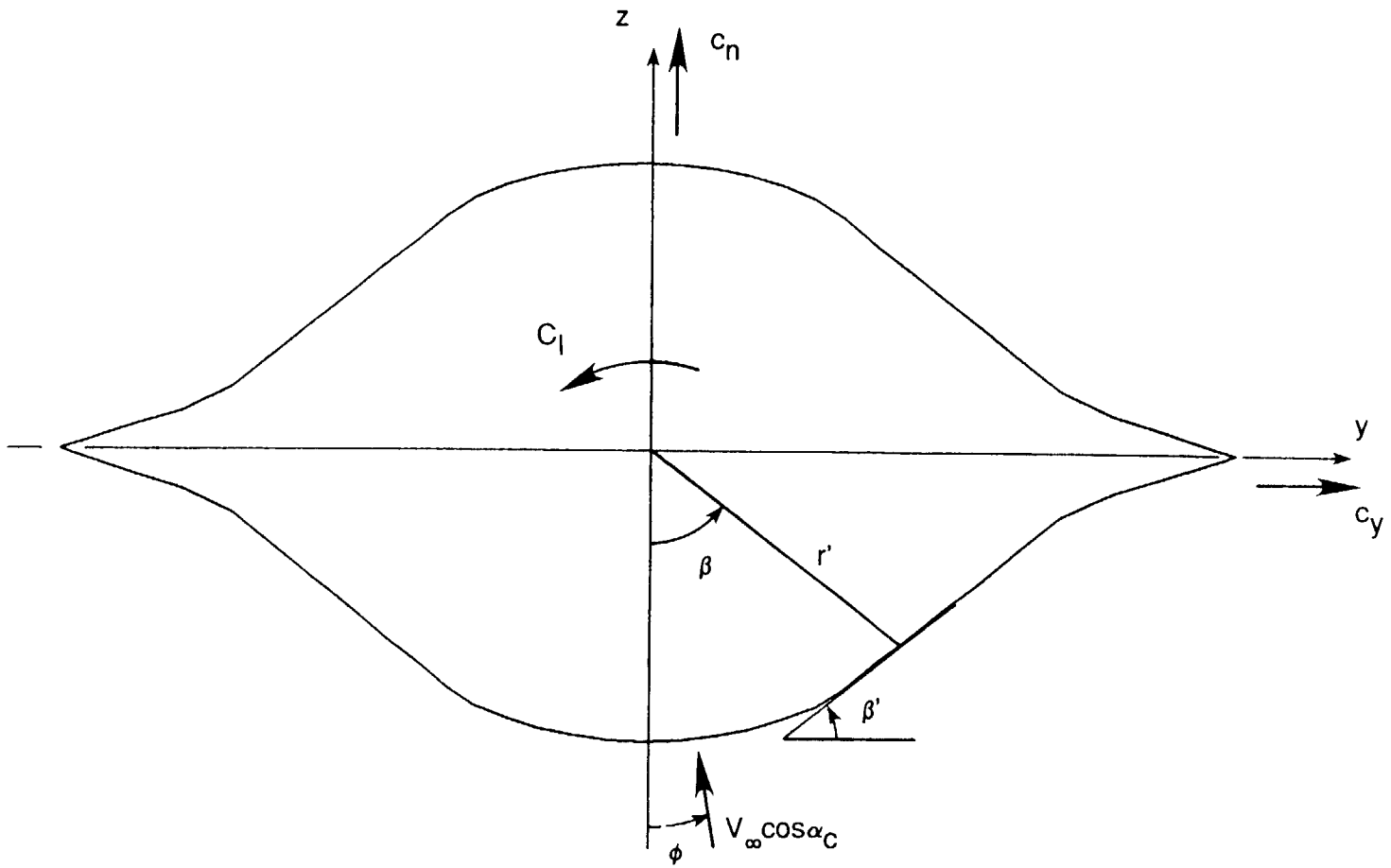

Figure 4- Forebody cross section nomenclature.

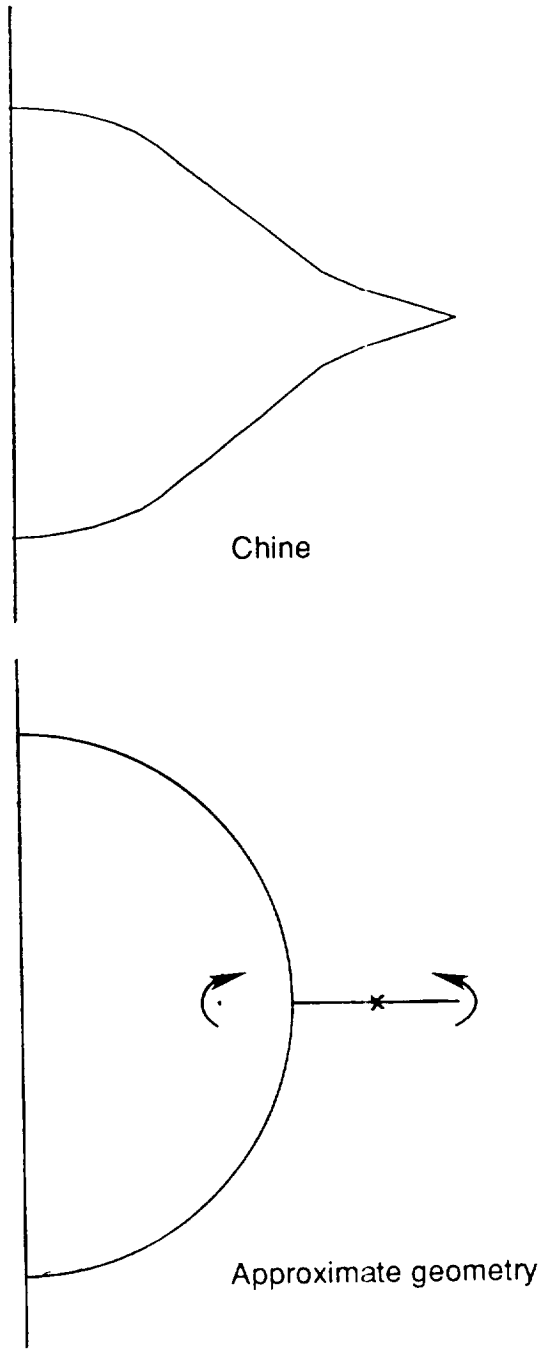

Figure 5.- Panel approximation for calculating initial vortex strength.

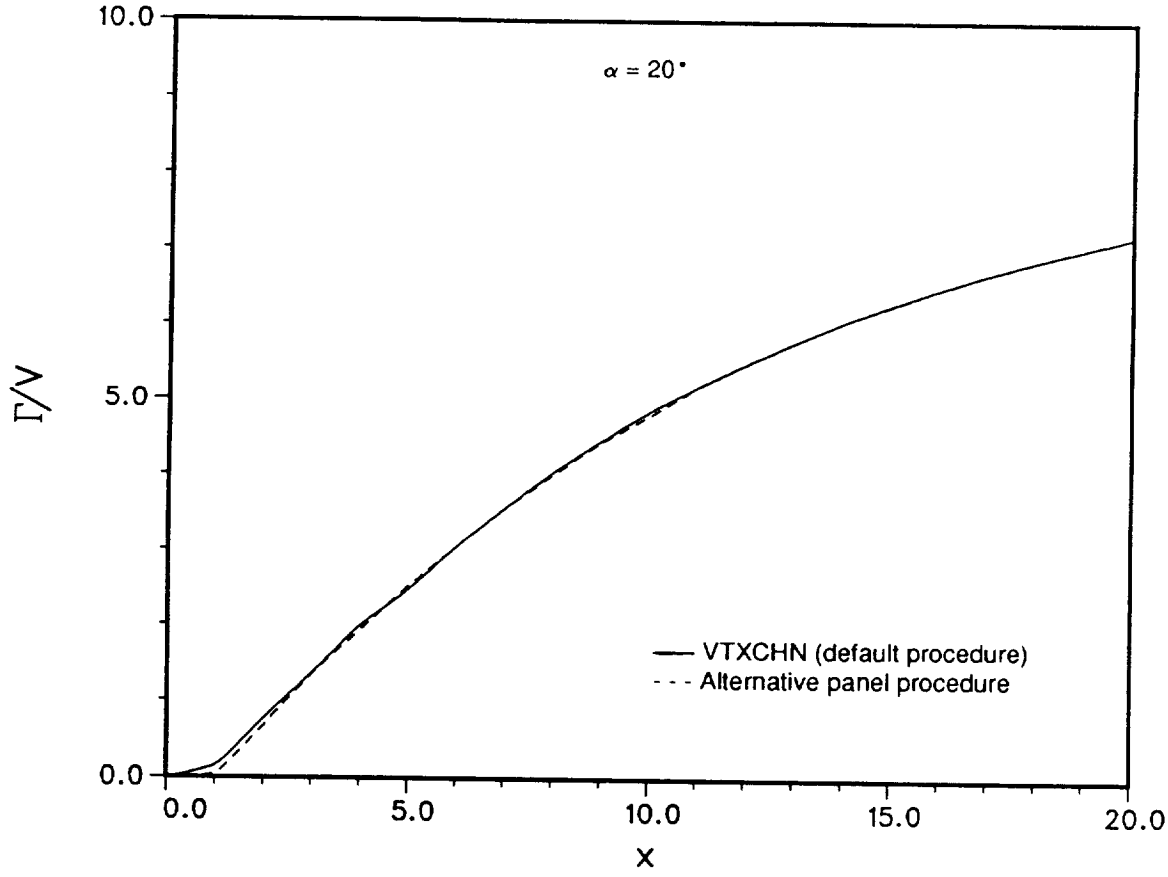

Figure 6.- Effect of solution starting procedure on vortex development.

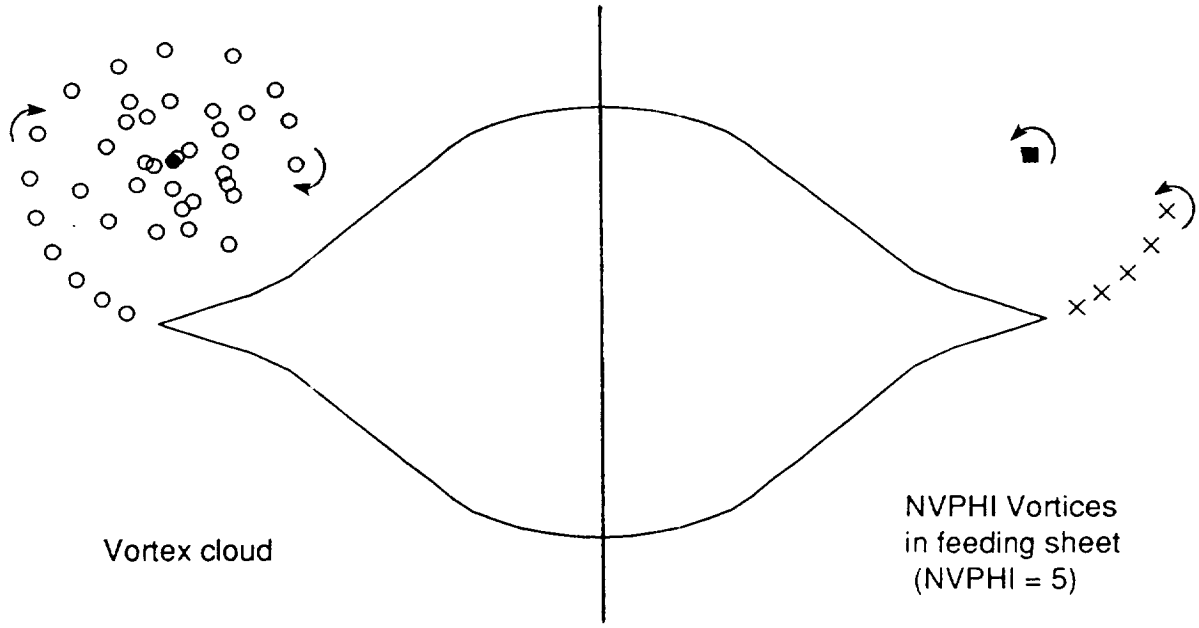

Figure 7.- Vortex cloud modification for $d\phi/dt$ calculation.

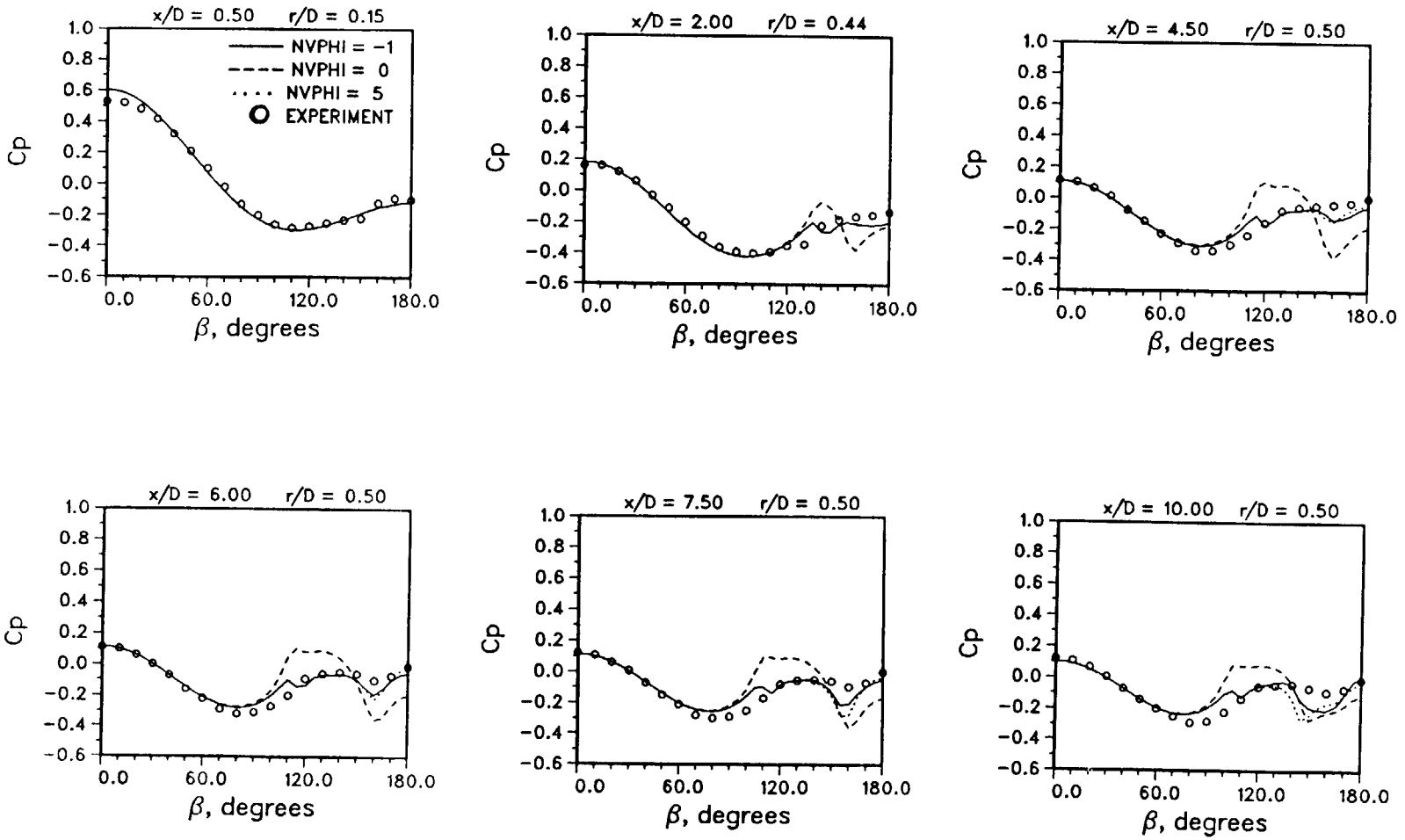

Figure 8.- Effect of vortex cloud modification on predicted pressure distributions on an ogive cylinder, $\alpha = 20°$.

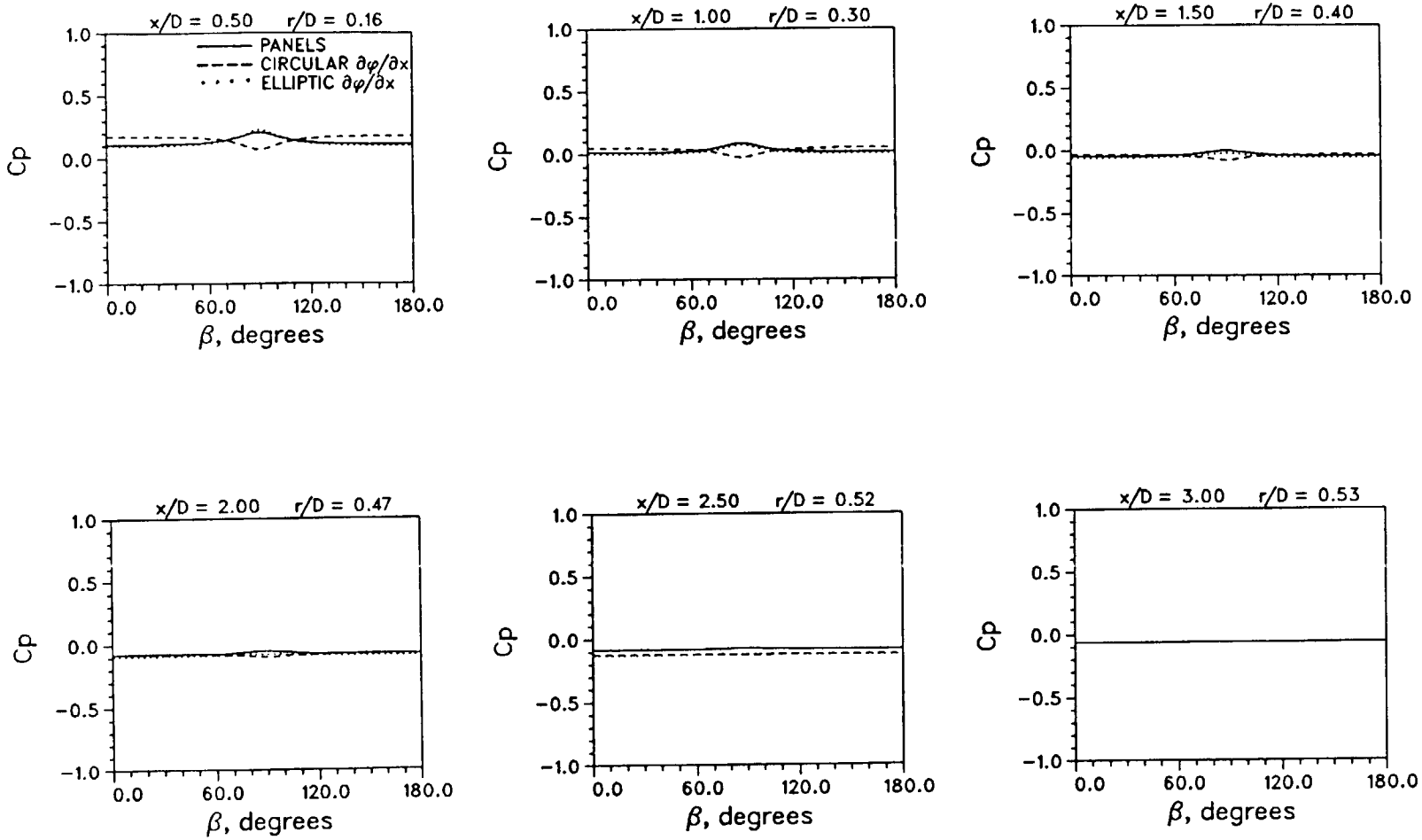

(a) $\alpha = 0°$

Figure 9.- Effect of noncircular u-velocity approximation on predicted pressure distribution on a 2:1 elliptic cross section forebody.

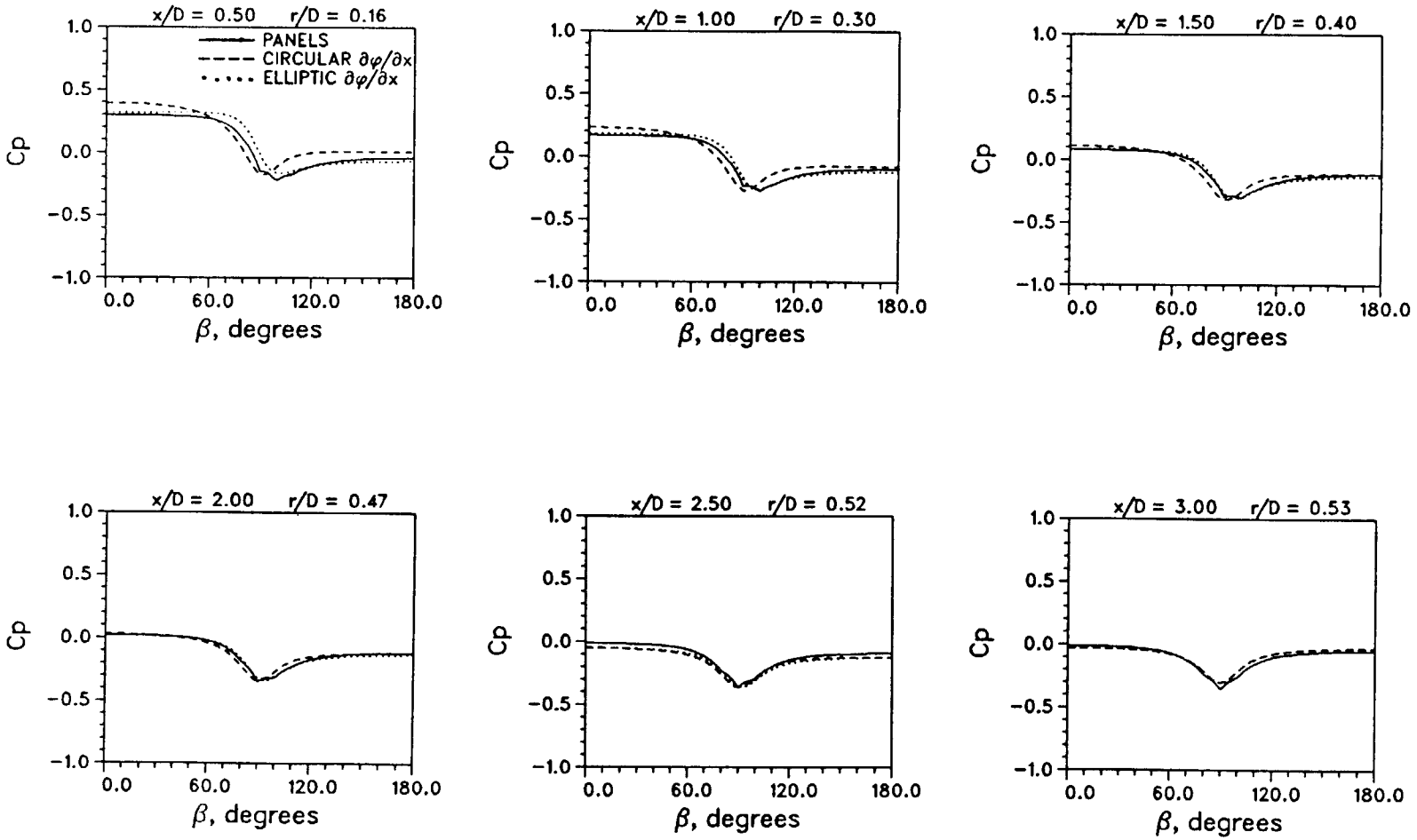

(b) $\alpha = 10°$

Figure 9.- Concluded.

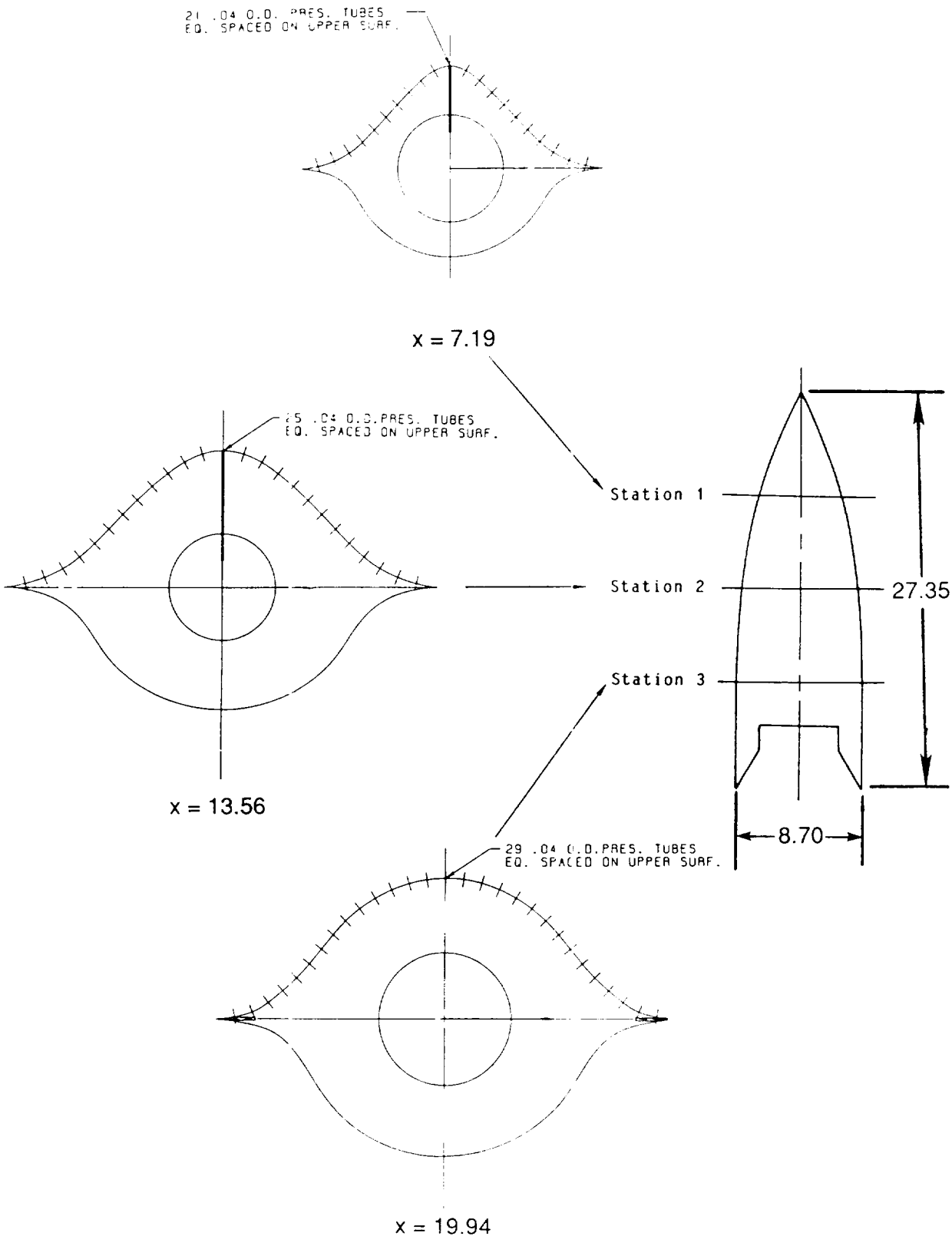

Figure 10.- Forebody with chine details (from Ref. 30).

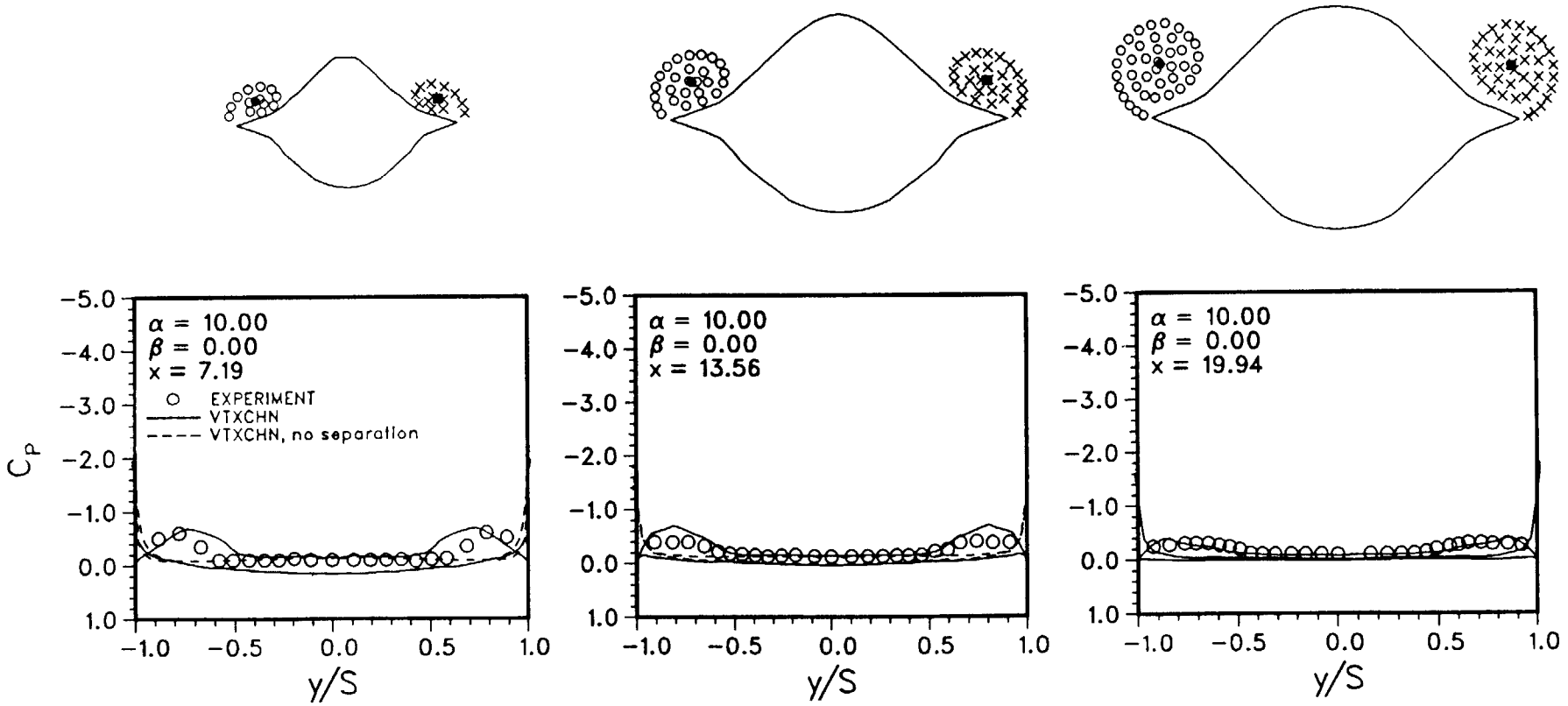

(a) x = 7.19 (b) x = 13.56 (c) x = 19.94

Figure 11.- Measured and predicted pressure distributions on a forebody with chine, $\alpha = 10°$.

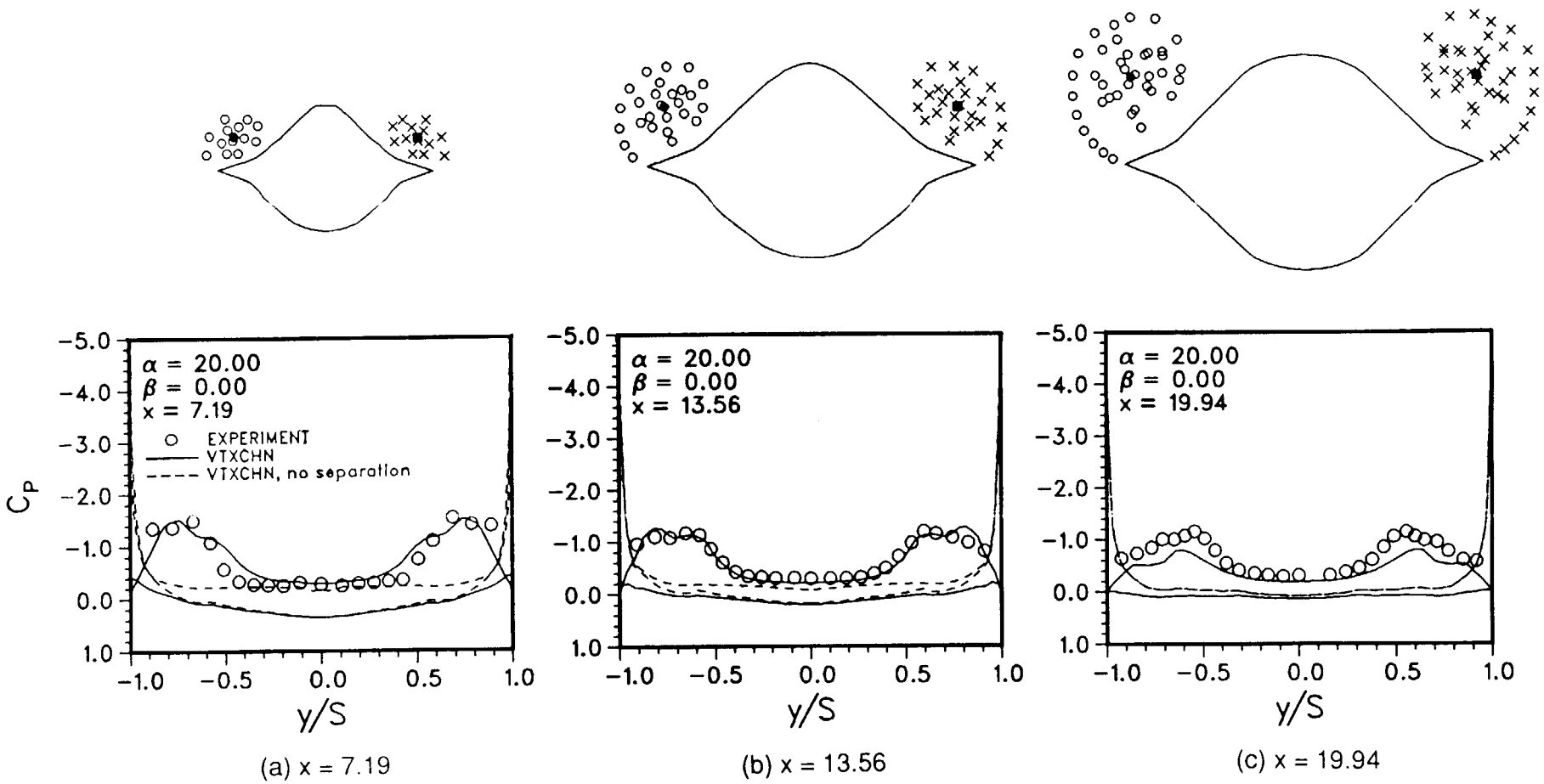

Figure 12.- Measured and predicted pressure distributions on a forebody with chine, $\alpha = 20°$.

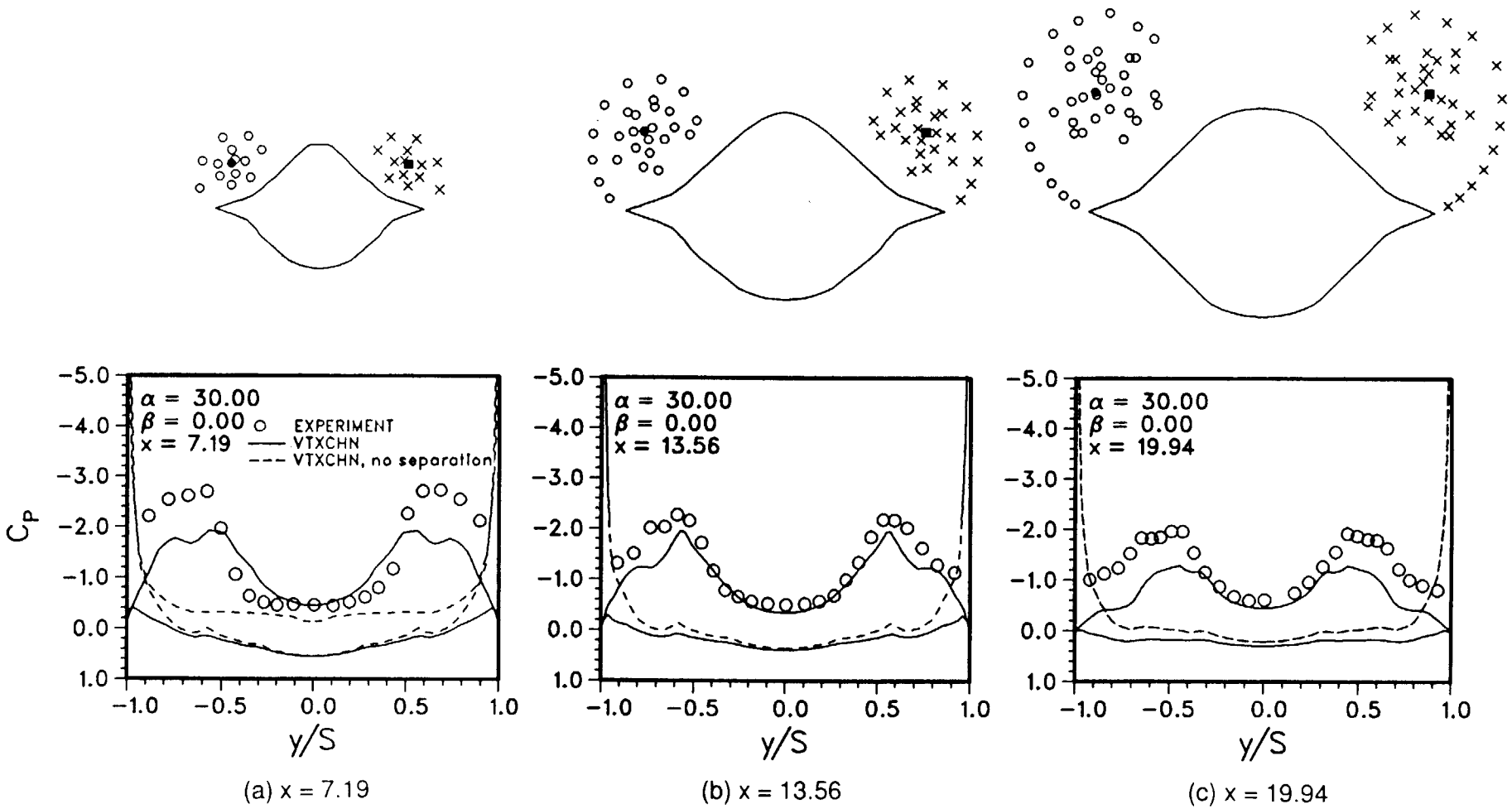

Figure 13.- Measured and predicted pressure distributions on a forebody with chine, $\alpha = 30°$.

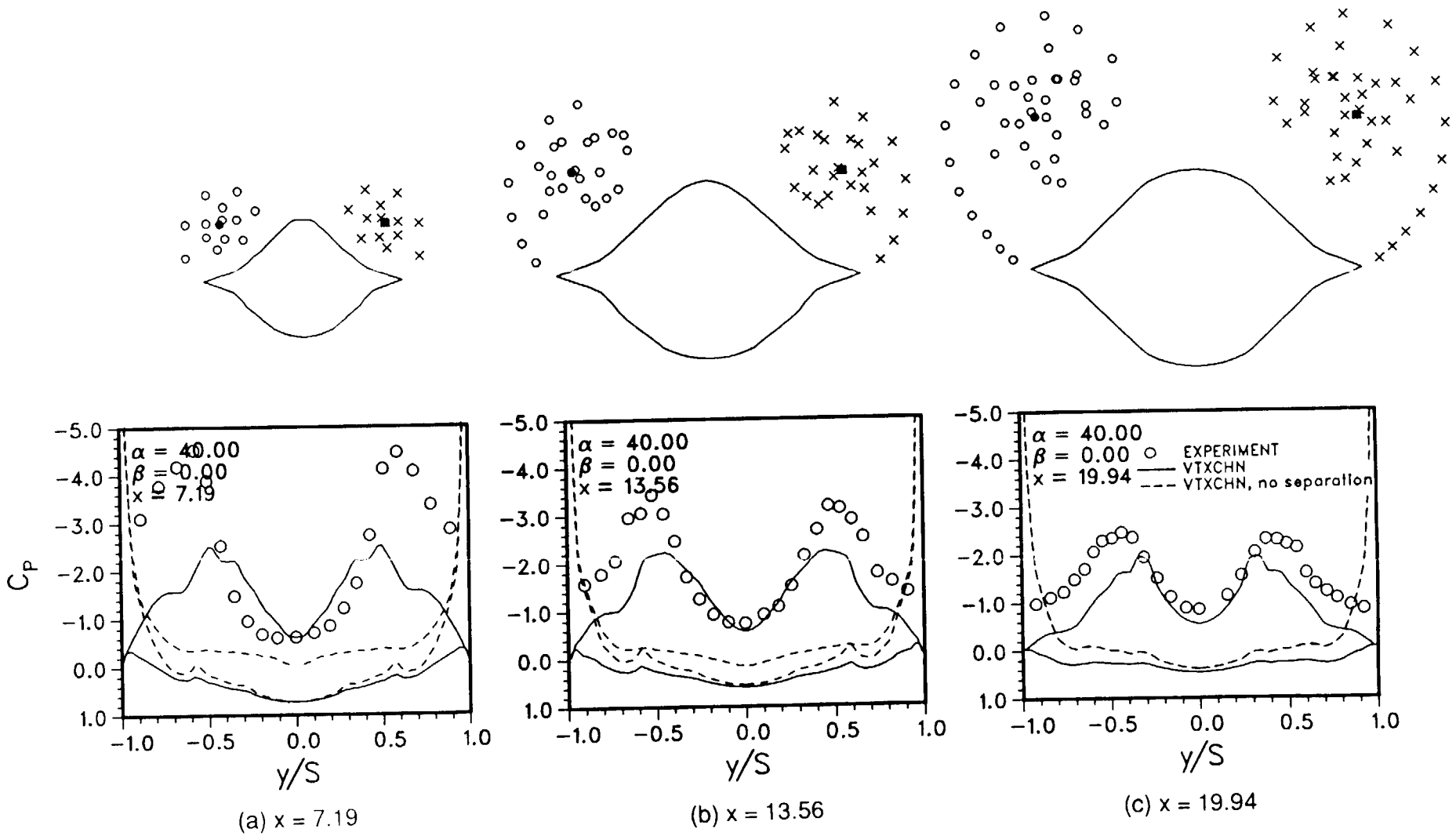

Figure 14.- Measured and predicted pressure distributions on a forebody with chine, $\alpha = 40°$.

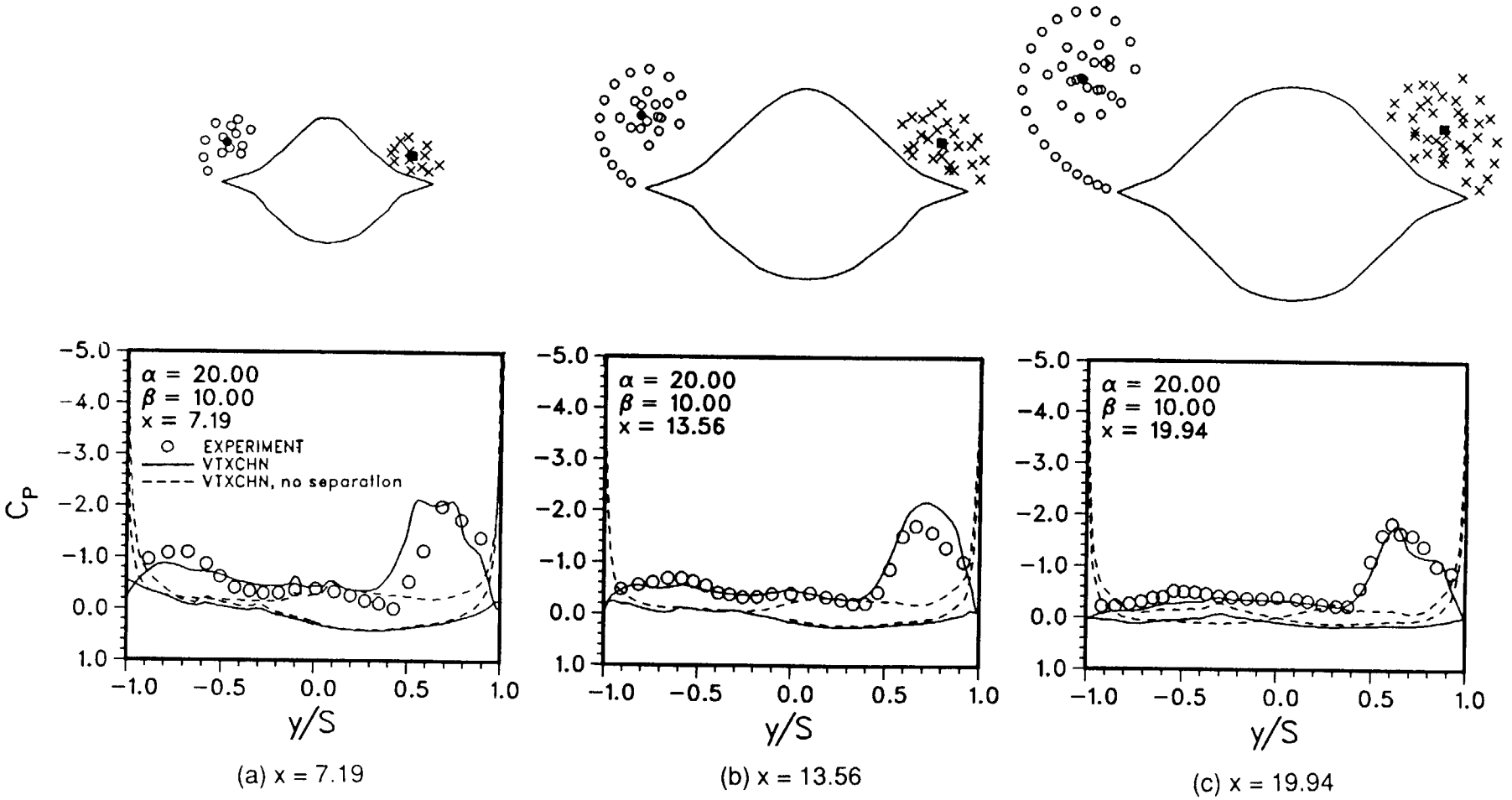

Figure 15.- Measured and predicted pressure distributions on a forebody with chine, $\alpha = 20°$, $\beta = 10°$.

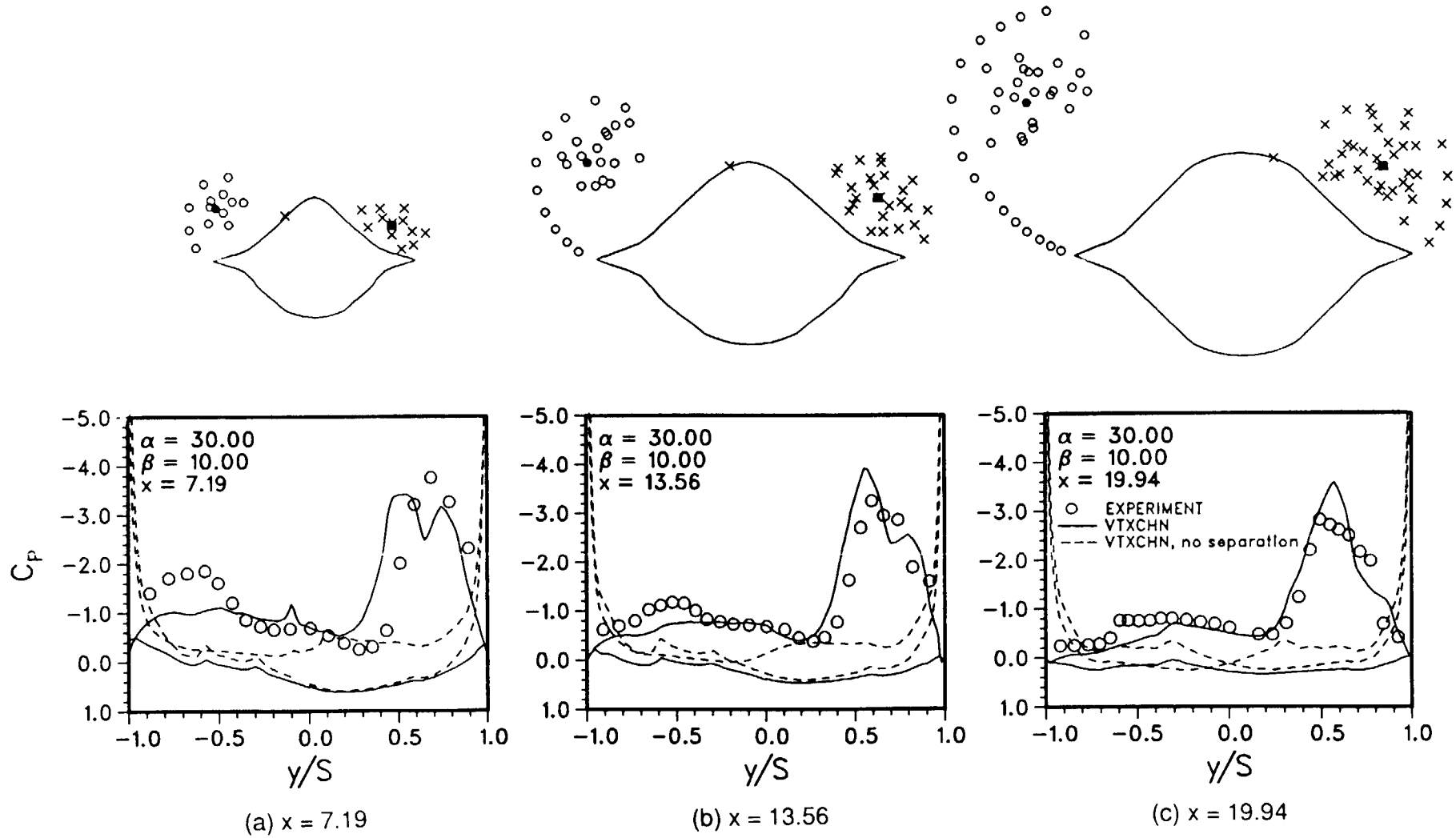

(a) x = 7.19 (b) x = 13.56 (c) x = 19.94

Figure 16.- Measured and predicted pressure distributions on a forebody with chine, $\alpha = 30°$, $\beta = 10°$.

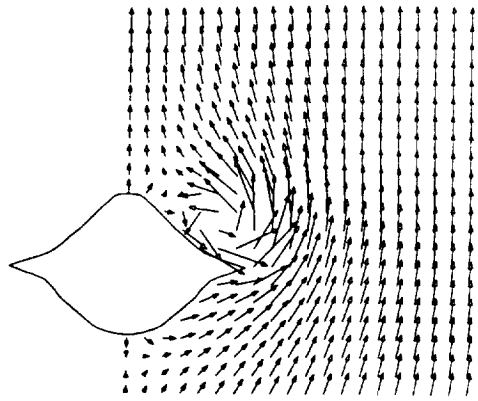

(a) x = 7.19

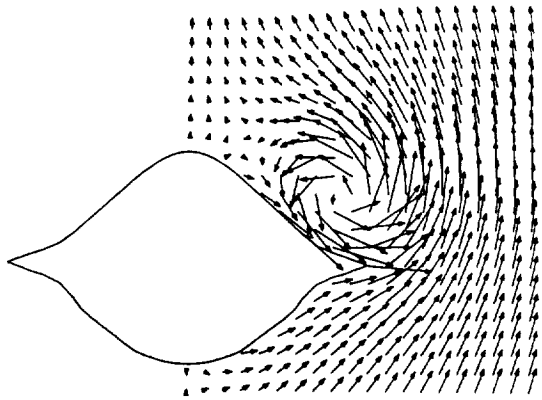

(b) x = 13.56

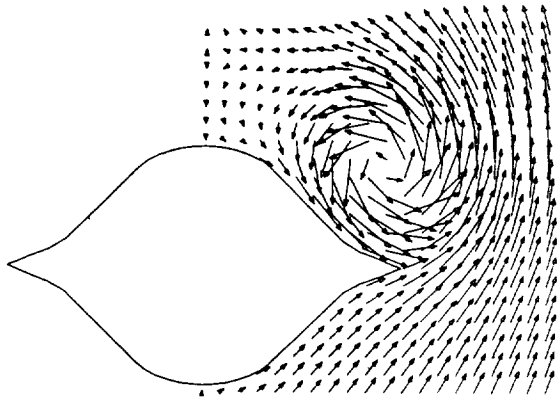

(c) x = 19.94

Figure 17.- Predicted velocity vectors near a forebody with chine, $\alpha = 20°$

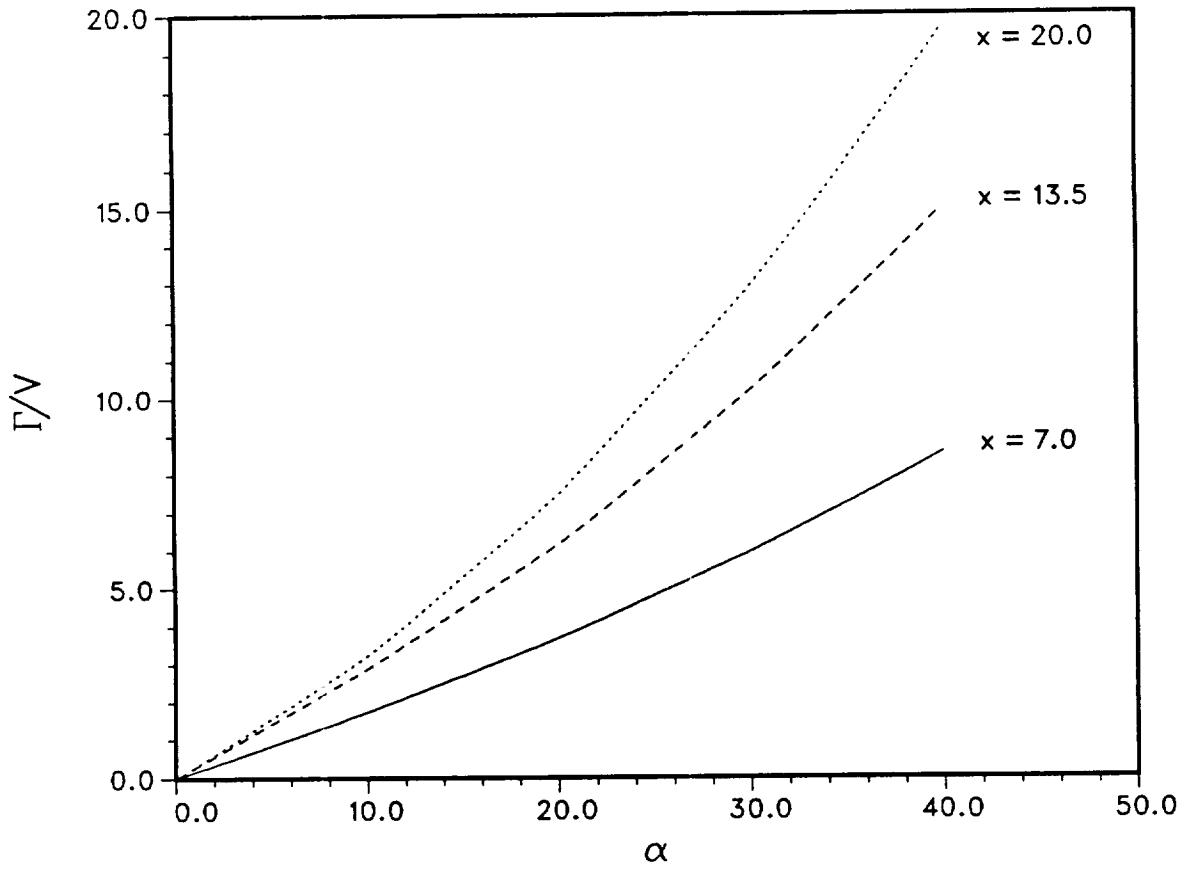

Figure 18.- Predicted vortex strength near a forebody with chine.

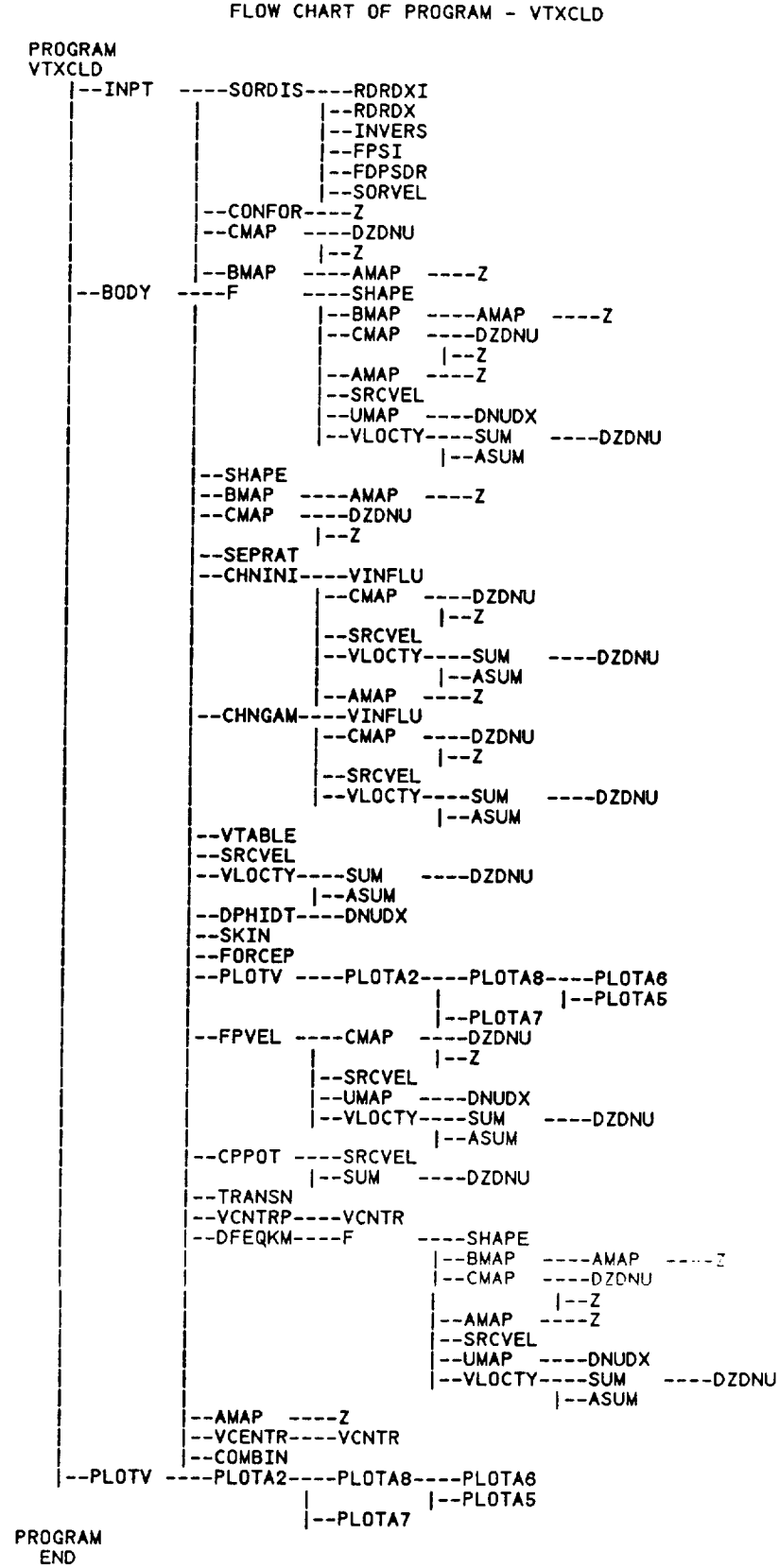

Figure 19.- Subroutine calling sequence for program VTXCHN.

CROSS REFERENCE MAP PAGE = 1

SUBROUTINE NAME / EXTERNAL REFERENCES	AMAP	ASUM	BMAP	BODY	CHNGAM	CHNINI	CMAP	COMBIN	CONFOR	CPPOT	DFEQKM	DNUDX	DPHIDT	DZDNU	F	FDPSDR	FORCEP	FPSI	FPVEL	INPT	INVERS	PLOTA2	PLOTA5	PLOTA6	PLOTA7	PLOTA8	PLOTV	RDRDX	RDRDXI	SEPRAT	SHAPE	SKIN	SORDIS	SORVEL	SRCVEL	SUM	TRANSN	UMAP	VCENTR	VCNTR
AMAP			X	X		X									X																								
ASUM																																							
BMAP				X											X					X																			
BODY																																							
CHNGAM				X																																			
CHNINI				X																																			
CMAP				X	X	X									X					X	X																		
COMBIN				X																																			
CONFOR																				X																			
CPPOT				X																																			
DFEQKM				X																																			
DNUDX													X																								X			
DPHIDT				X																																			
DZDNU							X																														X			
F				X							X																													
FDPSDR																																X							
FORCEP				X																													X						
FPSI																																							
FPVEL				X																																			
INPT																																							
INVERS																																	X						
PLOTA2																						X																	
PLOTA5																						X																	
PLOTA6																						X																	
PLOTA7																									X														
PLOTA8																									X														
PLOTV				X																																			
RDRDX																																	X						
RDRDXI																																	X						
SEPRAT				X																																			

(a) Page 1

Figure 20.- Subroutine cross reference list for program VTXCHN.

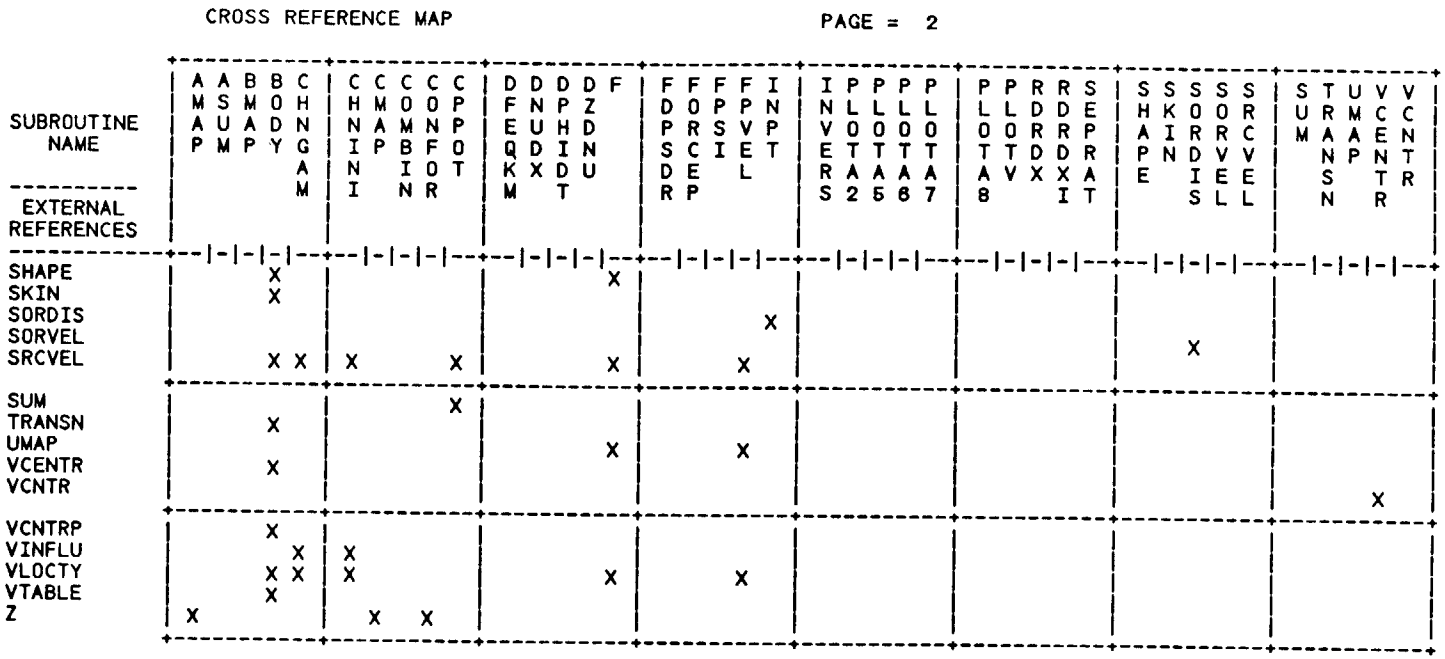

(b) Page 2

Figure 20.- Continued.

CROSS REFERENCE MAP

SUBROUTINE NAME	VCNTRP	VINFLU	VLOCTY	VTABLE	Z
EXTERNAL REFERENCES					
AMAP					
ASUM		X			
BMAP					
BODY				X	
CHNGAM					
CHNINI					
CMAP					
COMBIN					
CONFOR					
CPPOT					
DFEQKM					
DNUDX					
DPHIDT					
DZDNU					
F					
FDPSDR					
FORCEP					
FPSI					
FPVEL					
INPT				X	
INVERS					
PLOTA2					
PLOTA5					
PLOTA6					
PLOTA7					
PLOTA8					
PLOTV				X	
RDRDX					
RDRDXI					
SEPRAT					

CROSS REFERENCE MAP

SUBROUTINE NAME	VCNTRP	VINFLU	VLOCTY	VTABLE	Z
EXTERNAL REFERENCES					
SHAPE					
SKIN					
SORDIS					
SORVEL					
SRCVEL					
SUM		X			
TRANSN					
UMAP					
VCENTR					
VCNTR	X				
VCNTRP					
VINFLU					
VLOCTY					
VTABLE					
Z					

(c) Page 3

Figure 20.- Concluded.

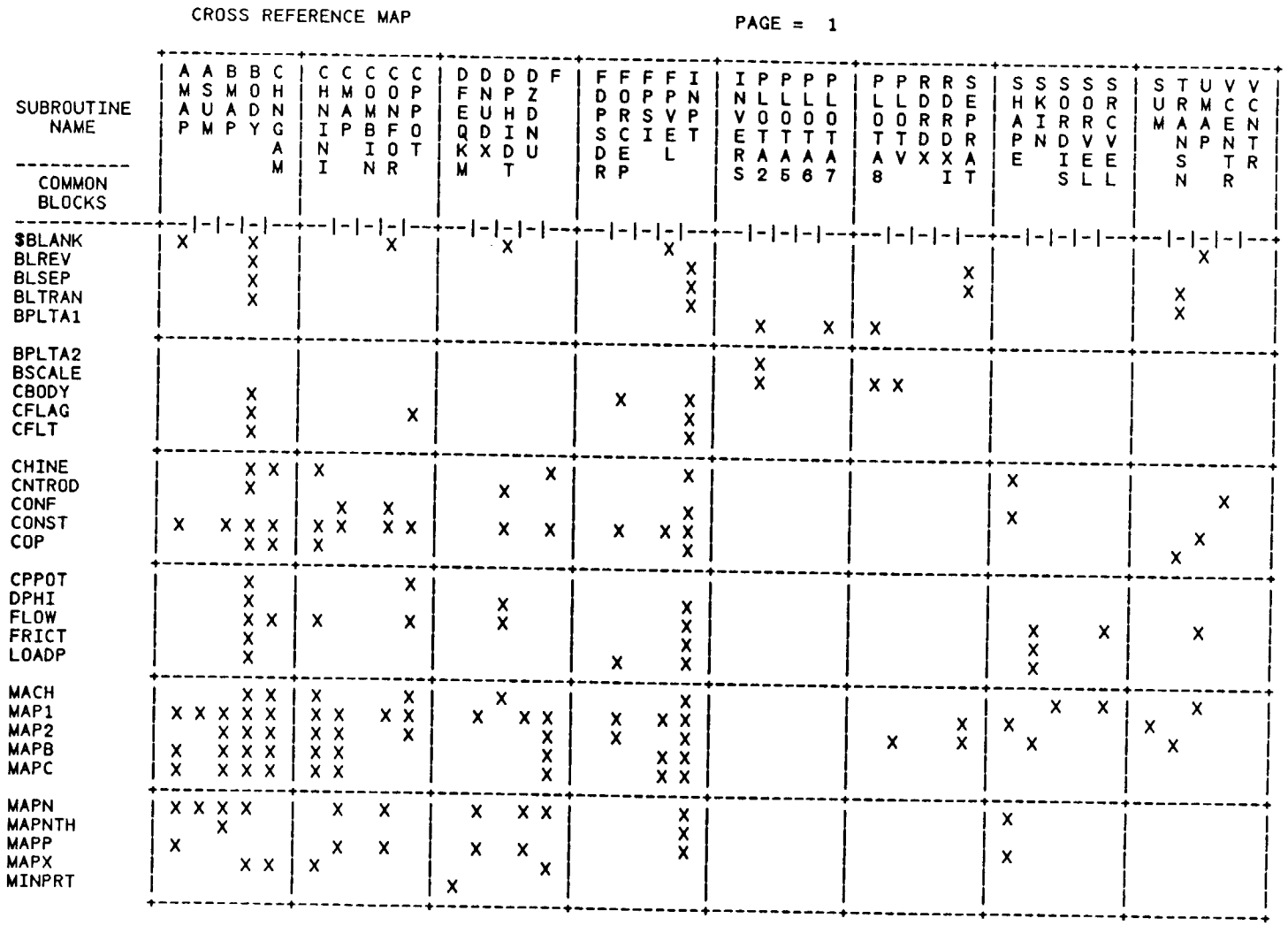

(a) Page 1

Figure 21.- Common block cross reference list for program VTXCHN.

CROSS REFERENCE MAP PAGE = 2

SUBROUTINE NAME / COMMON BLOCKS	AMAP	ASUM	BMAP	BODY	CHNGAM	CHNINI	CMAP	COMBIN	CONFOR	CPPOT	DFEQKM	DNUDX	DPHIDT	DZDNU	F	FDPSDR	FORCEP	FPSI	FPVEL	INPUT	INVERS	PLOTA2	PLOTA5	PLOTA6	PLOTA7	PLOTA8	PLOTV	RDRDX	RDRDXI	SEPRAT	SHAPE	SKIN	SORDIS	SORVEL	SRCVEL	SUM	TRANSN	UMAP	VCENTR	VCNTR
PHI				X	X	X				X			X		X				X																		X		
PRESS				X	X	X											X													X						X			
PRINTF																															X								
PROLD																	X			X																			
RATIO																	X			X											X								
RDRDXC																												X	X			X							
RE				X	X	X														X											X								
REF				X	X	X											X			X						X			X		X								
RZZZ																				X										X									
SHPE				X													X			X							X	X		X	X	X							
SOURCE				X												X		X		X												X	X	X					
SYMTRY				X	X	X				X				X						X									X										
TMPCS				X										X						X																			
VCORE																				X																			
VEL				X	X	X				X			X	X					X	X																			
VFPTS				X															X	X																			
VORTEX				X	X	X		X					X	X						X						X													
VTXTBL				X	X	X		X					X							X						X												X	
ZFLOW																				X									X										

(b) Page 2

Figure 21.- Continued.

CROSS REFERENCE MAP

SUBROUTINE NAME / COMMON BLOCKS	VCNTRP	VINFLU	VLOCTY	VTABLE	VTXCLD	Z
$BLANK			X			
BLREV						
BLSEP						
BLTRAN						
BPLTA1						
BPLTA2						
BSCALE						
CBODY						
CFLAG					X	
CFLT						
CHINE						
CNTROD						
CONF						
CONST			X		X	
COP					X	
CPPOT						
DPHI						
FLOW			X		X	
FRICT					X	
LOADP					X	
MACH			X			
MAP1			X		X	X
MAP2					X	
MAPB						
MAPC						
MAPN						X
MAPNTH						
MAPP						X
MAPX						
MINPRT						

CROSS REFERENCE MAP

SUBROUTINE NAME / COMMON BLOCKS	VCNTRP	VINFLU	VLOCTY	VTABLE	VTXCLD	Z
PHI			X			
PRESS					X	
PRINTF						
PROLD						
RATIO						
RDRDXC						
RE						
REF			X			
RZZZ						
SHPE						
SOURCE						
SYMTRY	X				X	
TMPCS			X			
VCORE			X			
VEL			X			
VFPTS						
VORTEX			X	X	X	
VTXTBL	X			X	X	
ZFLOW						

(c) Page 3

Figure 21.- Concluded.

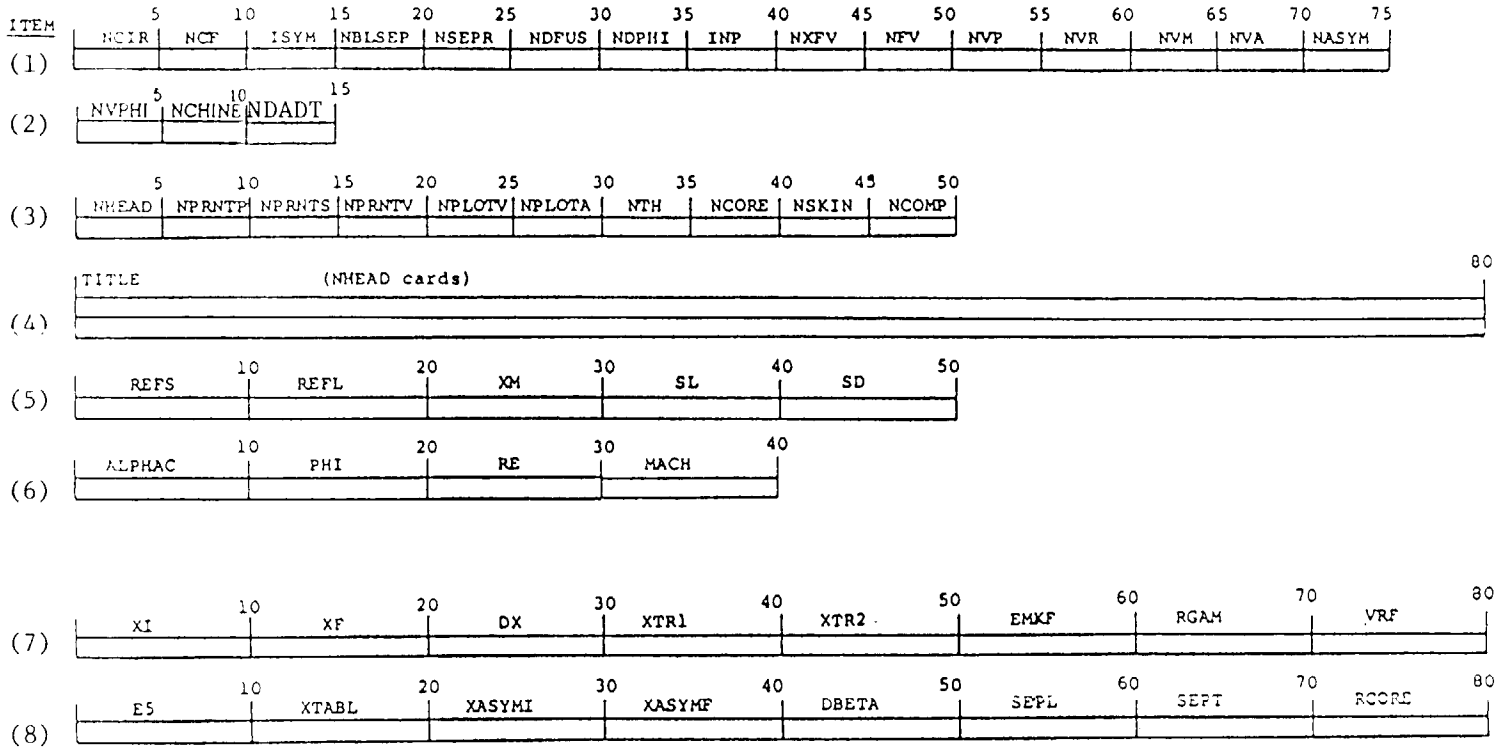

(a) Page 1

Figure 22.- Input forms for program VTXCHN.

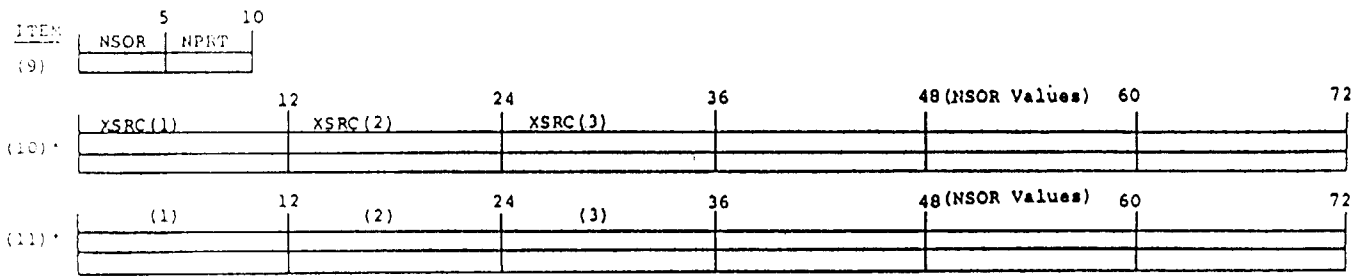

(b) Page 2

Figure 22.- Continued.

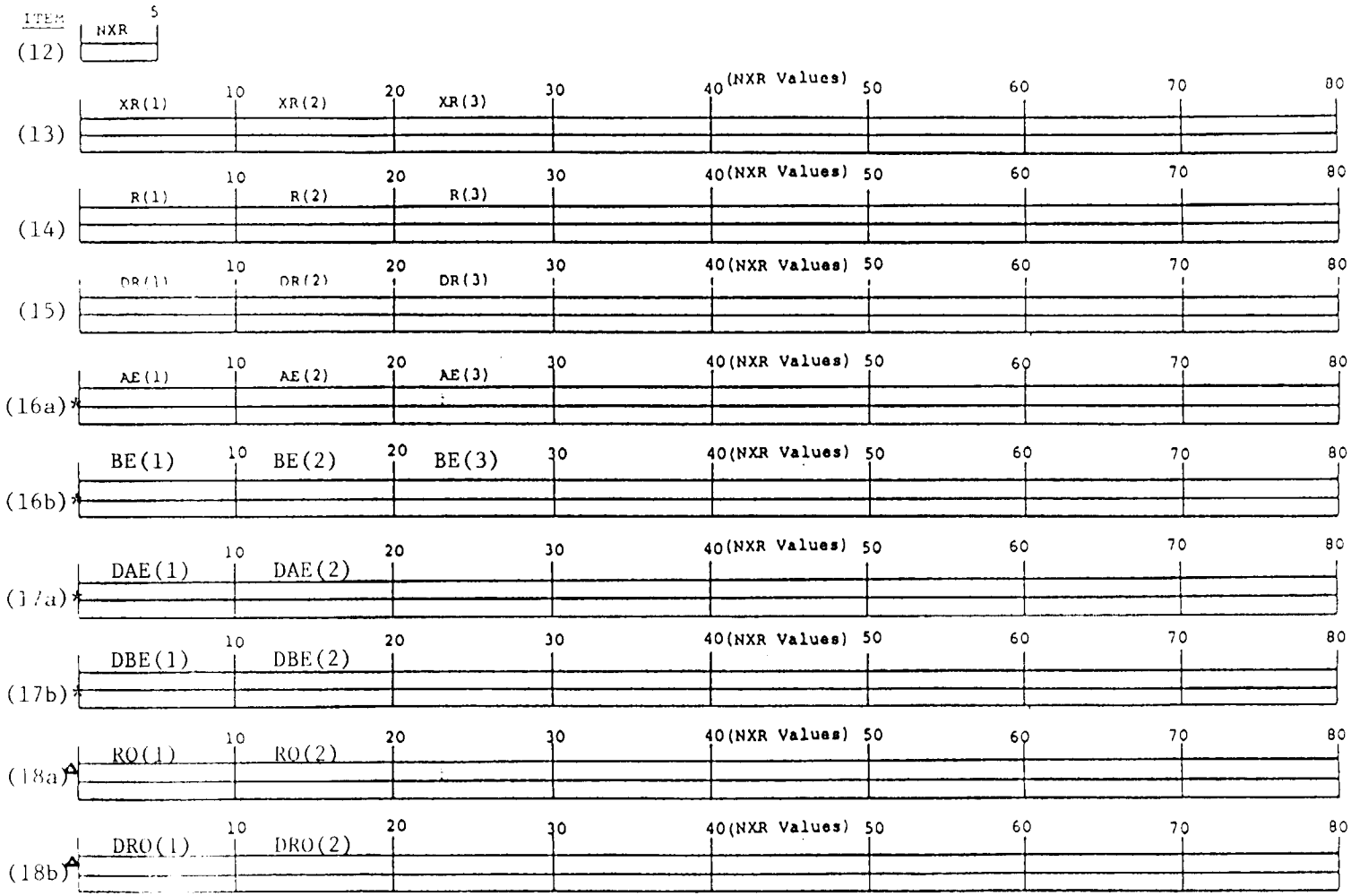

(c) Page 3

Figure 22.- Continued.

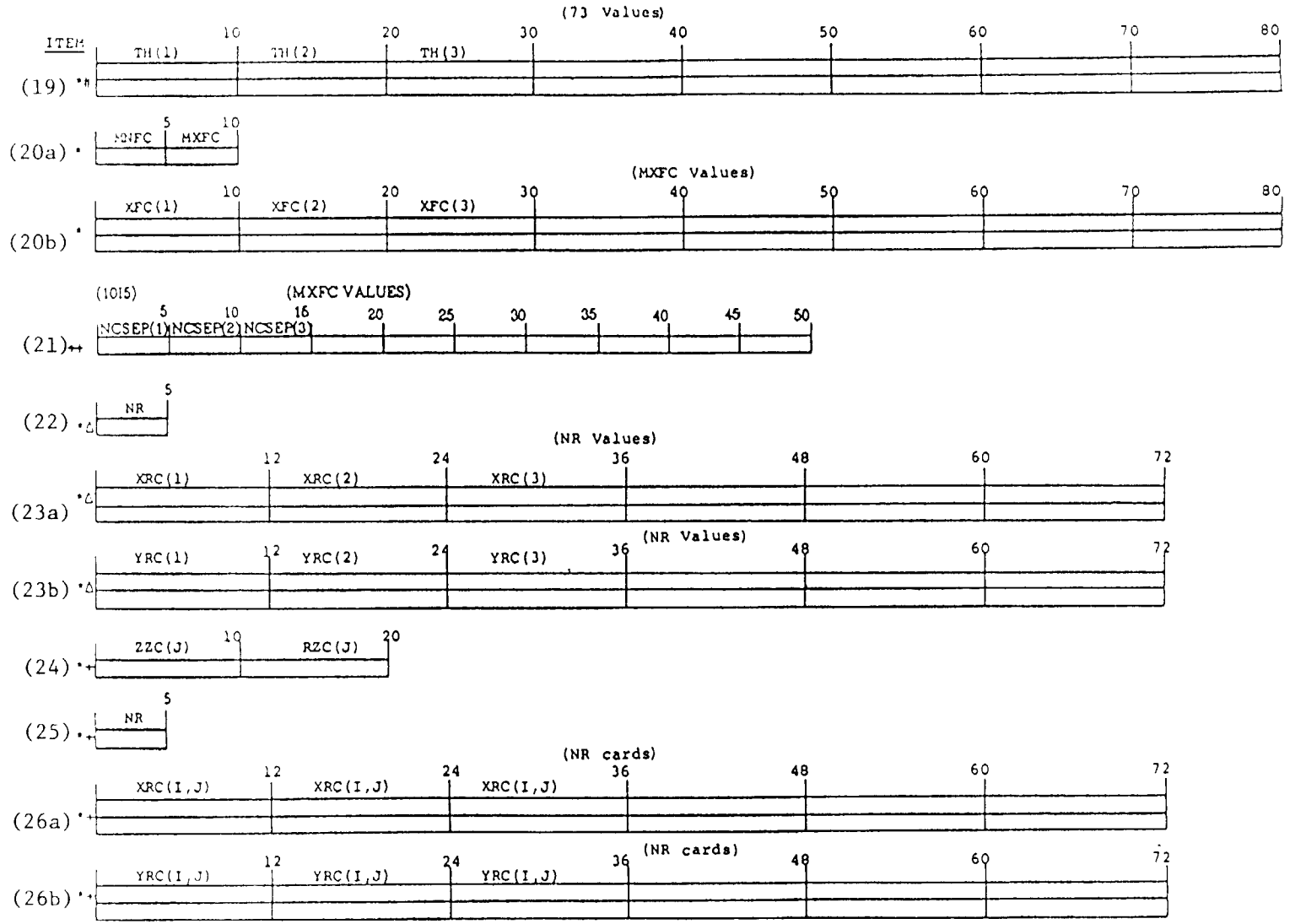

Omit items (19) through (27) if NCIR < 2
Omit items (22) through (23) if NCF ≠ 0
Omit items (24) through (27) if NCF = 0
Omit item (19) if NTH = 0
Omit item (21)a if NCHINE = 0

(d) Page 4

Figure 22.- Continued.

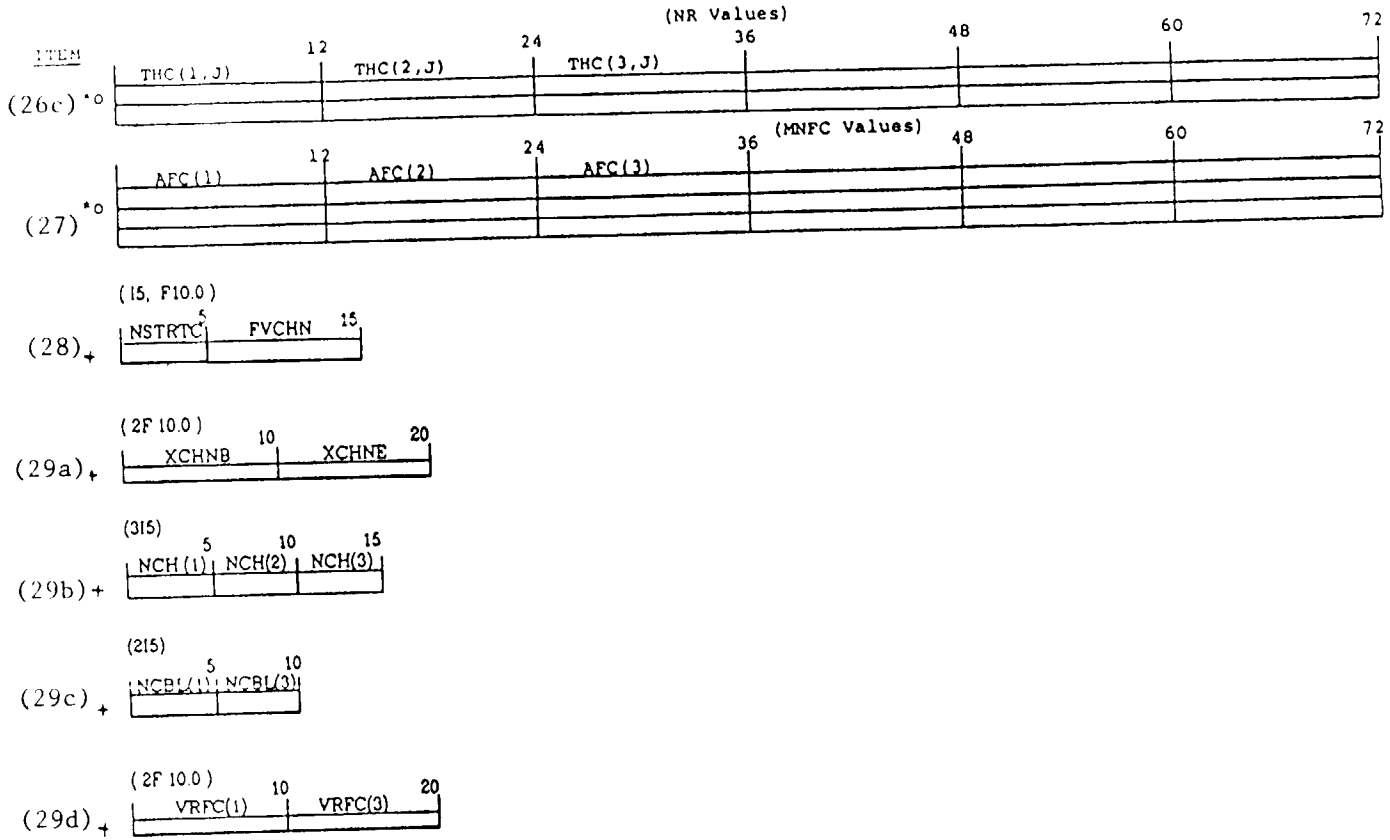

* Omit items (26), (27) if NCIR < 2
o Omit items (26), (27) if NCF = 0
+ Omit items (28) - (29) if NCHINE = 0

(e) Page 5

Figure 22.- Continued.

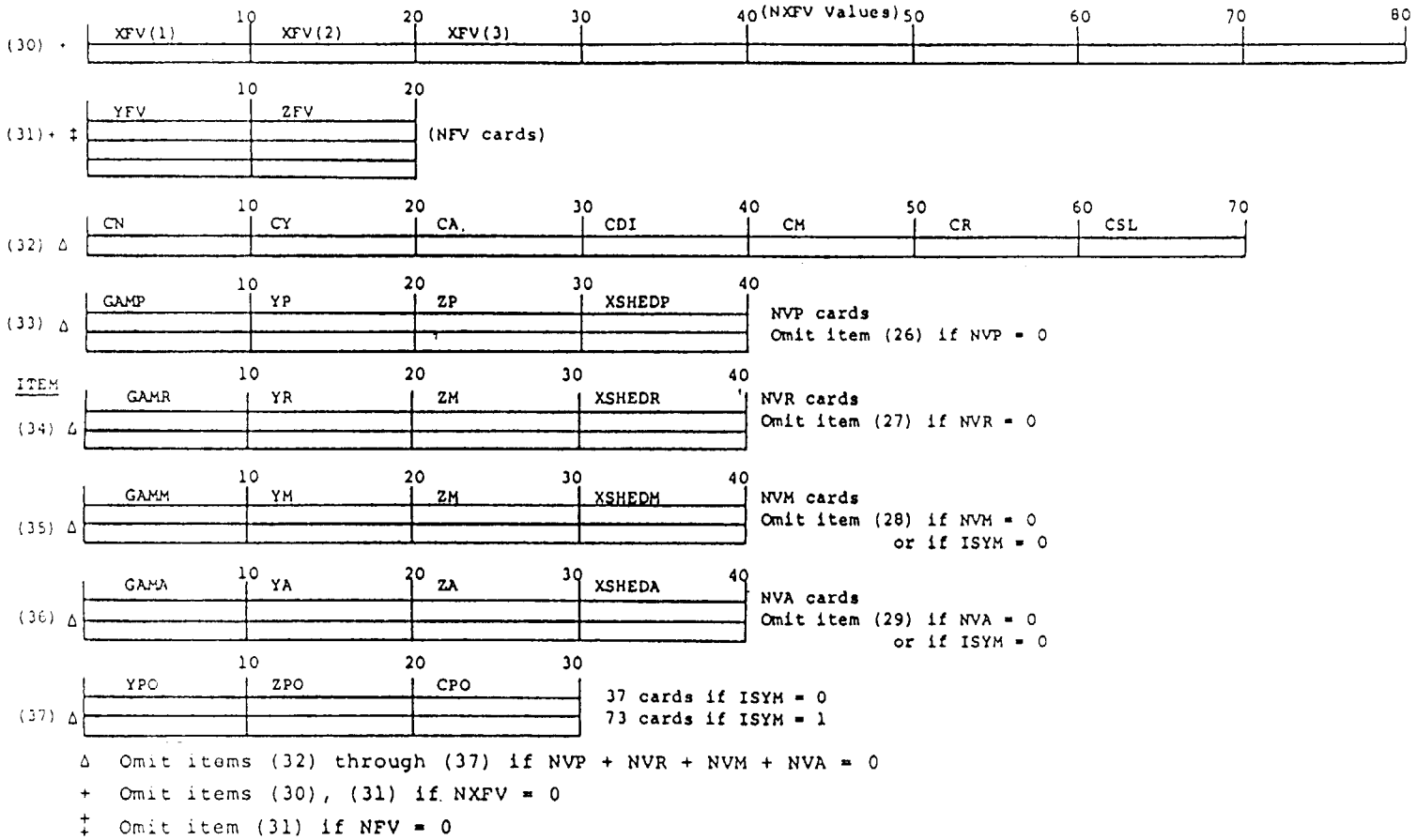

(f) Page 6

Figure 22.- Concluded.

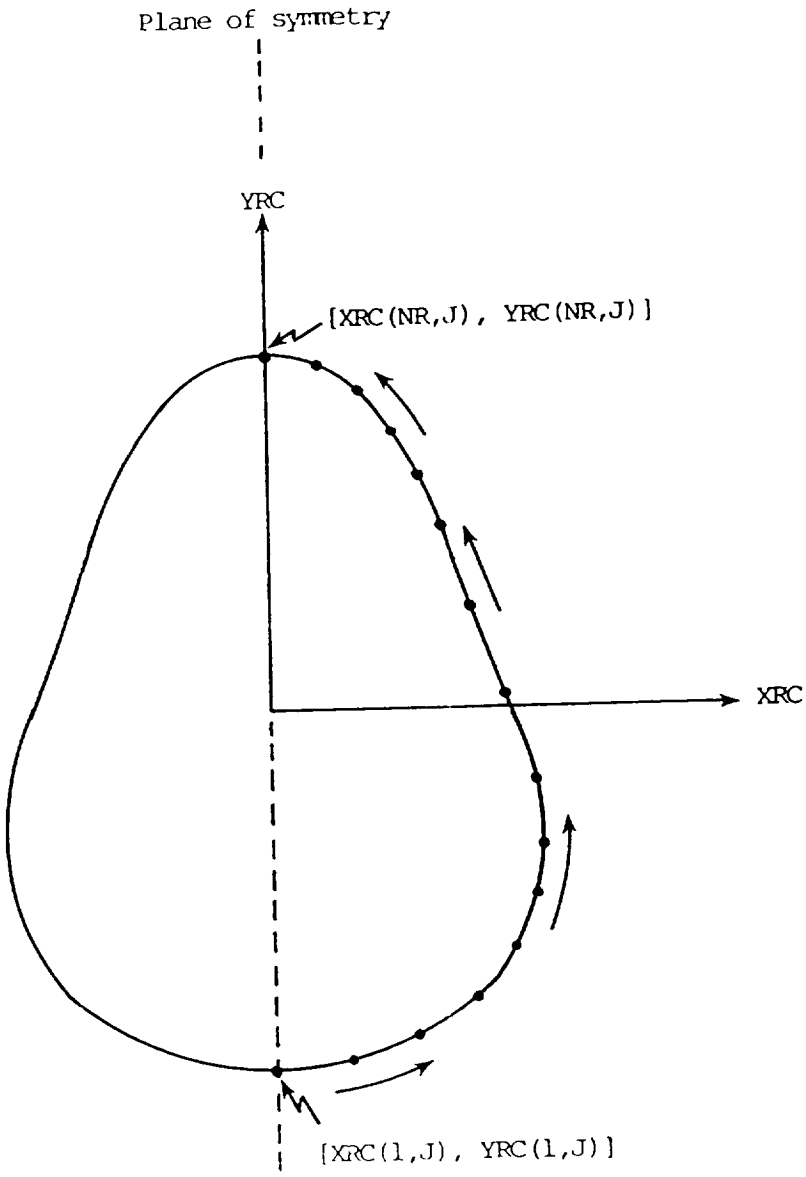

(a) Noncircular cross section

Figure 23.- Convention for ordering coordinates for a noncircular cross section at X = XFC(J).

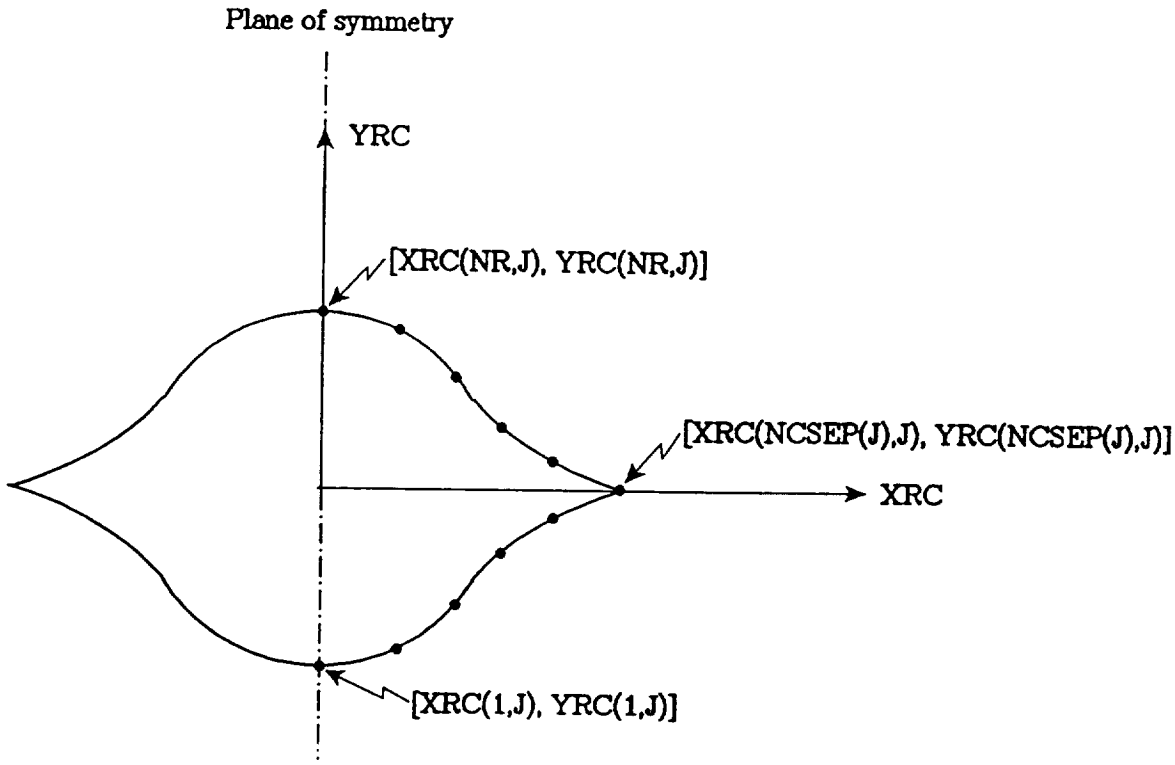

(b) Chine cross section

Figure 23.- Concluded.

```
INPUT ITEM
----------

(1)      3    0    0    1    0    1    1    0    0    0    0    0    0    0    0
(2)     -1    1
(3)      4    1    1    1    3    2    0    0    0    0
(4)      NIELSEN ENGINEERING & RESEARCH, INC.                          PROGRAM VTXCHN
         CHINE BODY
         REF. AIAA 87-2617
         CHINE SAMPLE CASE 1
(5)   22.145      8.700     23.000     73.400      8.70
(6)    20.000      0.000     1000000.    0.00
(7)     0.500     14.500      0.50       0.0        0.0        1.05       0.0        1.00
(8)      .050      0.0        0.0        0.0        0.0        0.0        0.0        0.05
(9)     -1    2
(12)    29
(13)    0.00000    0.01962    0.03910    0.05872    0.07834    0.09796    0.11744    0.13787
        0.18474    0.20354    0.23501    0.27166    0.34060    0.47684    0.61308    0.74932
        0.93120    1.00000    1.03665    1.06812    1.08692    1.13379    1.15422    1.17371
        1.19332    1.21294    1.23256    1.25204    1.27166
(14)    0.00000    0.00603    0.01151    0.01615    0.02061    0.02419    0.02791    0.03059
        0.03463    0.03561    0.03682    0.03799    0.03799    0.03799    0.03799    0.03799
        0.03799    0.03799    0.03682    0.03561    0.03463    0.03059    0.02791    0.02419
        0.02061    0.01615    0.01151    0.00603    0.00000
(15)    0.31992    0.29440    0.25906    0.23181    0.20492    0.18673    0.16184    0.11756
        0.06198    0.04712    0.03537    0.02074    0.00000    0.00000    0.00000    0.00000
        0.00000   -0.02072   -0.03537   -0.04712   -0.06198   -0.11756   -0.16184   -0.18673
       -0.20492   -0.23181   -0.25906   -0.29440   -0.31992
(18a)   0.00000    0.00585    0.01121    0.01612    0.02059    0.02461    0.02817    0.03146
        0.03715    0.03869    0.04051    0.04134    0.04134    0.04134    0.04134    0.04134
        0.04134    0.04134    0.04052    0.03869    0.03715    0.03146    0.02817    0.02460
        0.02059    0.01612    0.01122    0.00588    0.00000
(18b)   0.31155    0.28714    0.26334    0.23980    0.21662    0.19376    0.17135    0.14810
        0.09562    0.07482    0.04018    0.00000    0.00000    0.00000    0.00000    0.00000
        0.00000    0.00000   -0.04017   -0.07482   -0.09562   -0.14810   -0.17135   -0.19377
       -0.21662   -0.23980   -0.26333   -0.28713   -0.31155
(20a)   30    3
(20b)   7.19      13.56      19.94
(21)     7    7    7
(22)    12
(23a)  0.00000E+00 0.26583E+00 0.54375E+00 0.83375E+00 1.64333E+00 1.95750E+00
       2.90000E+00 1.88500E+00 0.84583E+00 0.54375E+00 0.29000E+00 0.00000E+00
(23b) -1.66750E+00-1.64333E+00-1.57083E+00-1.46208E+00-0.76125E+00-0.29725E+00
       0.00000E+00 0.31417E+00 1.20833E+00 1.51042E+00 1.72792E+00 1.83667E+00
(22)    12
(23a)  0.00000E+00 0.41083E+00 0.78542E+00 1.20833E+00 2.35625E+00 2.90000E+00
       4.13250E+00 2.87583E+00 1.14792E+00 0.79750E+00 0.39875E+00 0.00000E+00
(23b) -2.32000E+00-2.29583E+00-2.19917E+00-2.03000E+00-1.13583E+00-0.43500E+00
       0.00000E+00 0.44708E+00 2.03000E+00 2.29583E+00 2.51333E+00 2.59792E+00
(22)    12
(23a)  0.00000E+00 0.46060E+00 0.90719E+00 1.32622E+00 2.41107E+00 3.15905E+00
       4.35000E+00 3.15905E+00 1.32622E+00 0.90719E+00 0.46060E+00 0.00000E+00
(23b) -2.65240E+00-2.61210E+00-2.49247E+00-2.29709E+00-1.23073E+00-0.48274E+00
       0.00000E+00 0.48274E+00 2.29709E+00 2.49247E+00 2.61210E+00 2.65240E+00
(28)     8   0.2500
(29a)   0.00      30.00
(29b)    3    3    3
(29c)    1    1
(29d)   1.00       1.00
```

Figure 24.- Sample case 1 input file.

```
INPUT ITEM
----------

(1)       3    0    0    1    0    1    1    0    0    0    0    0    0    0    0    0
(2)      -1    1    0
(3)       3    1    1    1    3    2    0    0    0    0
(4)       NIELSEN ENGINEERING & RESEARCH, INC.                              PROGRAM VTXCHN
          CIRCULAR - CHINE BODY
          SAMPLE CASE 2
(5)      3.14159     2.0000     10.000     20.000      2.0000
(6)      20.000      0.000      1000000.    0.00
(7)       0.50      13.000       0.50       0.0         0.0         1.05        0.0         1.00
(8)        .030      0.0         0.0        0.0         0.0         0.0         0.0         0.05
(9)      -1    2
(12)     35
(13)      0.00000    0.00164    0.00656    0.01468    0.02594    0.04019    0.05729    0.07706
          0.09926    0.12366    0.15000    0.17798    0.20729    0.23763    0.26864    0.30000
          0.35       0.65       0.95       1.00000    1.03136    1.06237    1.09271    1.12202
          1.15000    1.17634    1.20074    1.22294    1.24271    1.25981    1.27406    1.28532
          1.29344    1.29836    1.30000
(14)      0.00000    0.00056    0.00222    0.00490    0.00847    0.01276    0.01759    0.02273
          0.02796    0.03304    0.03776    0.04192    0.04534    0.04789    0.04947    0.05000
           .05838     .05907     .05838     0.05000    0.04947    0.04789    0.04534    0.04192
          0.03776    0.03304    0.02796    0.02273    0.01759    0.01276    0.00847    0.00490
          0.00222    0.00056    0.00000
(15)      0.34286    0.34076    0.33452    0.32426    0.31021    0.29265    0.27191    0.24834
          0.22231    0.19419    0.16434    0.13308    0.10073    0.06758    0.03392    0.00000
           .02600     .00000    -.02600     0.00000   -0.03392   -0.06758   -0.10073   -0.13308
         -0.16434   -0.19419   -0.22231   -0.24834   -0.27191   -0.29265   -0.31021   -0.32426
         -0.33452   -0.34076   -0.34286
(18a)     0.00000    0.00056    0.00222    0.00490    0.00847    0.01276    0.01759    0.02273
          0.02796    0.03304    0.03776    0.04192    0.04534    0.04789    0.04947    0.05000
           .05209     .05618     .05209     0.05000    0.04947    0.04789    0.04534    0.04192
          0.03776    0.03304    0.02796    0.02273    0.01759    0.01276    0.00847    0.00490
          0.00222    0.00056    0.00000
(18b)     0.34286    0.34076    0.33452    0.32426    0.31021    0.29265    0.27191    0.24834
          0.22231    0.19419    0.16434    0.13308    0.10073    0.06758    0.03392    0.00000
           .01540     .00000    -.01540     0.00000   -0.03392   -0.06758   -0.10073   -0.13308
         -0.16434   -0.19419   -0.22231   -0.24834   -0.27191   -0.29265   -0.31021   -0.32426
         -0.33452   -0.34076   -0.34286
(20a)     25    5
(20b)     6.00       7.00       13.00      19.00      20.00
(21)      10   10    10   10    10
(22)      19
(23a)  0.00000E+00 0.17365E+00 0.34202E+00 0.50000E+00 0.64279E+00 0.76604E+00
       0.86603E+00 0.93969E+00 0.98481E+00 0.10000E+01 0.98481E+00 0.93969E+00
       0.86603E+00 0.76604E+00 0.64279E+00 0.50000E+00 0.34202E+00 0.17365E+00
       0.00000E+00
(23b) -0.10000E+01-0.98481E+00-0.93969E+00-0.86603E+00-0.76604E+00-0.64279E+00
      -0.50000E+00-0.34202E+00-0.17365E+00 0.00000E+00 0.17365E+00 0.34202E+00
       0.50000E+00 0.64279E+00 0.76604E+00 0.86603E+00 0.93969E+00 0.98481E+00
       0.10000E+01
(22)      19
(23a)  0.00000E+00 0.17365E+00 0.34202E+00 0.50000E+00 0.64279E+00 0.76604E+00
       0.86603E+00 0.93969E+00 0.98481E+00 0.13000E+01 0.98481E+00 0.93969E+00
       0.86603E+00 0.76604E+00 0.64279E+00 0.50000E+00 0.34202E+00 0.17365E+00
       0.00000E+00
(23b) -0.10000E+01-0.98481E+00-0.93969E+00-0.86603E+00-0.76604E+00-0.64279E+00
      -0.50000E+00-0.34202E+00-0.17365E+00 0.00000E+00 0.17365E+00 0.34202E+00
       0.50000E+00 0.64279E+00 0.76604E+00 0.86603E+00 0.93969E+00 0.98481E+00
       0.10000E+01
```

(a) Page 1

Figure 25.- Sample case 2 input file.

```
(22)      19
(23a)   0.00000E+00 0.17365E+00 0.34202E+00 0.50000E+00 0.64279E+00 0.76604E+00
        0.86603E+00 0.93969E+00 0.98481E+00 0.10000E+01 0.98481E+00 0.93969E+00
        0.86603E+00 0.76604E+00 0.64279E+00 0.50000E+00 0.34202E+00 0.17365E+00
        0.00000E+00
(23b) -0.10000E+01-0.98481E+00-0.93969E+00-0.86603E+00-0.76604E+00-0.64279E+00
      -0.50000E+00-0.34202E+00-0.17365E+00 0.00000E+00 0.17365E+00 0.34202E+00
        0.50000E+00 0.64279E+00 0.76604E+00 0.86603E+00 0.93969E+00 0.98481E+00
        0.10000E+01
(22)      19
(23a)   0.00000E+00 0.17365E+00 0.34202E+00 0.50000E+00 0.64279E+00 0.76604E+00
        0.86603E+00 0.93969E+00 0.98481E+00 0.13000E+01 0.98481E+00 0.93969E+00
        0.86603E+00 0.76604E+00 0.64279E+00 0.50000E+00 0.34202E+00 0.17365E+00
        0.00000E+00
(23b) -0.10000E+01-0.98481E+00-0.93969E+00-0.86603E+00-0.76604E+00-0.64279E+00
      -0.50000E+00-0.34202E+00-0.17365E+00 0.00000E+00 0.17365E+00 0.34202E+00
        0.50000E+00 0.64279E+00 0.76604E+00 0.86603E+00 0.93969E+00 0.98481E+00
        0.10000E+01
(22)      19
(23a)   0.00000E+00 0.17365E+00 0.34202E+00 0.50000E+00 0.64279E+00 0.76604E+00
        0.86603E+00 0.93969E+00 0.98481E+00 0.10000E+01 0.98481E+00 0.93969E+00
        0.86603E+00 0.76604E+00 0.64279E+00 0.50000E+00 0.34202E+00 0.17365E+00
        0.00000E+00
(23b) -0.10000E+01-0.98481E+00-0.93969E+00-0.86603E+00-0.76604E+00-0.64279E+00
      -0.50000E+00-0.34202E+00-0.17365E+00 0.00000E+00 0.17365E+00 0.34202E+00
        0.50000E+00 0.64279E+00 0.76604E+00 0.86603E+00 0.93969E+00 0.98481E+00
        0.10000E+01
(28)       0   0.5000
(29a)    6.00      20.00
(29b)     0    3     0
(29c)     1    1
(29d)    0.60       0.60
```

(b) Page 2

Figure 25.- Concluded.

```
NIELSEN ENGINEERING & RESEARCH, INC.                    PROGRAM VTXCHN
CHINE BODY
REF. AIAA 87-2617
CHINE SAMPLE CASE 1


      REFERENCE QUANTITIES
        REF. AREA ........   22.15
        REF. LENGTH ......    8.70
        X(MOMENT CENTER) .   23.00
        BODY LENGTH (L)...   73.40
        BASE DIAMETER (D).    8.70
        STRATFORD (LAM)...   0.087
        STRATFORD (TURB)..   0.350


      FLOW CONDITIONS
        ALPHA C (DEG.) ...   20.00
        PHI (DEG.) .......    0.00
        MACH NUMBER ......    0.00
        REYNOLDS NO. (D)..    1.000E+06
        VORTEX FACTOR ....    1.00

        ALPHA (DEG.) .....   20.00
        BETA (DEG.) ......    0.00
        U/V0 .............   0.940
        V0*DT ............   0.532
        RE/D .............    1.149E+05
        RE/D SIN(ALPHA) ..    3.931E+04


      INITIAL CONDITIONS      XI        XF        DX       XTR1      XTR2       TOL       EMKF      RGAM     RCORE/D
                            0.500     14.500     0.500     15.950    24.650   0.05000     1.050     0.000      0.050

      OPTIONS...

   NCIR    NCF   ISYM  NBLSEP  NSEPR  NDFUS  NDPHI   INP   NXFV   NFV   NVP   NVR   NVM   NVA  NASYM  NVPHI  NCHINE
      3      0      0       1      0      1      1     0      0     0     0     0     0     0      0     -1       1

   NPRNTP NPRNTS NPRNTV NPLOTV NPLOTA   NTH   NCORE NSKIN  NCOMP  NDADT
      1      1      1      3      2      0      0     0      0      0


DEFINITIONS OF OUTPUT QUANTITIES ...
     CA(X)      (DCA/DX)/(Q*D) , POSITIVE AFT
     CN(X)      (DCN/DX)/(Q*D) , POSITIVE UP
     CY(X)      (DCY/DX)/(Q*D) , POSITIVE RIGHT
     CA         FX/(Q*REFS) , POSITIVE AFT
     CN         FZ/(Q*REFS) , POSITIVE UP
     CY         FY/(Q*REFS) , POSITIVE RIGHT
     CM         M/(Q*REFS*REFL) , POSITIVE NOSE UP
     CR         R/(Q*REFS*REFL) , POSITIVE NOSE RIGHT
     CLL        L/(Q*REFS*REFL) , POSITIVE COUNTERCLOCKWISE
```

(a) Page 1

Figure 26.- Sample case 1 output.

INPUT GEOMETRY CHARACTERISTICS
NXR = 29

X/L	REQ/L	DREQ/DX	X	REQ
0.0000	0.0000	0.3199	0.0000	0.0000
0.0196	0.0060	0.2944	1.4401	0.4426
0.0391	0.0115	0.2591	2.8699	0.8448
0.0587	0.0161	0.2318	4.3100	1.1854
0.0783	0.0206	0.2049	5.7502	1.5128
0.0980	0.0242	0.1867	7.1903	1.7755
0.1174	0.0279	0.1618	8.6201	2.0486
0.1379	0.0306	0.1176	10.1197	2.2453
0.1847	0.0346	0.0620	13.5599	2.5418
0.2035	0.0356	0.0471	14.9398	2.6138
0.2360	0.0368	0.0354	17.2497	2.7026
0.2717	0.0380	0.0207	19.9398	2.7885
0.3406	0.0380	0.0000	25.0000	2.7885
0.4768	0.0380	0.0000	35.0001	2.7885
0.6131	0.0380	0.0000	45.0001	2.7885
0.7493	0.0380	0.0000	55.0001	2.7885
0.9312	0.0380	0.0000	68.3501	2.7885
1.0000	0.0380	-0.0207	73.4000	2.7885
1.0366	0.0368	-0.0354	76.0901	2.7026
1.0681	0.0356	-0.0471	78.4000	2.6138
1.0869	0.0346	-0.0620	79.7799	2.5418
1.1338	0.0306	-0.1176	83.2202	2.2453
1.1542	0.0279	-0.1618	84.7197	2.0486
1.1737	0.0242	-0.1867	86.1503	1.7755
1.1933	0.0206	-0.2049	87.5897	1.5128
1.2129	0.0161	-0.2318	89.0298	1.1854
1.2326	0.0115	-0.2591	90.4699	0.8448
1.2520	0.0060	-0.2944	91.8997	0.4426
1.2717	0.0000	-0.3199	93.3398	0.0000

(b) Page 2

Figure 26.- Continued.

SOURCE LOCATIONS AND BODY RADIUS AND SURFACE SLOPE AT THESE LOCATIONS

SOURCE SPACING IS 0.75000 TIMES LOCAL RADIUS

X/L	0.00200	0.00246	0.00303	0.00373	0.00459	0.00564	0.00694
R/L	0.00061	0.00076	0.00093	0.00115	0.00141	0.00173	0.00213
DR/DX	0.31732	0.31672	0.31598	0.31507	0.31396	0.31258	0.31089
X/L	0.00854	0.01051	0.01294	0.01592	0.01959	0.02410	0.02957
R/L	0.00263	0.00323	0.00398	0.00489	0.00602	0.00729	0.00883
DR/DX	0.30881	0.30625	0.30309	0.29922	0.29444	0.28827	0.27635
X/L	0.03619	0.04421	0.05375	0.06498	0.07816	0.09358	0.11113
R/L	0.01069	0.01272	0.01497	0.01757	0.02057	0.02339	0.02670
DR/DX	0.26434	0.25196	0.23872	0.22323	0.20517	0.19079	0.16991
X/L	0.13116	0.15344	0.17739	0.20288	0.22956	0.25702	0.28516
R/L	0.02971	0.03193	0.03400	0.03558	0.03661	0.03752	0.03799
DR/DX	0.13211	0.09910	0.07070	0.04764	0.03740	0.02658	0.01668
X/L	0.31366	0.34215	0.37064	0.39913	0.42763	0.45612	0.48461
R/L	0.03799	0.03799	0.03799	0.03799	0.03799	0.03799	0.03799
DR/DX	0.00811	0.00000	0.00000	0.00000	0.00000	0.00000	0.00000
X/L	0.51310	0.54160	0.57009	0.59858	0.62707	0.65557	0.68406
R/L	0.03799	0.03799	0.03799	0.03799	0.03799	0.03799	0.03799
DR/DX	0.00000	0.00000	0.00000	0.00000	0.00000	0.00000	0.00000
X/L	0.71255	0.74104	0.76954	0.79803	0.82652	0.85501	0.88351
R/L	0.03799	0.03799	0.03799	0.03799	0.03799	0.03799	0.03799
DR/DX	0.00000	0.00000	0.00000	0.00000	0.00000	0.00000	0.00000
X/L	0.91200	0.94049	0.96898	0.99748	1.02597	1.05384	1.08096
R/L	0.03799	0.03799	0.03799	0.03799	0.03716	0.03616	0.03494
DR/DX	0.00000	-0.00280	-0.01138	-0.01996	-0.03110	-0.04179	-0.05727
X/L	1.10717	1.13183	1.15490	1.17573	1.19360	1.20901	1.22179
R/L	0.03288	0.03076	0.02778	0.02382	0.02055	0.01704	0.01406
DR/DX	-0.08599	-0.11523	-0.16271	-0.18881	-0.20530	-0.22642	-0.24410
X/L	1.23233	1.24101	1.24786	1.25328	1.25750	1.26077	1.26328
R/L	0.01156	0.00913	0.00721	0.00565	0.00435	0.00335	0.00258
DR/DX	-0.25875	-0.27438	-0.28681	-0.29599	-0.30151	-0.30575	-0.30902
X/L	1.26521						
R/L	0.00198						
DR/DX	-0.31153						

X(ST)	XS(1)	X(RM)	R(MAX)	XS(L)	X(ST)
0.00169	0.00200	0.27168	0.03799	1.26668	1.26820

(c) Page 3

Figure 26.- Continued.

FOR THIS CASE THERE ARE 71 SOURCES

X/L	2.0000E-03	2.4610E-03	3.0283E-03	3.7263E-03	4.5852E-03	5.6422E-03
Q	6.9391E-08	1.5171E-08	8.7780E-08	9.3383E-08	1.6719E-07	2.3969E-07
X/L	6.9427E-03	8.5430E-03	1.0512E-02	1.2935E-02	1.5917E-02	1.9586E-02
Q	3.7472E-07	5.6527E-07	8.6412E-07	1.3152E-06	1.9884E-06	3.1042E-06
X/L	2.4101E-02	2.9569E-02	3.6190E-02	4.4209E-02	5.3747E-02	6.4978E-02
Q	4.5911E-06	6.5068E-06	9.4576E-06	1.3641E-05	1.7509E-05	2.4059E-05
X/L	7.8157E-02	9.3583E-02	1.1113E-01	1.3116E-01	1.5344E-01	1.7739E-01
Q	3.0421E-05	3.8356E-05	4.8201E-05	5.9922E-05	2.0738E-05	5.0476E-05
X/L	2.0288E-01	2.2956E-01	2.5702E-01	2.8516E-01	3.1366E-01	3.4215E-01
Q	3.4914E-08	2.7479E-05	1.3125E-05	5.3656E-06	7.3576E-06	-9.1544E-06
X/L	3.7064E-01	3.9913E-01	4.2763E-01	4.5612E-01	4.8461E-01	5.1310E-01
Q	4.1969E-06	-5.1886E-06	4.3805E-06	-4.9101E-06	4.5378E-06	-4.8024E-06
X/L	5.4160E-01	5.7009E-01	5.9858E-01	6.2707E-01	6.5557E-01	6.8406E-01
Q	4.8158E-06	-4.7422E-06	4.6653E-06	-4.6986E-06	4.7063E-06	-4.6570E-06
X/L	7.1255E-01	7.4104E-01	7.6954E-01	7.9803E-01	8.2652E-01	8.5501E-01
Q	4.7515E-06	-4.6042E-06	4.8172E-06	-4.5173E-06	4.9399E-06	-4.3351E-06
X/L	8.8351E-01	9.1200E-01	9.4049E-01	9.6898E-01	9.9748E-01	1.0260E+00
Q	5.2932E-06	-4.3245E-06	1.2747E-05	-1.8080E-05	2.8700E-06	-2.9473E-05
X/L	1.0538E+00	1.0810E+00	1.1072E+00	1.1318E+00	1.1549E+00	1.1767E+00
Q	-9.2092E-06	-2.7861E-05	-3.6873E-05	-4.6932E-05	-6.2039E-05	-4.4803E-05
X/L	1.1936E+00	1.2090E+00	1.2218E+00	1.2323E+00	1.2410E+00	1.2479E+00
Q	-3.5954E-05	-2.6898E-05	-1.8986E-05	-1.3570E-05	-8.6058E-06	-5.5527E-06
X/L	1.2533E+00	1.2575E+00	1.2608E+00	1.2633E+00	1.2652E+00	
Q	-3.4385E-06	-1.9056E-06	-1.3171E-06	-4.5432E-07	-7.6060E-07	

(d) Page 4

Figure 26.- Continued.

SHAPE CALCULATED FROM SOURCE DISTRIBUTION

X/L	0.01000	0.02000	0.03000	0.04000	0.05000	0.06000	0.07000
R/L(S.D.)	0.00307	0.00608	0.00894	0.01162	0.01413	0.01649	0.01872
R/L(INPT)	0.00307	0.00614	0.00895	0.01172	0.01409	0.01644	0.01871
M-INDEX	1	2	1	2	2	2	1
X/L	0.08000	0.09000	0.10000	0.11000	0.12000	0.13000	0.14000
R/L(S.D.)	0.02082	0.02281	0.02470	0.02647	0.02811	0.02959	0.03086
R/L(INPT)	0.02091	0.02274	0.02458	0.02649	0.02825	0.02956	0.03077
M-INDEX	2	2	2	2	2	2	2
X/L	0.15000	0.16000	0.17000	0.18000	0.19000	0.20000	0.21000
R/L(S.D.)	0.03193	0.03286	0.03370	0.03446	0.03510	0.03562	0.03606
R/L(INPT)	0.03164	0.03250	0.03336	0.03422	0.03490	0.03543	0.03586
M-INDEX	2	2	2	2	2	2	2
X/L	0.22000	0.23000	0.24000	0.25000	0.26000	0.27000	0.28000
R/L(S.D.)	0.03645	0.03684	0.03720	0.03752	0.03780	0.03804	0.03823
R/L(INPT)	0.03624	0.03663	0.03698	0.03730	0.03762	0.03794	0.03799
M-INDEX	2	2	2	2	2	2	2
X/L	0.29000	0.30000	0.31000	0.32000	0.33000	0.34000	0.35000
R/L(S.D.)	0.03839	0.03853	0.03864	0.03872	0.03876	0.03878	0.03879
R/L(INPT)	0.03799	0.03799	0.03799	0.03799	0.03799	0.03799	0.03799
M-INDEX	2	2	2	2	2	2	2
X/L	0.36000	0.37000	0.38000	0.39000	0.40000	0.41000	0.42000
R/L(S.D.)	0.03879	0.03879	0.03880	0.03880	0.03879	0.03879	0.03879
R/L(INPT)	0.03799	0.03799	0.03799	0.03799	0.03799	0.03799	0.03799
M-INDEX	2	2	2	2	2	2	2
X/L	0.43000	0.44000	0.45000	0.46000	0.47000	0.48000	0.49000
R/L(S.D.)	0.03880	0.03880	0.03880	0.03879	0.03879	0.03879	0.03880
R/L(INPT)	0.03799	0.03799	0.03799	0.03799	0.03799	0.03799	0.03799
M-INDEX	2	2	2	2	2	2	2
X/L	0.50000	0.51000	0.52000	0.53000	0.54000	0.55000	0.56000
R/L(S.D.)	0.03880	0.03880	0.03879	0.03879	0.03880	0.03880	0.03880
R/L(INPT)	0.03799	0.03799	0.03799	0.03799	0.03799	0.03799	0.03799
M-INDEX	2	2	2	2	2	2	2
X/L	0.57000	0.58000	0.59000	0.60000	0.61000	0.62000	0.63000
R/L(S.D.)	0.03880	0.03879	0.03879	0.03880	0.03880	0.03880	0.03879
R/L(INPT)	0.03799	0.03799	0.03799	0.03799	0.03799	0.03799	0.03799
M-INDEX	2	2	2	2	2	2	2
X/L	0.64000	0.65000	0.66000	0.67000	0.68000	0.69000	0.70000
R/L(S.D.)	0.03879	0.03879	0.03880	0.03880	0.03880	0.03879	0.03879
R/L(INPT)	0.03799	0.03799	0.03799	0.03799	0.03799	0.03799	0.03799
M-INDEX	2	2	2	2	2	2	2
X/L	0.71000	0.72000	0.73000	0.74000	0.75000	0.76000	0.77000
R/L(S.D.)	0.03879	0.03880	0.03880	0.03880	0.03879	0.03879	0.03880
R/L(INPT)	0.03799	0.03799	0.03799	0.03799	0.03799	0.03799	0.03799
M-INDEX	2	2	2	2	2	2	2
X/L	0.78000	0.79000	0.80000	0.81000	0.82000	0.83000	0.84000
R/L(S.D.)	0.03880	0.03880	0.03879	0.03879	0.03879	0.03880	0.03880
R/L(INPT)	0.03799	0.03799	0.03799	0.03799	0.03799	0.03799	0.03799
M-INDEX	2	2	2	2	2	2	2

(e) Page 5

Figure 26.- Continued.

X/L	0.85000	0.86000	0.87000	0.88000	0.89000	0.90000	0.91000
R/L(S.D.)	0.03880	0.03879	0.03879	0.03879	0.03880	0.03880	0.03879
R/L(INPT)	0.03799	0.03799	0.03799	0.03799	0.03799	0.03799	0.03799
M-INDEX	2	2	2	2	2	2	2
X/L	0.92000	0.93000	0.94000	0.95000	0.96000	0.97000	0.98000
R/L(S.D.)	0.03879	0.03879	0.03878	0.03875	0.03868	0.03856	0.03842
R/L(INPT)	0.03799	0.03799	0.03799	0.03799	0.03799	0.03799	0.03799
M-INDEX	2	2	2	2	2	2	2
X/L	0.99000	1.00000	1.01000	1.02000	1.03000	1.04000	1.05000
R/L(S.D.)	0.03826	0.03808	0.03787	0.03760	0.03727	0.03692	0.03654
R/L(INPT)	0.03799	0.03799	0.03787	0.03735	0.03703	0.03669	0.03631
M-INDEX	2	2	2	2	2	2	2
X/L	1.06000	1.07000	1.08000	1.09000	1.10000	1.11000	1.12000
R/L(S.D.)	0.03614	0.03569	0.03517	0.03455	0.03384	0.03302	0.03208
R/L(INPT)	0.03592	0.03551	0.03499	0.03436	0.03350	0.03264	0.03178
M-INDEX	2	2	2	2	2	2	2
X/L	1.13000	1.14000	1.15000	1.16000	1.17000	1.18000	1.19000
R/L(S.D.)	0.03101	0.02977	0.02835	0.02674	0.02498	0.02311	0.02114
R/L(INPT)	0.03092	0.02978	0.02846	0.02681	0.02490	0.02304	0.02122
M-INDEX	2	1	2	2	2	2	2
X/L	1.20000	1.21000	1.22000	1.23000	1.24000	1.25000	1.26000
R/L(S.D.)	0.01905	0.01684	0.01449	0.01199	0.00932	0.00646	0.00335
R/L(INPT)	0.01909	0.01682	0.01448	0.01212	0.00942	0.00660	0.00358
M-INDEX	2	1	2	2	2	2	2

(f) Page 6

Figure 26.- Continued.

VELOCITIES ON THE BODY SURFACE

		VELOCITIES			
		AXIAL	RADIAL	TANGEN	NORMAL
X/L	R/L	VA/V0	VR/V0	VT/V0	VN/V0
0.00169	0.00052	-0.33774	0.20448	-0.25997	0.29715
0.01000	0.00307	-0.18808	0.24935	-0.10664	0.29356
0.02000	0.00614	-0.14678	0.24948	-0.07052	0.28073
0.03000	0.00895	-0.11708	0.24305	-0.04830	0.26543
0.04000	0.01172	-0.09406	0.23345	-0.03280	0.24954
0.05000	0.01409	-0.07545	0.22558	-0.01984	0.23704
0.06000	0.01644	-0.06090	0.21620	-0.01088	0.22435
0.07000	0.01871	-0.04709	0.20610	-0.00244	0.21140
0.08000	0.02091	-0.03512	0.19605	0.00465	0.19912
0.09000	0.02274	-0.02496	0.18963	0.01163	0.19091
0.10000	0.02458	-0.01360	0.18132	0.01946	0.18078
0.11000	0.02649	-0.00109	0.17101	0.02781	0.16873
0.12000	0.02825	0.01174	0.15729	0.03589	0.15359
0.13000	0.02958	0.02429	0.14177	0.04298	0.13726
0.14000	0.03077	0.03174	0.12047	0.04530	0.11606
0.15000	0.03164	0.03170	0.10280	0.04208	0.09900
0.16000	0.03250	0.02952	0.09156	0.03772	0.08849
0.17000	0.03336	0.03040	0.08398	0.03696	0.08131
0.18000	0.03422	0.03416	0.07363	0.03905	0.07116
0.19000	0.03490	0.03503	0.05992	0.03843	0.05780
0.20000	0.03543	0.03104	0.04834	0.03341	0.04673
0.21000	0.03586	0.02548	0.04219	0.02734	0.04101
0.22000	0.03624	0.02206	0.04025	0.02369	0.03931
0.23000	0.03663	0.02185	0.03875	0.02328	0.03791
0.24000	0.03698	0.02279	0.03540	0.02396	0.03462
0.25000	0.03730	0.02313	0.03096	0.02403	0.03027
0.26000	0.03762	0.02286	0.02634	0.02352	0.02575
0.27000	0.03794	0.02198	0.02188	0.02244	0.02140
0.28000	0.03799	0.02074	0.01815	0.02107	0.01777
0.29000	0.03799	0.01952	0.01510	0.01975	0.01481
0.30000	0.03799	0.01855	0.01247	0.01870	0.01224
0.31000	0.03799	0.01795	0.00983	0.01804	0.00966
0.32000	0.03799	0.01733	0.00665	0.01737	0.00654
0.33000	0.03799	0.01586	0.00318	0.01587	0.00313
0.34000	0.03799	0.01329	0.00060	0.01329	0.00060
0.35000	0.03799	0.01054	-0.00022	0.01054	-0.00022
0.36000	0.03799	0.00877	0.00023	0.00877	0.00023
0.37000	0.03799	0.00815	0.00067	0.00815	0.00067
0.38000	0.03799	0.00793	0.00036	0.00793	0.00036
0.39000	0.03799	0.00729	-0.00039	0.00729	-0.00039
0.40000	0.03799	0.00614	-0.00073	0.00614	-0.00073
0.41000	0.03799	0.00514	-0.00027	0.00514	-0.00027
0.42000	0.03799	0.00488	0.00049	0.00488	0.00049
0.43000	0.03799	0.00520	0.00070	0.00520	0.00070
0.44000	0.03799	0.00539	0.00015	0.00539	0.00015
0.45000	0.03799	0.00490	-0.00057	0.00490	-0.00057
0.46000	0.03799	0.00400	-0.00067	0.00400	-0.00067
0.47000	0.03799	0.00342	-0.00003	0.00342	-0.00003
0.48000	0.03799	0.00358	0.00064	0.00358	0.00064
0.49000	0.03799	0.00412	0.00061	0.00412	0.00061
0.50000	0.03799	0.00426	-0.00009	0.00426	-0.00009
0.51000	0.03799	0.00371	-0.00069	0.00371	-0.00069
0.52000	0.03799	0.00293	-0.00053	0.00293	-0.00053
0.53000	0.03799	0.00266	0.00021	0.00266	0.00021
0.54000	0.03799	0.00309	0.00072	0.00309	0.00072
0.55000	0.03799	0.00366	0.00044	0.00366	0.00044
0.56000	0.03799	0.00366	-0.00032	0.00366	-0.00032
0.57000	0.03799	0.00303	-0.00073	0.00303	-0.00073
0.58000	0.03799	0.00239	-0.00034	0.00239	-0.00034

(g) Page 7

Figure 26.- Continued.

0.59000	0.03799	0.00240	0.00043	0.00240	0.00043
0.60000	0.03799	0.00301	0.00072	0.00301	0.00072
0.61000	0.03799	0.00351	0.00022	0.00351	0.00022
0.62000	0.03799	0.00333	-0.00052	0.00333	-0.00052
0.63000	0.03799	0.00265	-0.00069	0.00265	-0.00069
0.64000	0.03799	0.00221	-0.00011	0.00221	-0.00011
0.65000	0.03799	0.00249	0.00060	0.00249	0.00060
0.66000	0.03799	0.00319	0.00065	0.00319	0.00065
0.67000	0.03799	0.00358	-0.00001	0.00358	-0.00001
0.68000	0.03799	0.00321	-0.00066	0.00321	-0.00066
0.69000	0.03799	0.00257	-0.00058	0.00257	-0.00058
0.70000	0.03799	0.00238	0.00014	0.00238	0.00014
0.71000	0.03799	0.00288	0.00070	0.00288	0.00070
0.72000	0.03799	0.00360	0.00050	0.00360	0.00050
0.73000	0.03799	0.00381	-0.00025	0.00381	-0.00025
0.74000	0.03799	0.00335	-0.00073	0.00335	-0.00073
0.75000	0.03799	0.00282	-0.00040	0.00282	-0.00040
0.76000	0.03799	0.00290	0.00036	0.00290	0.00036
0.77000	0.03799	0.00362	0.00073	0.00362	0.00073
0.78000	0.03799	0.00432	0.00030	0.00432	0.00030
0.79000	0.03799	0.00438	-0.00046	0.00438	-0.00046
0.80000	0.03799	0.00390	-0.00071	0.00390	-0.00071
0.81000	0.03799	0.00359	-0.00018	0.00359	-0.00018
0.82000	0.03799	0.00401	0.00055	0.00401	0.00055
0.83000	0.03799	0.00494	0.00068	0.00494	0.00068
0.84000	0.03799	0.00562	0.00006	0.00562	0.00006
0.85000	0.03799	0.00563	-0.00062	0.00563	-0.00062
0.86000	0.03799	0.00532	-0.00062	0.00532	-0.00062
0.87000	0.03799	0.00544	0.00006	0.00544	0.00006
0.88000	0.03799	0.00635	0.00067	0.00635	0.00067
0.89000	0.03799	0.00763	0.00054	0.00763	0.00054
0.90000	0.03799	0.00855	-0.00017	0.00855	-0.00017
0.91000	0.03799	0.00902	-0.00062	0.00902	-0.00062
0.92000	0.03799	0.00979	-0.00032	0.00979	-0.00032
0.93000	0.03799	0.01186	0.00005	0.01186	0.00005
0.94000	0.03799	0.01523	-0.00113	0.01524	-0.00109
0.95000	0.03799	0.01836	-0.00485	0.01838	-0.00474
0.96000	0.03799	0.01948	-0.00990	0.01956	-0.00973
0.97000	0.03799	0.01872	-0.01382	0.01888	-0.01360
0.98000	0.03799	0.01813	-0.01561	0.01836	-0.01535
1.28620	0.00168	-0.30135	-0.21552	-0.22326	-0.29586

(h) Page 8

Figure 26.- Continued.

SOURCE DISTRIBUTION REPRESENTING CIRCULAR BODY
NSOR = 71 NPRT = 2

X/L LOCATIONS

0.20000E-02 0.24610E-02 0.30283E-02 0.37263E-02 0.45852E-02 0.56422E-02
0.69427E-02 0.85430E-02 0.10512E-01 0.12935E-01 0.15917E-01 0.19586E-01
0.24101E-01 0.29669E-01 0.36190E-01 0.44209E-01 0.53747E-01 0.64978E-01
0.78157E-01 0.93583E-01 0.11113E+00 0.13116E+00 0.15344E+00 0.17739E+00
0.20288E+00 0.22956E+00 0.25702E+00 0.28516E+00 0.31366E+00 0.34215E+00
0.37064E+00 0.39913E+00 0.42763E+00 0.45612E+00 0.48461E+00 0.51310E+00
0.54160E+00 0.57009E+00 0.59858E+00 0.62707E+00 0.65557E+00 0.68406E+00
0.71255E+00 0.74104E+00 0.76954E+00 0.79803E+00 0.82652E+00 0.85501E+00
0.88351E+00 0.91200E+00 0.94049E+00 0.96898E+00 0.99748E+00 0.10260E+01
0.10538E+01 0.10810E+01 0.11072E+01 0.11318E+01 0.11549E+01 0.11757E+01
0.11936E+01 0.12090E+01 0.12218E+01 0.12323E+01 0.12410E+01 0.12479E+01
0.12533E+01 0.12575E+01 0.12608E+01 0.12633E+01 0.12652E+01

SOURCE STRENGTHS QS=Q/(4*PI*L*L*U)

0.69391E-07 0.15171E-07 0.87780E-07 0.93363E-07 0.16719E-06 0.23969E-06
0.37472E-06 0.56527E-06 0.86412E-06 0.13152E-05 0.19884E-05 0.31042E-05
0.45911E-05 0.65068E-05 0.94576E-05 0.13641E-04 0.17509E-04 0.24059E-04
0.30421E-04 0.38356E-04 0.48201E-04 0.59922E-04 0.20738E-04 0.50476E-04
0.34914E-07 0.27479E-04 0.13125E-04 0.53656E-05 0.73576E-05-0.91544E-05
0.41969E-05-0.51886E-05 0.43805E-05-0.49101E-05 0.45378E-05-0.48024E-05
0.46158E-05-0.47422E-05 0.46653E-05-0.46986E-05 0.47063E-05-0.46570E-05
0.47515E-05-0.46042E-05 0.48172E-05-0.45173E-05 0.49399E-05-0.43351E-05
0.52932E-05-0.43245E-05 0.12747E-04-0.18080E-04 0.28700E-05-0.29473E-04
-0.92092E-05-0.27861E-04-0.36873E-04-0.46932E-04-0.62039E-04-0.44803E-04
-0.35954E-04-0.26898E-04-0.18986E-04-0.13570E-04-0.86058E-05-0.55527E-05
-0.34385E-05-0.19056E-05-0.13171E-05-0.45432E-06-0.76060E-06

X/L	RO/L	DRO/DX	X	RO
0.0000	0.0000	0.3115	0.0000	0.0000
0.0196	0.0058	0.2871	1.4401	0.4294
0.0391	0.0112	0.2633	2.8699	0.8228
0.0587	0.0161	0.2398	4.3100	1.1832
0.0783	0.0206	0.2166	5.7502	1.5113
0.0980	0.0246	0.1938	7.1903	1.8064
0.1174	0.0282	0.1714	8.6201	2.0677
0.1379	0.0315	0.1481	10.1197	2.3092
0.1847	0.0371	0.0956	13.5599	2.7268
0.2035	0.0387	0.0748	14.9398	2.8398
0.2350	0.0405	0.0402	17.2497	2.9734
0.2717	0.0413	0.0000	19.9398	3.0344
0.3408	0.0413	0.0000	25.0000	3.0344
0.4768	0.0413	0.0000	35.0001	3.0344
0.6131	0.0413	0.0000	45.0001	3.0344
0.7493	0.0413	0.0000	55.0001	3.0344
0.9312	0.0413	0.0000	68.3501	3.0344
1.0000	0.0413	0.0000	73.4000	3.0344
1.0366	0.0405	-0.0402	76.0901	2.9742
1.0681	0.0387	-0.0748	78.4000	2.8398
1.0869	0.0371	-0.0956	79.7799	2.7268
1.1338	0.0315	-0.1481	83.2202	2.3092
1.1542	0.0282	-0.1714	84.7197	2.0677
1.1737	0.0246	-0.1938	86.1503	1.8056
1.1933	0.0206	-0.2166	87.5897	1.5113
1.2129	0.0161	-0.2398	89.0298	1.1832
1.2326	0.0112	-0.2633	90.4699	0.8235
1.2520	0.0059	-0.2871	91.8997	0.4301
1.2717	0.0000	-0.3115	93.3398	0.0000

(i) Page 9

Figure 26.- Continued.

INPUT BODY GEOMETRY AT XFC(1) = 7.19000

XRC (Y)	YRC (Z)
0.0000	-1.6675
0.2658	-1.6433
0.5437	-1.5708
0.8338	-1.4621
1.6433	-0.7613
1.9575	-0.2973
2.9000	0.0000
1.8850	0.3142
0.8458	1.2083
0.5437	1.5104
0.2900	1.7279
0.0000	1.8367

BODY AXIS SHIFT, ZZ = 0.0313693

CIRCLE RADIUS, RZ = 1.9581980

MAPPED AND INPUT CORNER COORDINATES

	MAPPED...		INPUT...	
I	YRT	ZRT	YR	ZR
1	0.00000	-1.68264	0.00000	-1.66750
2	0.26594	-1.65941	0.26583	-1.64333
3	0.54412	-1.58802	0.54375	-1.57083
4	0.83281	-1.47580	0.83375	-1.46208
5	1.64575	-0.77882	1.64333	-0.76125
6	1.98244	-0.34142	1.95750	-0.29725
7	2.90258	-0.01739	2.90000	0.00000
8	1.88628	0.31646	1.88500	0.31417
9	1.03457	1.03081	0.84583	1.20833
10	0.54531	1.51249	0.54375	1.51042
11	0.29004	1.72881	0.29000	1.72792
12	0.00000	1.83667	0.00000	1.83667

(j) Page 10

Figure 26.- Continued.

***** ITERATION NO. 12 *****

SERIES COEFFICIENTS

N	AN
1	-0.2646261
2	-0.0172847
3	0.1918155
4	-0.0350858
5	-0.0334423
6	-0.0042402
7	-0.0029773
8	0.0068138
9	0.0072526
10	-0.0043737
11	-0.0047305
12	-0.0004754
13	-0.0003627
14	0.0052962
15	0.0062596
16	-0.0021943
17	-0.0025676
18	-0.0022914
19	-0.0016160
20	0.0021578
21	0.0022285
22	-0.0013290
23	-0.0002803
24	-0.0022588
25	-0.0006178
26	0.0014533
27	0.0019017
28	-0.0001131
29	0.0003714
30	-0.0014244

(k) Page 11

Figure 26.- Continued.

CORRESPONDING POINTS ON BODY AND CIRCLE FOR CHINE FOR X = 7.19000

I	CIRCLE THETA	CIRCLE Y	CIRCLE Z	BODY Y	BODY Z	BETA	
1	0.0000	0.0000	-1.9582	0.0000	-1.6828	0.0000	
2	5.0000	0.1707	-1.9507	0.1711	-1.6737	5.8381	
3	10.0000	0.3400	-1.9284	0.3421	-1.6436	11.7570	
4	15.0000	0.5068	-1.8915	0.5154	-1.5971	17.8865	
5	20.0000	0.6697	-1.8401	0.6872	-1.5388	24.0660	
6	25.0000	0.8276	-1.7747	0.8420	-1.4705	29.7952	
7	30.0000	0.9791	-1.6958	0.9784	-1.3587	35.7593	
8	35.0000	1.1232	-1.6041	1.1425	-1.2137	43.2705	
9	40.0000	1.2587	-1.5001	1.3124	-1.0708	50.7885	
10	45.0000	1.3847	-1.3847	1.4877	-0.9134	58.4505	
11	50.0000	1.5001	-1.2587	1.6515	-0.7724	64.9352	
12	55.0000	1.6041	-1.1232	1.7783	-0.5693	72.2488	
13	60.0000	1.6958	-0.9791	2.0147	-0.3187	81.0097	
14	65.0000	1.7747	-0.8276	2.3058	-0.1997	85.0503	
15	70.0000	1.8401	-0.6697	2.5057	-0.1456	88.6746	
16	75.0000	1.8915	-0.5068	2.6658	-0.0888	88.0928	
17	80.0000	1.9284	-0.3400	2.7864	-0.0555	88.8583	
18	85.0000	1.9507	-0.1707	2.8650	-0.0272	89.4556	
* 19	90.5845	1.9581	0.0200	2.9026	-0.0174	89.6567	* CHINE SEPARATION POINT
20	95.0000	1.9507	0.1707	2.8786	-0.0097	89.8066	
21	100.0000	1.9284	0.3400	2.8093	0.0124	90.2521	
22	105.0000	1.8915	0.5068	2.7014	0.0454	90.9635	
23	110.0000	1.8401	0.6697	2.5560	0.0898	92.0130	
24	115.0000	1.7747	0.8276	2.3770	0.1475	93.5518	
25	120.0000	1.6958	0.9791	2.1556	0.2104	95.5755	
26	125.0000	1.6041	1.1232	1.8721	0.3243	99.8284	
27	130.0000	1.5001	1.2587	1.6125	0.5221	107.9414	
28	135.0000	1.3847	1.3847	1.4062	0.7102	116.7947	
29	140.0000	1.2587	1.5001	1.1901	0.8865	126.6817	
30	145.0000	1.1232	1.6041	0.9895	1.0742	137.3511	
31	150.0000	0.9791	1.6958	0.8048	1.2516	147.2591	
32	155.0000	0.8276	1.7747	0.6430	1.4195	155.6313	
33	160.0000	0.6697	1.8401	0.4953	1.5556	162.3392	
34	165.0000	0.5068	1.8915	0.3587	1.6764	167.9215	
35	170.0000	0.3400	1.9284	0.2422	1.7517	172.1283	
36	175.0000	0.1707	1.9507	0.1056	1.8008	176.6437	
37	180.0000	0.0000	1.9582	0.0000	1.8367	180.0000	
38	185.0000	-0.1707	1.9507	-0.1056	1.8008	183.3563	
39	190.0000	-0.3400	1.9284	-0.2422	1.7517	187.8717	
40	195.0000	-0.5068	1.8915	-0.3587	1.6764	192.0785	
41	200.0000	-0.6697	1.8401	-0.4953	1.5556	197.6608	
42	205.0000	-0.8276	1.7747	-0.6430	1.4195	204.3687	
43	210.0000	-0.9791	1.6958	-0.8048	1.2516	212.7410	
44	215.0000	-1.1232	1.6041	-0.9895	1.0742	222.6489	
45	220.0000	-1.2587	1.5001	-1.1901	0.8865	233.3184	
46	225.0000	-1.3847	1.3847	-1.4062	0.7102	243.2053	
47	230.0000	-1.5001	1.2587	-1.6125	0.5221	252.0586	
48	235.0000	-1.6041	1.1232	-1.8721	0.3243	260.1716	
49	240.0000	-1.6958	0.9791	-2.1556	0.2104	264.4245	
50	245.0000	-1.7747	0.8276	-2.3770	0.1475	266.4482	
51	250.0000	-1.8401	0.6697	-2.5560	0.0898	267.9870	
52	255.0000	-1.8915	0.5068	-2.7014	0.0454	269.0366	
53	260.0000	-1.9284	0.3400	-2.8093	0.0124	269.7479	
54	265.0000	-1.9507	0.1707	-2.8786	-0.0097	270.1934	
* 55	269.4155	-1.9581	0.0200	-2.9026	-0.0174	270.3433	* CHINE SEPARATION POINT
56	275.0000	-1.9507	-0.1707	-2.8650	-0.0272	270.5444	
57	280.0000	-1.9284	-0.3400	-2.7864	-0.0555	271.1417	
58	285.0000	-1.8915	-0.5068	-2.6658	-0.0888	271.9072	
59	290.0000	-1.8401	-0.6697	-2.5057	-0.1456	273.3254	
60	295.0000	-1.7747	-0.8276	-2.3058	-0.1997	274.9497	
61	300.0000	-1.6958	-0.9791	-2.0147	-0.3187	278.9904	

(l) Page 12

Figure 26.- Continued.

62	305.0000	-1.6041	-1.1232	-1.7783	-0.5893	287.7513
63	310.0000	-1.5001	-1.2587	-1.6515	-0.7724	295.0648
64	315.0000	-1.3847	-1.3847	-1.4877	-0.9134	301.5496
65	320.0000	-1.2587	-1.5001	-1.3124	-1.0708	309.2115
66	325.0000	-1.1232	-1.6041	-1.1425	-1.2137	316.7295
67	330.0000	-0.9791	-1.6958	-0.9784	-1.3587	324.2408
68	335.0000	-0.8276	-1.7747	-0.8420	-1.4705	330.2048
69	340.0000	-0.6697	-1.8401	-0.6872	-1.5388	335.9340
70	345.0000	-0.5068	-1.8915	-0.5154	-1.5971	342.1135
71	350.0000	-0.3400	-1.9284	-0.3421	-1.6436	348.2430
72	355.0000	-0.1707	-1.9507	-0.1711	-1.6737	354.1619
73	360.0000	0.0000	-1.9582	0.0000	-1.6828	0.0000

(m) Page 13

Figure 26.- Continued.

INPUT BODY GEOMETRY AT XFC(2) = 13.56000

XRC (Y)	YRC (Z)
0.0000	-2.3200
0.4108	-2.2958
0.7854	-2.1992
1.2083	-2.0300
2.3563	-1.1358
2.9000	-0.4350
4.1325	0.0000
2.8758	0.4471
1.1479	2.0300
0.7975	2.2958
0.3988	2.5133
0.0000	2.5979

BODY AXIS SHIFT, ZZ =-0.0303943

CIRCLE RADIUS, RZ = 2.8173275

MAPPED AND INPUT CORNER COORDINATES

	MAPPED...		INPUT...	
I	YRT	ZRT	YR	ZR
1	0.00000	-2.31520	0.00000	-2.32000
2	0.41097	-2.28988	0.41083	-2.29583
3	0.78591	-2.19382	0.78542	-2.19917
4	1.20788	-2.02178	1.20833	-2.03000
5	2.35721	-1.12858	2.35625	-1.13583
6	2.93405	-0.45531	2.90000	-0.43500
7	4.13458	0.00735	4.13250	0.00000
8	2.89800	0.47194	2.87583	0.44708
9	1.15134	2.03761	1.14792	2.03000
10	0.79788	2.29922	0.79750	2.29583
11	0.39795	2.51455	0.39875	2.51333
12	0.00000	2.59792	0.00000	2.59792

(n) Page 14

Figure 26.- Continued.

***** ITERATION NO. 13 *****

SERIES COEFFICIENTS

N	AN
1	-0.2611494
2	-0.0208124
3	0.1685687
4	-0.0170018
5	-0.0405029
6	-0.0006268
7	0.0027656
8	0.0026457
9	0.0061041
10	-0.0036377
11	-0.0066124
12	-0.0004192
13	0.0009768
14	0.0026675
15	0.0055238
16	-0.0007471
17	-0.0041913
18	-0.0011172
19	-0.0006133
20	0.0005546
21	0.0019569
22	-0.0005039
23	-0.0016407
24	-0.0005206
25	-0.0003263
26	0.0003213
27	0.0017617
28	-0.0001255
29	-0.0006746
30	-0.0000638

(o) Page 15

Figure 26.- Continued.

CORRESPONDING POINTS ON BODY AND CIRCLE FOR CHINE FOR X = 13.56000

		CIRCLE		BODY			
I	THETA	Y	Z	Y	Z	BETA	
1	0.0000	0.0000	-2.8173	0.0000	-2.3152	0.0000	
2	5.0000	0.2455	-2.8066	0.2671	-2.3071	6.3698	
3	10.0000	0.4892	-2.7745	0.5041	-2.2729	12.6050	
4	15.0000	0.7292	-2.7213	0.7498	-2.2057	18.7736	
5	20.0000	0.9636	-2.6474	0.9977	-2.1180	25.2218	
6	25.0000	1.1907	-2.5534	1.2267	-2.0108	31.3864	
7	30.0000	1.4087	-2.4399	1.4430	-1.8514	37.9337	
8	35.0000	1.6160	-2.3078	1.6883	-1.6557	45.5598	
9	40.0000	1.8109	-2.1582	1.9444	-1.4610	53.0782	
10	45.0000	1.9922	-1.9922	2.1966	-1.2609	60.1432	
11	50.0000	2.1582	-1.8109	2.4222	-1.0637	66.2923	
12	55.0000	2.3078	-1.6160	2.6145	-0.7925	73.1365	
13	60.0000	2.4399	-1.4087	2.9213	-0.4645	80.9648	
14	65.0000	2.5534	-1.1907	3.3070	-0.2760	85.2287	
15	70.0000	2.6474	-0.9636	3.5922	-0.1894	86.9814	
16	75.0000	2.7213	-0.7292	3.8111	-0.1037	88.4416	
17	80.0000	2.7745	-0.4892	3.9818	-0.0492	89.2918	
18	85.0000	2.8066	-0.2455	4.0882	-0.0081	89.8861	
* 19	89.9071	2.8173	-0.0046	4.1346	0.0073	90.1018	* CHINE SEPARATION POINT
20	95.0000	2.8066	0.2455	4.0860	0.0215	90.3015	
21	100.0000	2.7745	0.4892	3.9766	0.0653	90.9410	
22	105.0000	2.7213	0.7292	3.8092	0.1194	91.7949	
23	110.0000	2.6474	0.9636	3.5889	0.2039	93.2513	
24	115.0000	2.5534	1.1907	3.3197	0.2928	95.0402	
25	120.0000	2.4399	1.4087	2.9574	0.4376	98.4164	
26	125.0000	2.3078	1.6160	2.6050	0.6992	105.0256	
27	130.0000	2.1582	1.8109	2.3241	0.9706	112.6667	
28	135.0000	1.9922	1.9922	2.0461	1.2182	120.7888	
29	140.0000	1.8109	2.1582	1.7761	1.4690	129.5930	
30	145.0000	1.6160	2.3078	1.5192	1.7040	138.2816	
31	150.0000	1.4087	2.4399	1.2734	1.9278	146.5536	
32	155.0000	1.1907	2.5534	1.0488	2.1223	153.7031	
33	160.0000	0.9636	2.6474	0.8248	2.2815	160.1248	
34	165.0000	0.7292	2.7213	0.6084	2.4168	165.8712	
35	170.0000	0.4892	2.7745	0.4025	2.5129	170.8990	
36	175.0000	0.2455	2.8066	0.1964	2.5734	175.6360	
37	180.0000	0.0000	2.8173	0.0000	2.5979	180.0000	
38	185.0000	-0.2455	2.8066	-0.1964	2.5734	184.3641	
39	190.0000	-0.4892	2.7745	-0.4025	2.5129	189.1010	
40	195.0000	-0.7292	2.7213	-0.6084	2.4168	194.1288	
41	200.0000	-0.9636	2.6474	-0.8248	2.2815	199.8753	
42	205.0000	-1.1907	2.5534	-1.0488	2.1223	206.2969	
43	210.0000	-1.4087	2.4399	-1.2734	1.9278	213.4464	
44	215.0000	-1.6160	2.3078	-1.5192	1.7040	221.7185	
45	220.0000	-1.8109	2.1582	-1.7761	1.4690	230.4070	
46	225.0000	-1.9922	1.9922	-2.0461	1.2182	239.2312	
47	230.0000	-2.1582	1.8109	-2.3241	0.9706	247.3333	
48	235.0000	-2.3078	1.6160	-2.6050	0.6992	254.9745	
49	240.0000	-2.4399	1.4087	-2.9574	0.4376	261.5836	
50	245.0000	-2.5534	1.1907	-3.3197	0.2928	264.9598	
51	250.0000	-2.6474	0.9636	-3.5889	0.2039	266.7487	
52	255.0000	-2.7213	0.7292	-3.8092	0.1194	268.2051	
53	260.0000	-2.7745	0.4892	-3.9766	0.0653	269.0590	
54	265.0000	-2.8066	0.2455	-4.0860	0.0215	269.6985	
* 55	270.0929	-2.8173	-0.0046	-4.1346	0.0073	269.8982	* CHINE SEPARATION POINT
56	275.0000	-2.8066	-0.2455	-4.0882	-0.0081	270.1139	
57	280.0000	-2.7745	-0.4892	-3.9818	-0.0492	270.7082	
58	285.0000	-2.7213	-0.7292	-3.8111	-0.1037	271.5583	
59	290.0000	-2.6474	-0.9636	-3.5922	-0.1894	273.0186	
60	295.0000	-2.5534	-1.1907	-3.3070	-0.2760	274.7713	
61	300.0000	-2.4399	-1.4087	-2.9213	-0.4645	279.0352	

(p) Page 16

Figure 26.- Continued.

62	305.0000	-2.3078	-1.6160	-2.6145	-0.7925	286.8636
63	310.0000	-2.1582	-1.8109	-2.4222	-1.0637	293.7077
64	315.0000	-1.9922	-1.9922	-2.1966	-1.2609	299.8569
65	320.0000	-1.8109	-2.1582	-1.9444	-1.4610	306.9219
66	325.0000	-1.6160	-2.3078	-1.6883	-1.6557	314.4402
67	330.0000	-1.4087	-2.4399	-1.4430	-1.8514	322.0663
68	335.0000	-1.1907	-2.5534	-1.2267	-2.0108	328.6136
69	340.0000	-0.9636	-2.6474	-0.9977	-2.1180	334.7783
70	345.0000	-0.7292	-2.7213	-0.7498	-2.2057	341.2264
71	350.0000	-0.4892	-2.7745	-0.5041	-2.2729	347.4950
72	355.0000	-0.2455	-2.8066	-0.2571	-2.3071	353.6402
73	360.0000	0.0000	-2.8173	0.0000	-2.3152	0.0000

(q) Page 17

Figure 26.- Continued.

INPUT BODY GEOMETRY AT XFC(3) = 19.94000

XRC (Y)	YRC (Z)
0.0000	-2.6524
0.4606	-2.6121
0.9072	-2.4925
1.3262	-2.2971
2.4111	-1.2307
3.1590	-0.4827
4.3500	0.0000
3.1590	0.4827
1.3262	2.2971
0.9072	2.4925
0.4606	2.6121
0.0000	2.6524

BODY AXIS SHIFT, ZZ = 0.0002265

CIRCLE RADIUS, RZ = 3.0342150

MAPPED AND INPUT CORNER COORDINATES

	MAPPED...		INPUT...	
I	YRT	ZRT	YR	ZR
1	0.00000	-2.65137	0.00000	-2.65240
2	0.46035	-2.61169	0.46060	-2.61210
3	0.90681	-2.49268	0.90719	-2.49247
4	1.32411	-2.29426	1.32622	-2.29709
5	2.41363	-1.23347	2.41107	-1.23073
6	3.17855	-0.50470	3.15905	-0.48274
7	4.35134	-0.00256	4.35000	0.00000
8	3.19524	0.49184	3.15905	0.48274
9	1.32518	2.29484	1.32622	2.29709
10	0.90717	2.49336	0.90719	2.49247
11	0.45997	2.61268	0.46060	2.61210
12	0.00000	2.65240	0.00000	2.65240

(r) Page 18

Figure 26.- Continued.

***** ITERATION NO. 12 *****

SERIES COEFFICIENTS

N	AN
1	-0.2313311
2	-0.0004480
3	0.1544752
4	0.0002782
5	-0.0517554
6	-0.0000627
7	-0.0007065
8	0.0000508
9	0.0037163
10	0.0000468
11	-0.0030484
12	-0.0001696
13	0.0028445
14	0.0000606
15	0.0031767
16	0.0001042
17	-0.0038550
18	-0.0001290
19	0.0005987
20	0.0000396
21	0.0001602
22	0.0000740
23	-0.0011882
24	-0.0001046
25	0.0012832
26	0.0000243
27	0.0007353
28	0.0000586
29	-0.0011114
30	-0.0000674

(s) Page 19

Figure 26.- Continued.

CORRESPONDING POINTS ON BODY AND CIRCLE FOR CHINE FOR X = 19.94000

I	CIRCLE THETA	CIRCLE Y	CIRCLE Z	BODY Y	BODY Z	BODY BETA	
1	0.0000	0.0000	-3.0342	0.0000	-2.6514	0.0000	
2	5.0000	0.2644	-3.0227	0.2643	-2.6397	5.7167	
3	10.0000	0.5269	-2.9881	0.5253	-2.5990	11.4254	
4	15.0000	0.7853	-2.9308	0.7835	-2.5344	17.1781	
5	20.0000	1.0378	-2.8512	1.0327	-2.4424	22.9185	
6	25.0000	1.2823	-2.7499	1.2689	-2.3288	28.5861	
7	30.0000	1.5171	-2.6277	1.4728	-2.1879	34.1909	
8	35.0000	1.7404	-2.4855	1.6961	-1.9364	41.2152	
9	40.0000	1.9504	-2.3243	1.9525	-1.6937	49.0602	
10	45.0000	2.1455	-2.1455	2.2090	-1.4334	57.0207	
11	50.0000	2.3243	-1.9504	2.4875	-1.1645	64.9142	
12	55.0000	2.4855	-1.7404	2.7554	-0.8922	72.0585	
13	60.0000	2.6277	-1.5171	3.0670	-0.5858	79.1904	
14	65.0000	2.7499	-1.2823	3.4454	-0.3642	83.9663	
15	70.0000	2.8512	-1.0378	3.7572	-0.2466	86.2447	
16	75.0000	2.9308	-0.7853	3.9936	-0.1475	87.8854	
17	80.0000	2.9881	-0.5269	4.1786	-0.0735	88.9921	
18	85.0000	3.0227	-0.2644	4.3017	-0.0231	89.6927	
* 19	89.9833	3.0342	-0.0009	4.3513	-0.0026	89.9662	* CHINE SEPARATION POINT
20	95.0000	3.0227	0.2644	4.3007	0.0186	90.2479	
21	100.0000	2.9881	0.5269	4.1769	0.0688	90.9433	
22	105.0000	2.9308	0.7853	3.9908	0.1435	92.0599	
23	110.0000	2.8512	1.0378	3.7538	0.2423	93.6925	
24	115.0000	2.7499	1.2823	3.4381	0.3620	96.0100	
25	120.0000	2.6277	1.5171	3.0626	0.5893	100.8908	
26	125.0000	2.4855	1.7404	2.7559	0.8928	107.9508	
27	130.0000	2.3243	1.9504	2.4850	1.1628	115.0763	
28	135.0000	2.1455	2.1455	2.2059	1.4339	123.0251	
29	140.0000	1.9504	2.3243	1.9498	1.6948	130.9949	
30	145.0000	1.7404	2.4855	1.6939	1.9385	138.8526	
31	150.0000	1.5171	2.6277	1.4721	2.1699	145.8462	
32	155.0000	1.2823	2.7499	1.2688	2.3304	151.4374	
33	160.0000	1.0378	2.8512	1.0327	2.4436	157.0900	
34	165.0000	0.7853	2.9308	0.7832	2.5352	162.8333	
35	170.0000	0.5269	2.9881	0.5253	2.6000	168.5786	
36	175.0000	0.2644	3.0227	0.2641	2.6404	174.2877	
37	180.0000	0.0000	3.0342	0.0000	2.6524	180.0000	
38	185.0000	-0.2644	3.0227	-0.2641	2.6404	185.7123	
39	190.0000	-0.5269	2.9881	-0.5253	2.6000	191.4214	
40	195.0000	-0.7853	2.9308	-0.7832	2.5352	197.1667	
41	200.0000	-1.0378	2.8512	-1.0327	2.4436	202.9101	
42	205.0000	-1.2823	2.7499	-1.2688	2.3304	208.5626	
43	210.0000	-1.5171	2.6277	-1.4721	2.1699	214.1539	
44	215.0000	-1.7404	2.4855	-1.6939	1.9385	221.1475	
45	220.0000	-1.9504	2.3243	-1.9498	1.6948	229.0052	
46	225.0000	-2.1455	2.1455	-2.2059	1.4339	236.9749	
47	230.0000	-2.3243	1.9504	-2.4850	1.1628	244.9237	
48	235.0000	-2.4855	1.7404	-2.7559	0.8928	252.0493	
49	240.0000	-2.6277	1.5171	-3.0626	0.5893	259.1093	
50	245.0000	-2.7499	1.2823	-3.4381	0.3620	263.9901	
51	250.0000	-2.8512	1.0378	-3.7538	0.2423	266.3075	
52	255.0000	-2.9308	0.7853	-3.9908	0.1435	267.9401	
53	260.0000	-2.9881	0.5269	-4.1769	0.0688	269.0567	
54	265.0000	-3.0227	0.2644	-4.3007	0.0186	269.7521	
* 55	270.0167	-3.0342	-0.0009	-4.3513	-0.0026	270.0338	* CHINE SEPARATION POINT
56	275.0000	-3.0227	-0.2645	-4.3017	-0.0231	270.3073	
57	280.0000	-2.9881	-0.5269	-4.1786	-0.0735	271.0079	
58	285.0000	-2.9308	-0.7853	-3.9936	-0.1475	272.1147	
59	290.0000	-2.8512	-1.0378	-3.7572	-0.2466	273.7553	
60	295.0000	-2.7499	-1.2823	-3.4454	-0.3642	278.0337	
61	300.0000	-2.6277	-1.5171	-3.0670	-0.5858	280.8098	

(t) Page 20

Figure 26.- Continued.

62	305.0000	-2.4855	-1.7404	-2.7554	-0.8922	287.9416
63	310.0000	-2.3243	-1.9504	-2.4875	-1.1645	295.0858
64	315.0000	-2.1455	-2.1455	-2.2090	-1.4334	302.9794
65	320.0000	-1.9504	-2.3243	-1.9525	-1.6937	310.9398
66	325.0000	-1.7404	-2.4855	-1.6961	-1.9364	318.7849
67	330.0000	-1.5171	-2.6277	-1.4728	-2.1679	326.8091
68	335.0000	-1.2823	-2.7499	-1.2689	-2.3288	331.4139
69	340.0000	-1.0378	-2.8512	-1.0327	-2.4424	337.0815
70	345.0000	-0.7853	-2.9308	-0.7835	-2.5344	342.8219
71	350.0000	-0.5269	-2.9881	-0.5253	-2.5990	348.5746
72	355.0000	-0.2644	-3.0227	-0.2643	-2.6397	354.2834
73	360.0000	0.0000	-3.0342	0.0000	-2.6514	0.0000

(u) Page 21

Figure 26.- Continued.

```
          CALCULATED COEFFICIENTS FOR NUMERICAL MAPPING,  MNFC = 30     MXFC =  3

       XFC
      7.190

 BODY AXIS SHIFT, ZZ = 0.0313693

 CIRCLE RADIUS, RZ   = 1.9581980

       XRC (Y)
            0.00000E+00  2.65938E-01  5.44120E-01  8.32810E-01  1.64575E+00  1.98244E+00
            2.90258E+00  1.88626E+00  1.03457E+00  5.45313E-01  2.90037E-01 -8.83767E-08

       YRC (Y)
           -1.68264E+00 -1.65941E+00 -1.58802E+00 -1.47580E+00 -7.78818E-01 -3.41417E-01
           -1.73853E-02  3.16462E-01  1.03081E+00  1.51249E+00  1.72881E+00  1.83667E+00

       THC (RAD.)
            0.00000E+00  1.35886E-01  2.76273E-01  4.30621E-01  8.68877E-01  1.03771E+00
            1.58119E+00  2.17743E+00  2.51014E+00  2.76318E+00  2.93224E+00  3.14159E+00

       AFC
           -2.64626E-01 -1.72847E-02  1.91815E-01 -3.50858E-02 -3.34423E-02 -4.24022E-03
           -2.97731E-03  6.81383E-03  7.25260E-03 -4.37366E-03 -4.73047E-03 -4.75440E-04
           -3.62738E-04  5.29617E-03  6.25960E-03 -2.19430E-03 -2.58757E-03 -2.29141E-03
           -1.61599E-03  2.15777E-03  2.22853E-03 -1.32900E-03 -2.80265E-04 -2.25879E-03
           -8.17825E-04  1.45334E-03  1.90170E-03 -1.13097E-04  3.71434E-04 -1.42439E-03

       XFC
      13.560

 BODY AXIS SHIFT, ZZ =-0.0303943

 CIRCLE RADIUS, RZ   = 2.8173275

       XRC (Y)
            0.00000E+00  4.10966E-01  7.85907E-01  1.20788E+00  2.35721E+00  2.93405E+00
            4.13458E+00  2.89800E+00  1.15134E+00  7.97879E-01  3.97952E-01 -1.92761E-07

       YRC (Y)
           -2.31520E+00 -2.28988E+00 -2.19382E+00 -2.02176E+00 -1.12858E+00 -4.55311E-01
            7.34697E-03  4.71940E-01  2.03781E+00  2.29922E+00  2.51455E+00  2.59792E+00

       THC (RAD.)
            0.00000E+00  1.41308E-01  2.74484E-01  4.28731E-01  8.44968E-01  1.05009E+00
            1.56911E+00  2.10796E+00  2.66487E+00  2.80304E+00  2.96900E+00  3.14159E+00

       AFC
           -2.61149E-01 -2.08124E-02  1.68569E-01 -1.70018E-02 -4.05029E-02 -6.26841E-04
            2.76557E-03  2.64570E-03  6.10410E-03 -3.63772E-03 -6.61244E-03 -4.19219E-04
            9.76782E-04  2.66747E-03  5.52375E-03 -7.47092E-04 -4.19127E-03 -1.11723E-03
           -8.13256E-04  5.54568E-04  1.95691E-03 -5.03931E-04 -1.64074E-03 -5.20613E-04
           -3.26334E-04  3.21292E-04  1.76171E-03 -1.25529E-04 -8.74564E-04 -8.36085E-05
```


(v) Page 22

Figure 26.- Continued.

```
     XFC
   19.940

BODY AXIS SHIFT, ZZ = 0.0002265

CIRCLE RADIUS, RZ   = 3.0342150


      XRC (Y)
            0.00000E+00  4.60352E-01  9.06812E-01  1.32411E+00  2.41363E+00  3.17855E+00
            4.35134E+00  3.19524E+00  1.32518E+00  9.07167E-01  4.59968E-01 -2.66463E-07

      YRC (Y)
           -2.65137E+00 -2.61169E+00 -2.49268E+00 -2.29426E+00 -1.23347E+00 -5.04703E-01
           -2.56398E-03  4.91845E-01  2.29484E+00  2.49336E+00  2.61266E+00  2.65240E+00

      THC (RAD.)
            0.00000E+00  1.52870E-01  3.04753E-01  4.58858E-01  8.49708E-01  1.07326E+00
            1.57051E+00  2.06304E+00  2.68209E+00  2.83668E+00  2.98887E+00  3.14159E+00

      AFC
           -2.31331E-01 -4.48035E-04  1.54475E-01  2.78203E-04 -5.17554E-02 -6.27261E-05
           -7.06547E-04  5.07649E-05  3.71627E-03  4.68375E-05 -3.04841E-03 -1.69560E-04
            2.84450E-03  6.05755E-05  3.17672E-03  1.04184E-04 -3.85505E-03 -1.29021E-04
            5.98718E-04  3.96489E-05  1.60234E-04  7.40022E-05 -1.18822E-03 -1.04638E-04
            1.28322E-03  2.42539E-05  7.35292E-04  5.85512E-05 -1.11143E-03 -6.73980E-05
```


(w) Page 23

Figure 26.- Continued.

PARAMETERS FOR CHINE CROSS SECTION BODIES

VORTEX LATTICE APPROX. AT FIRST 8 STATIONS TO START THE CHINE SOLUTION
VORTEX LATTICE BOUNDARY CONDITION APPLIED AT 0.25000 OF THE EXPOSED STRAKE SPAN

CHINE SECTION BEGINS AT XCHNB = 0.00000
CHINE SECTION ENDS AT XCHNE = 30.00000

	NCIR	NBLSEP	VRF
X < XCHNB	3	1	1.00000
XCHNB < X < XCHNE	3		
XCHNB < X	3	1	1.00000

(x) Page 24

Figure 26.- Continued.

X	R	DR/DX	X/L	RETR
0.6000	0.1491	0.3031	0.0068	0.197E+06

BODY SURFACE PRESSURE DISTRIBUTION

J	Y	Z	BETA	U/V0	V/V0	W/V0	VT/V0	CP	DPHI/DT	VC/V0	WC/V0		CS
1	0.0000	-0.1281	0.000	0.5370	0.0000	-0.2373	0.2373	0.6553	0.0000	0.0000	-0.2392	0.992	0.000
2	0.0130	-0.1274	5.838	0.5399	0.0862	-0.2309	0.2465	0.6477	0.0000	0.0802	-0.2331	0.999	-0.026
3	0.0260	-0.1251	11.757	0.5458	0.1630	-0.1993	0.2575	0.6358	0.0000	0.1585	-0.2150	0.983	-0.048
4	0.0392	-0.1216	17.887	0.5565	0.2261	-0.1664	0.2807	0.6115	0.0000	0.2329	-0.1852	0.943	-0.035
5	0.0523	-0.1172	24.066	0.5690	0.2884	-0.1380	0.3197	0.5740	0.0000	0.3017	-0.1448	0.955	-0.001
6	0.0641	-0.1120	29.795	0.5847	0.3910	-0.0603	0.3956	0.5246	0.0000	0.3631	-0.0946	1.049	-0.107
7	0.0745	-0.1034	35.759	0.5868	0.3503	0.0531	0.3543	0.5302	0.0000	0.4158	-0.0362	0.825	-0.199
8	0.0870	-0.0924	43.271	0.6231	0.3453	0.0464	0.3484	0.4904	0.0000	0.4586	0.0291	0.756	-0.053
9	0.0999	-0.0815	50.788	0.6427	0.3692	0.0916	0.3804	0.4422	0.0000	0.4906	0.0994	0.759	-0.033
10	0.1133	-0.0695	58.450	0.6766	0.3775	0.0880	0.3876	0.3920	0.0000	0.5112	0.1729	0.715	0.070
11	0.1257	-0.0588	64.935	0.6709	0.4511	0.2023	0.4944	0.3055	0.0000	0.5201	0.2476	0.858	0.020
12	0.1354	-0.0433	72.249	0.7199	0.2805	0.1983	0.3435	0.3638	0.0000	0.5173	0.3218	0.563	-0.033
13	0.1534	-0.0243	81.010	0.7951	0.2962	0.0606	0.3023	0.2765	0.0000	0.5034	0.3934	0.424	0.211
14	0.1755	-0.0152	85.050	0.8687	0.4407	-0.0600	0.4447	0.0476	0.0000	0.4788	0.4608	0.415	0.525
15	0.1908	-0.0111	86.675	0.8800	0.6510	-0.0055	0.6510	-0.1982	0.0000	0.4446	0.5222	0.609	0.728
16	0.2030	-0.0068	88.093	0.9307	0.7822	-0.0473	0.7837	-0.4804	0.0000	0.4021	0.5763	0.582	0.951
17	0.2121	-0.0042	88.858	0.9692	1.2263	-0.0409	1.2269	-1.4448	0.0000	0.3526	0.6219	0.796	1.520
18	0.2181	-0.0021	89.456	1.0161	1.8548	-0.0336	1.8551	-3.4739	0.0000	0.2977	0.6580	1.016	2.359
19	0.2210	-0.0014	89.650	***** CHINE EDGE POINT *****									
20	0.2192	-0.0007	89.807	0.2340	-1.9091	1.4398	2.3912	-4.7724	0.0000	0.1789	0.6997	1.277	-3.055
21	0.2139	0.0009	90.252	0.5885	-1.0507	0.7862	1.3123	-1.0684	0.0000	0.1186	0.7050	0.841	-1.632
22	0.2057	0.0035	90.963	0.7306	-0.7267	0.5435	0.9074	-0.3572	0.0000	0.0601	0.7001	0.682	-1.098
23	0.1946	0.0068	92.013	0.8111	-0.5392	0.4192	0.6830	-0.1244	0.0000	0.0049	0.6858	0.606	-0.791
24	0.1810	0.0112	93.552	0.8623	-0.4365	0.3467	0.5575	-0.0544	0.0000	-0.0452	0.6630	0.565	-0.620
25	0.1641	0.0160	95.576	0.9190	-0.3230	0.2520	0.4097	-0.0124	0.0000	-0.0890	0.6326	0.461	-0.446
26	0.1425	0.0247	99.828	0.9441	-0.1890	0.2467	0.3108	0.0122	0.0000	-0.1254	0.5962	0.460	-0.220
27	0.1228	0.0397	107.941	0.9467	-0.1227	0.3002	0.3243	-0.0014	0.0000	-0.1536	0.5552	0.559	-0.066
28	0.1071	0.0541	116.795	0.9497	-0.1406	0.3120	0.3423	-0.0191	0.0000	-0.1729	0.5112	0.831	-0.062
29	0.0906	0.0675	126.682	0.9680	-0.1047	0.2817	0.3005	-0.0273	0.0000	-0.1831	0.4659	0.800	0.011
30	0.0753	0.0818	137.351	0.9761	-0.0763	0.2891	0.2990	-0.0421	0.0000	-0.1842	0.4210	0.843	0.100
31	0.0613	0.0953	147.259	0.9847	-0.0507	0.2809	0.2854	-0.0511	0.0000	-0.1766	0.3782	0.861	0.175
32	0.0490	0.1081	155.631	0.9890	-0.0244	0.3005	0.3015	-0.0691	0.0000	-0.1609	0.3390	0.751	0.285
33	0.0377	0.1184	162.339	0.9883	-0.0199	0.2921	0.2927	-0.0624	0.0000	-0.1380	0.3048	0.820	0.306
34	0.0273	0.1276	167.922	0.9970	0.0282	0.3174	0.3186	-0.0955	0.0000	-0.1091	0.2769	0.957	0.479
35	0.0184	0.1334	172.128	0.9688	-0.0301	0.3343	0.3357	-0.0512	0.0000	-0.0754	0.2562	1.233	0.246
36	0.0080	0.1371	176.644	0.9836	0.0439	0.2934	0.2967	-0.0555	0.0000	-0.0385	0.2435	1.148	0.362
37	0.0000	0.1398	180.000	0.9517	0.0000	0.4634	-0.4634	-0.1204	0.0000	0.0000	0.2392	1.937	0.000

INITIAL CHINE VORTEX LOCATION CONVERGED

NEW VORTICIES

+ Y NEW VORTEX	YG	ZG	BETA	GAM/V	0.22990	-0.00216	89.46152	0.05848
- Y NEW VORTEX	YG	ZG	BETA	GAM/V	-0.22990	-0.00216	270.53848	-0.05848

(y) Page 25

Figure 26.- Continued.

	R	DR/DX	X/L	RETR
0.E+00	0.1491	0.3031	0.0068	0.197E+05

BODY SURFACE PRESSURE DISTRIBUTION

J	Y	Z	BETA	U/V0	V/V0	W/V0	VT/V0	CP	DPHI/DT	VC/V0	WC/V0		CS
1	0.0000	-0.1281	0.000	0.5370	0.0000	-0.2373	0.2373	0.6553	0.0000	0.0000	-0.2392	0.992	0.000
2	0.0130	-0.1274	5.838	0.5399	0.0843	-0.2311	0.2460	0.6479	0.0000	0.0783	-0.2333	0.999	-0.026
3	0.0260	-0.1251	11.757	0.5458	0.1593	-0.2002	0.2558	0.6366	0.0000	0.1546	-0.2156	0.963	-0.048
4	0.0392	-0.1216	17.887	0.5565	0.2206	-0.1681	0.2773	0.6134	0.0000	0.2270	-0.1868	0.943	-0.035
5	0.0523	-0.1172	24.066	0.5690	0.2807	-0.1408	0.3141	0.5776	0.0000	0.2937	-0.1477	0.955	-0.001
6	0.0641	-0.1120	29.795	0.5847	0.3808	-0.0664	0.3865	0.5317	0.0000	0.3529	-0.0994	1.049	-0.107
7	0.0745	-0.1034	35.759	0.5868	0.3414	0.0446	0.3443	0.5372	0.0000	0.4032	-0.0434	0.825	-0.199
8	0.0870	-0.0924	43.271	0.6231	0.3344	0.0375	0.3365	0.4985	0.0000	0.4434	0.0184	0.758	-0.053
9	0.0999	-0.0815	50.788	0.6427	0.3580	0.0795	0.3647	0.4539	0.0000	0.4725	0.0842	0.759	-0.033
10	0.1133	-0.0695	58.450	0.6766	0.3607	0.0742	0.3682	0.4066	0.0000	0.4898	0.1515	0.715	0.070
11	0.1257	-0.0588	64.935	0.6709	0.4289	0.1770	0.4640	0.3346	0.0000	0.4949	0.2177	0.858	0.020
12	0.1354	-0.0433	72.249	0.7199	0.2652	0.1736	0.3170	0.3813	0.0000	0.4878	0.2795	0.563	-0.033
13	0.1534	-0.0243	81.010	0.7951	0.2687	0.0424	0.2720	0.2939	0.0000	0.4685	0.3330	0.424	0.211
14	0.1755	-0.0152	85.050	0.8687	0.3771	-0.0758	0.3845	0.0975	0.0000	0.4376	0.3723	0.415	0.525
15	0.1908	-0.0111	86.675	0.8800	0.5237	-0.0516	0.5262	-0.0513	0.0000	0.3958	0.3881	0.609	0.728
16	0.2030	-0.0068	88.093	0.9307	0.5471	-0.1167	0.5594	-0.1792	0.0000	0.3452	0.3640	0.582	0.951
17	0.2121	-0.0042	88.858	0.9692	0.6471	-0.2251	0.6851	-0.4087	0.0000	0.2911	0.2731	0.796	1.520
18	0.2181	-0.0021	89.456	1.0161	0.5030	-0.4808	0.6958	-0.5166	0.0000	0.2494	0.1058	1.018	2.359
19	0.2210	-0.0014	89.650	***** CHINE EDGE POINT *****									
20	0.2192	-0.0007	89.807	0.2340	-0.1643	0.8836	0.8988	0.1374	0.0000	0.2271	0.1487	1.277	-3.055
21	0.2139	0.0009	90.252	0.5885	-0.4316	0.5939	0.7342	0.1147	0.0000	0.1799	0.3572	0.841	-1.632
22	0.2057	0.0035	90.963	0.7306	-0.4558	0.4612	0.6485	0.0457	0.0000	0.1168	0.4884	0.682	-1.098
23	0.1946	0.0068	92.013	0.8111	-0.4040	0.3767	0.5524	0.0370	0.0000	0.0538	0.5521	0.606	-0.791
24	0.1810	0.0112	93.552	0.8623	-0.3585	0.3224	0.4822	0.0239	0.0000	-0.0040	0.5747	0.565	-0.620
25	0.1641	0.0160	95.576	0.9190	-0.2801	0.2398	0.3687	0.0195	0.0000	-0.0542	0.5724	0.461	-0.446
26	0.1425	0.0247	99.828	0.9441	-0.1661	0.2338	0.2868	0.0265	0.0000	-0.0959	0.5540	0.460	-0.220
27	0.1228	0.0397	107.941	0.9467	-0.1066	0.2851	0.3044	0.0111	0.0000	-0.1285	0.5252	0.559	-0.066
28	0.1071	0.0541	116.795	0.9497	-0.1258	0.2999	0.3252	-0.0077	0.0000	-0.1515	0.4898	0.631	-0.062
29	0.0906	0.0675	126.682	0.9680	-0.0940	0.2724	0.2882	-0.0200	0.0000	-0.1650	0.4507	0.600	0.011
30	0.0753	0.0818	137.351	0.9761	-0.0676	0.2808	0.2888	-0.0361	0.0000	-0.1690	0.4104	0.643	0.100
31	0.0613	0.0953	147.259	0.9847	-0.0437	0.2739	0.2774	-0.0465	0.0000	-0.1640	0.3709	0.661	0.175
32	0.0490	0.1081	155.631	0.9890	-0.0180	0.2940	0.2946	-0.0650	0.0000	-0.1507	0.3342	0.751	0.285
33	0.0377	0.1184	162.339	0.9883	-0.0143	0.2872	0.2876	-0.0594	0.0000	-0.1300	0.3019	0.820	0.306
34	0.0273	0.1276	167.922	0.9970	0.0331	0.3131	0.3148	-0.0931	0.0000	-0.1032	0.2753	0.957	0.479
35	0.0184	0.1334	172.128	0.9688	-0.0254	0.3325	0.3335	-0.0497	0.0000	-0.0718	0.2555	1.233	0.246
36	0.0080	0.1371	176.644	0.9836	0.0461	0.2925	0.2961	-0.0551	0.0000	-0.0366	0.2433	1.148	0.362
37	0.0000	0.1398	180.000	0.9517	0.0000	0.4634	-0.4634	-0.1204	0.0000	0.0000	0.2392	1.937	0.000

FORCE AND MOMENT COEFFICIENTS - PRESSURE INTEGRATION

X	CN(X)	CY(X)	CA(X)	CN	CY	CA	CM	CR	CSL	XCPN	XCPY
0.250	4.502E-03	8.030E-08	4.763E-03	8.844E-04	1.577E-08	9.356E-04	2.336E-03	4.165E-08	0.000E+00	0.025	0.024

(z) Page 26

Figure 26.- Continued.

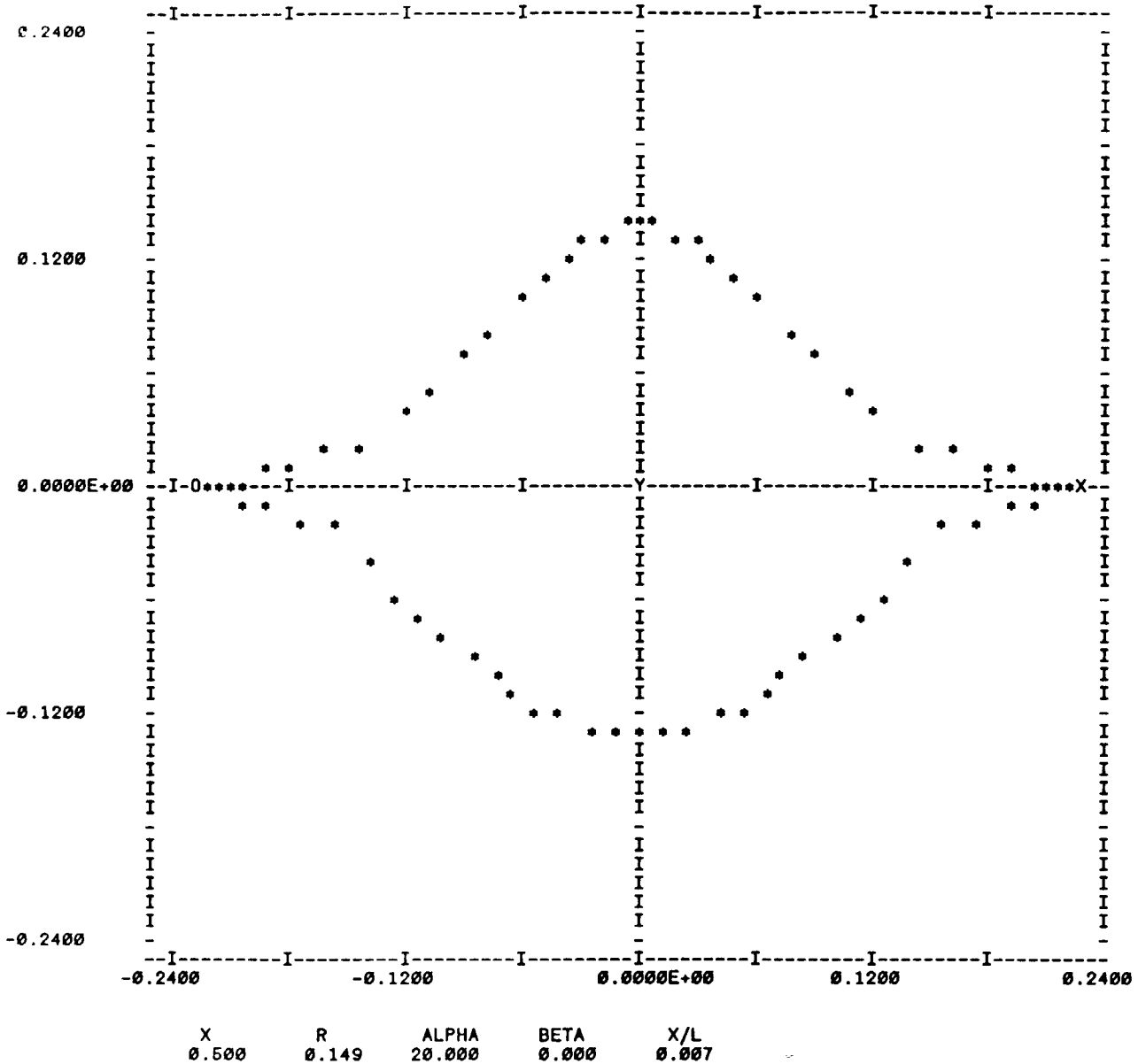

(aa) Page 27

Figure 26.- Continued.

```
 SUMMARY OF VORTEX FIELD AT X =  1.000      H = 0.50000

    NV     GAM/V        Y          Z        XSHED       BETA          YC         ZC         RG        RG/R

1    1   0.05848   0.22163   0.26375   0.50000   139.959        0.21782   0.32287   0.38948   1.30625

1    2  -0.05848  -0.22163   0.26375   0.50000   220.041       -0.21782   0.32287   0.38948   1.30625


CENTROID OF VORTICITY
                    GAM/V        Y         Z
          +Y BODY:   0.05848   0.22163   0.26375
          -Y BODY:  -0.05848  -0.22163   0.26375


INITIAL CHINE VORTEX LOCATION CONVERGED


NEW VORTICIES
+ Y NEW VORTEX   YG  ZG  BETA  GAM/V   0.45997  -0.00433  89.46095   0.11545
- Y NEW VORTEX   YG  ZG  BETA  GAM/V  -0.45997  -0.00433 270.53906  -0.11545
```


(ab) Page 28

Figure 26.- Continued.

SUMMARY OF VORTEX FIELD AT X = 4.500 H = 0.50000

	NV	GAM/V	Y	Z	XSHED	BETA	YC	ZC	RG	RG/R
1	1	0.05848	0.66070	0.65630	0.50000	134.809	0.73120	0.99780	1.23704	1.00860
2	2	0.11545	1.00635	0.56332	1.00000	119.239	0.95587	0.93566	1.33759	1.09059
3	3	0.16384	0.91023	0.58321	1.50000	122.649	0.89317	0.95440	1.30715	1.06577
4	4	0.19848	0.82175	0.76838	2.00000	133.078	0.83420	1.08155	1.36588	1.11366
5	5	0.22783	1.05333	0.84977	2.50000	128.895	1.00670	1.13921	1.52028	1.23954
6	6	0.25157	1.32373	0.80021	3.00000	121.153	1.21534	1.07686	1.62379	1.32394
7	7	0.27052	1.57912	0.61365	3.50000	111.236	1.39324	0.87554	1.64551	1.34164
8	8	0.29140	1.78435	0.36005	4.00000	101.408	1.50229	0.57708	1.60931	1.31214
1	9	-0.05848	-0.66070	0.65630	0.50000	225.191	-0.73120	0.99780	1.23704	1.00860
2	10	-0.11545	-1.00635	0.56332	1.00000	240.761	-0.95587	0.93566	1.33759	1.09059
3	11	-0.16384	-0.91023	0.58321	1.50000	237.351	-0.89317	0.95440	1.30715	1.06577
4	12	-0.19848	-0.82175	0.76838	2.00000	226.922	-0.83420	1.08155	1.36588	1.11366
5	13	-0.22783	-1.05333	0.84977	2.50000	231.105	-1.00670	1.13921	1.52028	1.23954
6	14	-0.25157	-1.32373	0.80021	3.00000	238.847	-1.21534	1.07686	1.62379	1.32393
7	15	-0.27052	-1.57912	0.61365	3.50000	248.764	-1.39324	0.87554	1.64551	1.34164
8	16	-0.29140	-1.78435	0.36005	4.00000	258.592	-1.50229	0.57708	1.60931	1.31214

CENTROID OF VORTICITY

	GAM/V	Y	Z
+Y BODY:	1.57757	1.25965	0.64486
-Y BODY:	-1.57757	-1.25965	0.64486

NEW VORTICIES

+ Y NEW VORTEX	YG	ZG	BETA	GAM/V	1.95473	0.02371	90.69500	0.50660
- Y NEW VORTEX	YG	ZG	BETA	GAM/V	-1.95473	0.02371	269.30499	-0.50660

Figure 26.- Continued.

X	R	DR/DX	X/L	RETR
4.5000	1.2265	0.2367	0.0613	0.177E+06

BODY SURFACE PRESSURE DISTRIBUTION

J	Y	Z	BETA	U/V0	V/V0	W/V0	VT/V0	CP	DPHI/DT	VC/V0	WC/V0		CS
1	0.0000	-1.0539	0.000	0.7223	0.0000	-0.2010	-0.2010	0.4330	0.0049	0.0000	-0.2026	0.992	0.000
2	0.1072	-1.0483	5.838	0.7247	0.0772	-0.1951	0.2098	0.4258	0.0050	0.0721	-0.1971	0.999	-0.026
3	0.2143	-1.0294	11.757	0.7294	0.1457	-0.1871	0.2217	0.4137	0.0052	0.1423	-0.1807	0.983	-0.048
4	0.3228	-1.0003	17.887	0.7372	0.2020	-0.1377	0.2445	0.3913	0.0055	0.2086	-0.1539	0.943	-0.035
5	0.4304	-0.9638	24.066	0.7460	0.2573	-0.1121	0.2807	0.3588	0.0059	0.2692	-0.1176	0.955	-0.001
6	0.5274	-0.9210	29.795	0.7440	0.3461	-0.0422	0.3486	0.3183	0.0065	0.3225	-0.0732	1.049	-0.107
7	0.6128	-0.8510	35.759	0.7629	0.3073	0.0550	0.3122	0.3131	0.0073	0.3671	-0.0220	0.825	-0.199
8	0.7156	-0.7602	43.271	0.7883	0.3020	0.0470	0.3057	0.2767	0.0084	0.4017	0.0339	0.756	-0.053
9	0.8220	-0.6707	50.788	0.8027	0.3200	0.0843	0.3310	0.2364	0.0098	0.4255	0.0926	0.759	-0.033
10	0.9318	-0.5721	58.450	0.8269	0.3238	0.0777	0.3328	0.1940	0.0115	0.4379	0.1514	0.715	0.070
11	1.0344	-0.4838	64.935	0.8220	0.3805	0.1695	0.4165	0.1369	0.0139	0.4387	0.2078	0.858	0.020
12	1.1138	-0.3586	72.249	0.8623	0.2322	0.1593	0.2816	0.1602	0.0169	0.4279	0.2578	0.563	-0.033
13	1.2819	-0.1998	81.010	0.9163	0.2348	0.0407	0.2383	0.0825	0.0211	0.4060	0.2980	0.424	0.211
14	1.4442	-0.1251	85.050	0.9659	0.3250	-0.0622	0.3309	-0.0692	0.0267	0.3742	0.3231	0.415	0.525
15	1.5694	-0.0912	86.675	0.9872	0.4409	-0.0447	0.4432	-0.1664	0.0345	0.3343	0.3260	0.609	0.728
16	1.6697	-0.0556	88.093	1.0002	0.4514	-0.1024	0.4629	-0.2604	0.0457	0.2895	0.2975	0.582	0.951
17	1.7452	-0.0348	88.858	1.0124	0.5413	-0.1928	0.5746	-0.4172	0.0621	0.2458	0.2273	0.798	1.520
18	1.7945	-0.0171	89.458	1.0234	0.4892	-0.3864	0.6234	-0.5229	0.0869	0.2135	0.1154	1.016	2.359
19	1.8178	-0.0111	89.650	***** CHINE EDGE POINT *****									
20	1.8030	-0.0061	89.807	0.5802	0.4232	0.5892	-0.7093	-0.0266	0.1869	0.2079	-0.0517	1.277	-3.055
21	1.7598	0.0077	90.252	0.8136	0.2489	0.3122	-0.3992	-0.1037	0.2823	0.2133	-0.0427	0.841	-1.632
22	1.6920	0.0285	90.963	0.9080	0.1978	0.2134	-0.2910	-0.3255	0.4163	0.2212	-0.0428	0.682	-1.098
23	1.6009	0.0563	92.013	0.9814	0.2011	0.1483	-0.2499	-0.5467	0.5601	0.2410	-0.0698	0.606	-0.791
24	1.4888	0.0924	93.552	0.9958	0.2154	0.1108	-0.2422	-0.7053	0.6550	0.2705	-0.1007	0.565	-0.620
25	1.3501	0.1318	95.576	1.0341	0.2058	0.0762	-0.2195	-0.7994	0.6819	0.3134	-0.1376	0.461	-0.446
26	1.1725	0.2031	99.828	1.0480	0.2256	-0.0086	-0.2258	-0.8070	0.6578	0.3917	-0.2061	0.460	-0.220
27	1.0099	0.3270	107.941	1.0469	0.3365	-0.1599	-0.3726	-0.8052	0.5704	0.5602	-0.3524	0.559	-0.066
28	0.8808	0.4448	116.795	1.0487	0.5355	-0.2739	-0.6015	-1.0033	0.5417	0.7983	-0.5118	0.631	-0.062
29	0.7454	0.5553	126.682	1.0607	0.5015	-0.2757	-0.5723	-0.7713	0.3187	0.8438	-0.4435	0.600	0.011
30	0.6197	0.6728	137.351	1.0649	0.3808	-0.1830	-0.4225	-0.5554	0.2430	0.6215	-0.1878	0.643	0.100
31	0.5041	0.7839	147.259	1.0695	0.2261	-0.0292	-0.2279	-0.3589	0.1630	0.3305	0.0432	0.681	0.175
32	0.4027	0.8891	155.631	1.0704	0.1600	0.0691	-0.1742	-0.3212	0.1462	0.1557	0.1510	0.751	0.285
33	0.3102	0.9743	162.339	1.0688	0.1147	0.1351	0.1773	-0.3058	0.1321	0.0689	0.1906	0.820	0.306
34	0.2247	1.0500	167.922	1.0719	0.1221	0.1817	0.2189	-0.3198	0.1228	0.0261	0.2028	0.957	0.479
35	0.1517	1.0972	172.128	1.0540	0.0587	0.2504	0.2572	-0.2936	0.1165	0.0069	0.2045	1.233	0.246
36	0.0861	1.1279	176.644	1.0635	0.0743	0.2332	0.2447	-0.3039	0.1130	0.0008	0.2033	1.148	0.362
37	0.0000	1.1504	180.000	1.0481	0.0000	0.3925	-0.3925	-0.3603	0.1118	0.0000	0.2026	1.937	0.000

FORCE AND MOMENT COEFFICIENTS - PRESSURE INTEGRATION

X	CN(X)	CY(X)	CA(X)	CN	CY	CA	CM	CR	CSL	XCPN	XCPY
4.250	2.549E-01	1.509E-06	-8.584E-02	2.028E-01	1.635E-06	-7.279E-02	4.622E-01	3.782E-06	-1.718E-07	3.175	43.119

(ad) Page 51

Figure 26.- Continued.

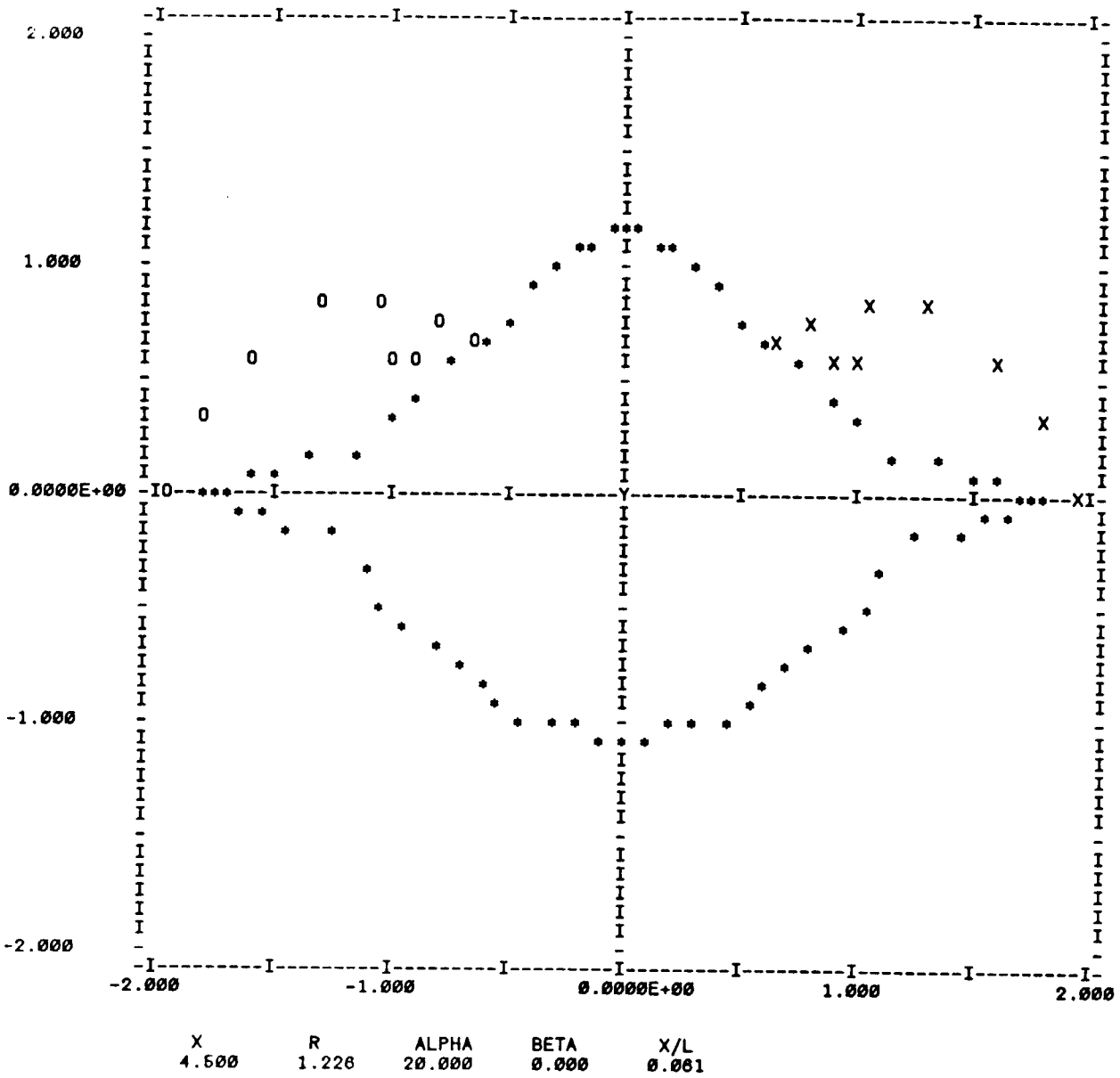

(ae) Page 52

Figure 26.- Continued.

SUMMARY OF VORTEX FIELD AT X = 5.000 H = 0.50000

	NV	GAM/V	Y	Z	XSHED	BETA	YC	ZC	RG	RG/R
1	1	0.05848	1.13254	0.35516	0.50000	107.411	1.04265	0.85815	1.35038	1.00745
2	2	0.11545	1.20154	0.59281	1.00000	116.260	1.11075	0.99779	1.49310	1.11392
3	3	0.16384	1.16519	0.51811	1.50000	113.973	1.07863	0.95273	1.43914	1.07367
4	4	0.19848	0.98309	0.61758	2.00000	122.137	0.96767	1.03055	1.41365	1.05465
5	5	0.22783	1.00807	0.83083	2.50000	129.495	0.99048	1.17616	1.53766	1.14717
6	6	0.25157	1.23543	0.93560	3.00000	127.137	1.16608	1.24578	1.70638	1.27304
7	7	0.27052	1.54124	0.80401	3.50000	117.549	1.39494	1.10579	1.78006	1.32801
8	8	0.29140	1.78947	0.56903	4.00000	107.640	1.55121	0.85121	1.76941	1.32006
9	9	0.50660	2.08128	0.38074	4.50000	100.465	1.75486	0.57591	1.84694	1.37791
1	10	-0.05848	-1.13254	0.35516	0.50000	252.589	-1.04265	0.85815	1.35038	1.00745
2	11	-0.11545	-1.20154	0.59281	1.00000	243.740	-1.11075	0.99779	1.49310	1.11392
3	12	-0.16384	-1.16519	0.51811	1.50000	246.027	-1.07863	0.95273	1.43914	1.07367
4	13	-0.19848	-0.98309	0.61758	2.00000	237.863	-0.96767	1.03055	1.41365	1.05465
5	14	-0.22783	-1.00807	0.83083	2.50000	230.505	-0.99048	1.17616	1.53766	1.14717
6	15	-0.25157	-1.23543	0.93560	3.00000	232.863	-1.16608	1.24578	1.70638	1.27304
7	16	-0.27052	-1.54124	0.80401	3.50000	242.451	-1.39494	1.10579	1.78006	1.32801
8	17	-0.29140	-1.78947	0.56903	4.00000	252.360	-1.55121	0.85121	1.76941	1.32006
9	18	-0.50660	-2.08128	0.38074	4.50000	259.535	-1.75486	0.57591	1.84694	1.37791

CENTROID OF VORTICITY

	GAM/V	Y	Z
+Y BODY:	2.08417	1.49415	0.62256
-Y BODY:	-2.08417	-1.49415	0.62256

NEW VORTICIES

+ Y NEW VORTEX	YG	ZG	BETA	GAM/V	2.10588	0.01818	90.49451	0.37719
- Y NEW VORTEX	YG	ZG	BETA	GAM/V	-2.10588	0.01818	269.50549	-0.37719

(af) Page 53

Figure 26.- Continued.

SUMMARY OF VORTEX FIELD AT X = 14.500 H = 0.50000

	NV	GAM/V	Y	Z	XSHED	BETA	YC	ZC	RG	RG/R
1	1	0.05848	3.18371	1.37409	0.50000	113.345	2.82745	1.95821	3.43934	1.22666
2	2	0.11545	3.51723	1.72855	1.00000	116.172	3.17226	2.19492	3.85758	1.37583
3	3	0.16384	3.56193	1.47210	1.50000	112.455	3.16268	1.96228	3.72198	1.32747
4	4	0.19848	3.58448	1.25097	2.00000	109.239	3.13038	1.76539	3.59387	1.28178
5	5	0.22783	3.37725	1.46663	2.50000	113.474	3.00381	1.99571	3.60634	1.28623
6	6	0.25157	3.87036	1.18917	3.00000	107.080	3.36963	1.63237	3.74421	1.33540
7	7	0.27052	4.05336	0.75858	3.50000	100.600	3.40164	1.15075	3.59102	1.28076
8	8	0.29140	2.93691	1.46358	4.00000	116.489	2.64910	2.07036	3.36216	1.19914
9	9	0.50660	3.68245	0.61135	4.50000	99.426	2.98085	1.18400	3.20738	1.14393
10	10	0.37719	3.43952	1.13237	5.00000	108.223	2.97694	1.70453	3.43039	1.22347
11	11	0.37449	3.20890	1.90286	5.50000	120.668	2.93180	2.39130	3.78336	1.34936
12	12	0.35477	3.51258	2.06614	6.00000	120.464	3.21822	2.49466	4.07189	1.45227
13	13	0.33017	3.94751	1.91797	6.50000	116.914	3.59445	2.29653	4.26546	1.52131
14	14	0.30557	4.17898	1.60161	7.00000	110.970	3.76019	1.95491	4.23801	1.51151
15	15	0.26109	4.21287	1.32387	7.50000	107.445	3.73528	1.67481	4.09357	1.46000
16	16	0.22419	4.29347	1.14340	8.00000	104.912	3.77328	1.47262	4.05047	1.44463
17	17	0.17181	4.08191	0.90379	8.50000	102.485	3.48528	1.28917	3.71607	1.32536
18	18	0.15995	2.71980	1.22416	9.00000	114.232	2.45325	1.92323	3.11725	1.11179
19	19	0.20440	3.00098	1.19978	9.50000	111.791	2.65330	1.85953	3.24004	1.15558
20	20	0.19416	2.67570	1.88157	10.00000	125.115	2.48867	2.42886	3.47747	1.24026
21	21	0.16678	2.92557	2.09644	10.50000	125.625	2.71234	2.58562	3.74729	1.33650
22	22	0.12893	3.40431	2.45018	11.00000	125.744	3.16340	2.85125	4.25873	1.51890
23	23	0.13876	3.92630	2.31263	11.50000	120.498	3.62822	2.66908	4.50422	1.60646
24	24	0.14421	4.38948	1.99181	12.00000	114.407	4.02951	2.30146	4.64044	1.65504
25	25	0.13867	4.67265	1.50441	12.50000	107.847	4.23872	1.76854	4.59287	1.63808
26	26	0.13892	4.73480	0.98494	13.00000	101.751	4.21200	1.20304	4.38044	1.56231
27	27	0.14321	4.64309	0.55599	13.50000	96.828	4.01776	0.72392	4.08245	1.45603
28	28	0.13217	4.44469	0.23566	14.00000	93.035	3.68116	0.34685	3.69747	1.31873
1	29	-0.05848	-3.18371	1.37409	0.50000	246.655	-2.82745	1.95821	3.43934	1.22666
2	30	-0.11545	-3.51723	1.72855	1.00000	243.828	-3.17226	2.19492	3.85758	1.37583
3	31	-0.16384	-3.56193	1.47210	1.50000	247.545	-3.16268	1.96228	3.72198	1.32747
4	32	-0.19848	-3.58448	1.25097	2.00000	250.761	-3.13038	1.76539	3.59387	1.28178
5	33	-0.22783	-3.37725	1.46663	2.50000	246.526	-3.00381	1.99571	3.60634	1.28623
6	34	-0.25157	-3.87036	1.18917	3.00000	252.920	-3.36963	1.63237	3.74421	1.33540
7	35	-0.27052	-4.05336	0.75858	3.50000	259.400	-3.40164	1.15075	3.59102	1.28076
8	36	-0.29140	-2.93691	1.46358	4.00000	243.511	-2.64910	2.07036	3.36216	1.19914
9	37	-0.50660	-3.68245	0.61135	4.50000	260.574	-2.98085	1.18400	3.20738	1.14393
10	38	-0.37719	-3.43952	1.13237	5.00000	251.777	-2.97694	1.70453	3.43039	1.22347
11	39	-0.37449	-3.20890	1.90286	5.50000	239.332	-2.93180	2.39130	3.78336	1.34936
12	40	-0.35477	-3.51258	2.06614	6.00000	239.536	-3.21822	2.49466	4.07189	1.45227
13	41	-0.33017	-3.94751	1.91797	6.50000	244.086	-3.59445	2.29653	4.26546	1.52131
14	42	-0.30557	-4.17898	1.60161	7.00000	249.030	-3.76019	1.95491	4.23801	1.51151
15	43	-0.26109	-4.21287	1.32387	7.50000	252.555	-3.73528	1.67481	4.09357	1.46000
16	44	-0.22419	-4.29347	1.14340	8.00000	255.088	-3.77328	1.47262	4.05047	1.44463
17	45	-0.17181	-4.08191	0.90379	8.50000	257.515	-3.48528	1.28917	3.71607	1.32536
18	46	-0.15995	-2.71980	1.22416	9.00000	245.768	-2.45325	1.92323	3.11725	1.11179
19	47	-0.20440	-3.00098	1.19978	9.50000	248.209	-2.65330	1.85953	3.24004	1.15558
20	48	-0.19416	-2.67570	1.88157	10.00000	234.885	-2.48867	2.42886	3.47747	1.24026
21	49	-0.16678	-2.92557	2.09644	10.50000	234.375	-2.71234	2.58562	3.74729	1.33650
22	50	-0.12893	-3.40431	2.45018	11.00000	234.256	-3.16340	2.85125	4.25873	1.51890
23	51	-0.13876	-3.92630	2.31263	11.50000	239.502	-3.62822	2.66908	4.50422	1.60646
24	52	-0.14421	-4.38948	1.99181	12.00000	245.593	-4.02951	2.30146	4.64044	1.65504
25	53	-0.13867	-4.67265	1.50441	12.50000	252.153	-4.23872	1.76854	4.59287	1.63808
26	54	-0.13892	-4.73480	0.98494	13.00000	258.249	-4.21200	1.20304	4.38044	1.56231
27	55	-0.14321	-4.64309	0.55599	13.50000	263.172	-4.01776	0.72392	4.08245	1.45603
28	56	-0.13217	-4.44469	0.23566	14.00000	266.965	-3.68116	0.34685	3.69747	1.31873

(ag) Page 114

Figure 26.- Continued.

CENTROID OF VORTICITY

	GAM/V	Y	Z
+Y BODY:	6.17360	3.68800	1.39838
-Y BODY:	-6.17360	-3.68800	1.39838

NEW VORTICIES

+ Y NEW VORTEX	YG	ZG	BETA	GAM/V	4.20361	0.04155	90.56638	0.11742
- Y NEW VORTEX	YG	ZG	BETA	GAM/V	-4.20361	0.04155	269.43362	-0.11742

(ah) Page 115

Figure 26.- Continued.

X	R	DR/DX	X/L	RETR
14.5000	2.8038	0.0814	0.1975	0.570E+06

BODY SURFACE PRESSURE DISTRIBUTION

J	Y	Z	BETA	U/V0	V/V0	W/V0	VT/V0	CP	DPHI/DT	VC/V0	WC/V0		CS
1	0.0000	-2.3255	0.000	0.9119	0.0000	-0.0429	0.0429	0.1992	-0.0326	0.0000	-0.0451	0.952	0.000
2	0.2542	-2.3170	6.260	0.9131	0.0546	-0.0400	0.0677	0.1944	-0.0326	0.0562	-0.0403	0.978	0.010
3	0.4993	-2.2824	12.339	0.9144	0.1100	-0.0224	0.1122	0.1841	-0.0328	0.1107	-0.0262	0.986	-0.032
4	0.7429	-2.2166	18.528	0.9167	0.1534	0.0043	0.1534	0.1692	-0.0330	0.1615	-0.0034	0.949	-0.048
5	0.9872	-2.1297	24.869	0.9192	0.1962	0.0308	0.1986	0.1491	-0.0334	0.2070	0.0274	0.951	-0.023
6	1.2137	-2.0232	30.960	0.9209	0.2354	0.0880	0.2514	0.1226	-0.0338	0.2458	0.0649	0.984	-0.098
7	1.4250	-1.8661	37.367	0.9271	0.2146	0.1316	0.2517	0.1114	-0.0344	0.2765	0.1078	0.835	-0.151
8	1.6636	-1.6685	44.916	0.9337	0.2195	0.1297	0.2550	0.0981	-0.0350	0.2981	0.1537	0.759	-0.044
9	1.9158	-1.4703	52.495	0.9382	0.2397	0.1496	0.2825	0.0757	-0.0356	0.3100	0.2013	0.764	0.014
10	2.1648	-1.2650	59.699	0.9430	0.2545	0.1651	0.3033	0.0550	-0.0363	0.3116	0.2479	0.758	0.074
11	2.3941	-1.0610	66.098	0.9442	0.2611	0.2259	0.3453	0.0263	-0.0370	0.3030	0.2910	0.821	0.043
12	2.5938	-0.7939	72.982	0.9557	0.1791	0.2031	0.2708	0.0508	-0.0375	0.2845	0.3278	0.624	0.005
13	2.8965	-0.4738	80.710	0.9701	0.1979	0.1178	0.2303	0.0434	-0.0376	0.2570	0.3551	0.482	0.208
14	3.2753	-0.2837	85.050	0.9813	0.2839	0.0605	0.2903	-0.0102	-0.0370	0.2218	0.3690	0.460	0.493
15	3.5598	-0.1942	86.877	0.9789	0.3831	0.0954	0.3948	-0.0791	-0.0361	0.1808	0.3650	0.628	0.739
16	3.7778	-0.1079	88.363	0.9809	0.4041	0.0936	0.4148	-0.1038	-0.0305	0.1368	0.3364	0.658	0.934
17	3.9477	-0.0517	89.250	0.9761	0.4905	0.0840	0.4976	-0.1792	-0.0212	0.0940	0.2737	0.825	1.508
18	4.0548	-0.0099	89.860	0.9480	0.4739	0.0557	0.4772	-0.1224	-0.0039	0.0595	0.1628	1.241	2.458
19	4.1009	0.0060	90.085	***** CHINE EDGE POINT *****									
20	4.0528	0.0209	90.295	0.9402	0.4407	-0.0387	-0.4424	-0.1359	0.0563	0.0589	-0.1564	1.146	-2.386
21	3.9432	0.0649	90.943	0.9773	0.6229	-0.1448	-0.6396	-0.4351	0.0710	0.1087	-0.3567	0.858	-1.485
22	3.7757	0.1210	91.835	1.0008	0.7699	-0.2149	-0.7993	-0.6793	0.0389	0.2222	-0.6551	0.652	-0.954
23	3.5565	0.2061	93.317	1.0086	0.9822	-0.3360	-1.0381	-1.0999	0.0050	0.4098	-0.9942	0.637	-0.725
24	3.2851	0.2979	95.181	1.0221	0.9091	-0.2579	-0.9449	-1.1554	0.2178	0.5875	-1.1534	0.498	-0.535
25	2.9266	0.4517	98.773	1.0241	0.6867	-0.3704	-0.7802	-1.0664	0.4089	0.7293	-1.1730	0.490	-0.281
26	2.5857	0.7150	105.458	1.0220	0.6240	-0.5560	-0.8358	-1.1034	0.3604	0.8425	-1.1248	0.583	-0.118
27	2.3105	0.9821	113.028	1.0221	0.6123	-0.5267	-0.8077	-0.9528	0.2558	0.8117	-0.8972	0.662	-0.083
28	2.0366	1.2291	121.111	1.0248	0.4362	-0.3586	-0.5647	-0.6244	0.2552	0.6364	-0.5727	0.659	-0.029
29	1.7726	1.4774	129.809	1.0256	0.2967	-0.2368	-0.3796	-0.4312	0.2352	0.4447	-0.3143	0.696	0.041
30	1.5198	1.7100	138.371	1.0265	0.1928	-0.1315	-0.2333	-0.3174	0.2093	0.2873	-0.1461	0.718	0.092
31	1.2810	1.9314	146.446	1.0261	0.1255	-0.0677	-0.1426	-0.2621	0.1888	0.1727	-0.0477	0.776	0.178
32	1.0627	2.1184	153.359	1.0247	0.0845	-0.0132	-0.0855	-0.2310	0.1736	0.0953	0.0053	0.876	0.187
33	0.8405	2.2688	159.673	1.0248	0.0481	0.0192	-0.0518	-0.2153	0.1624	0.0464	0.0311	0.907	0.194
34	0.6229	2.3961	165.429	1.0240	0.0277	0.0377	-0.0468	-0.2050	0.1543	0.0183	0.0418	1.001	0.225
35	0.4131	2.4865	170.567	1.0234	0.0125	0.0481	0.0497	-0.1987	0.1489	0.0046	0.0449	1.087	0.167
36	0.2026	2.5433	175.445	1.0234	0.0060	0.0519	0.0522	-0.1959	0.1458	0.0001	0.0452	1.148	0.130
37	0.0000	2.5658	180.000	1.0233	0.0000	0.0553	-0.0553	-0.1950	0.1448	0.0000	0.0451	1.227	0.000

FORCE AND MOMENT COEFFICIENTS - PRESSURE INTEGRATION

X	CN(X)	CY(X)	CA(X)	CN	CY	CA	CM	CR	CSL	XCPN	XCPY
14.250	6.327E-01	3.021E-06	-8.253E-02	2.327E+00	3.023E-05	-5.967E-01	3.634E+00	4.173E-05	-3.135E-07	9.414	35.009

(ai) Page 116

Figure 26.- Continued.

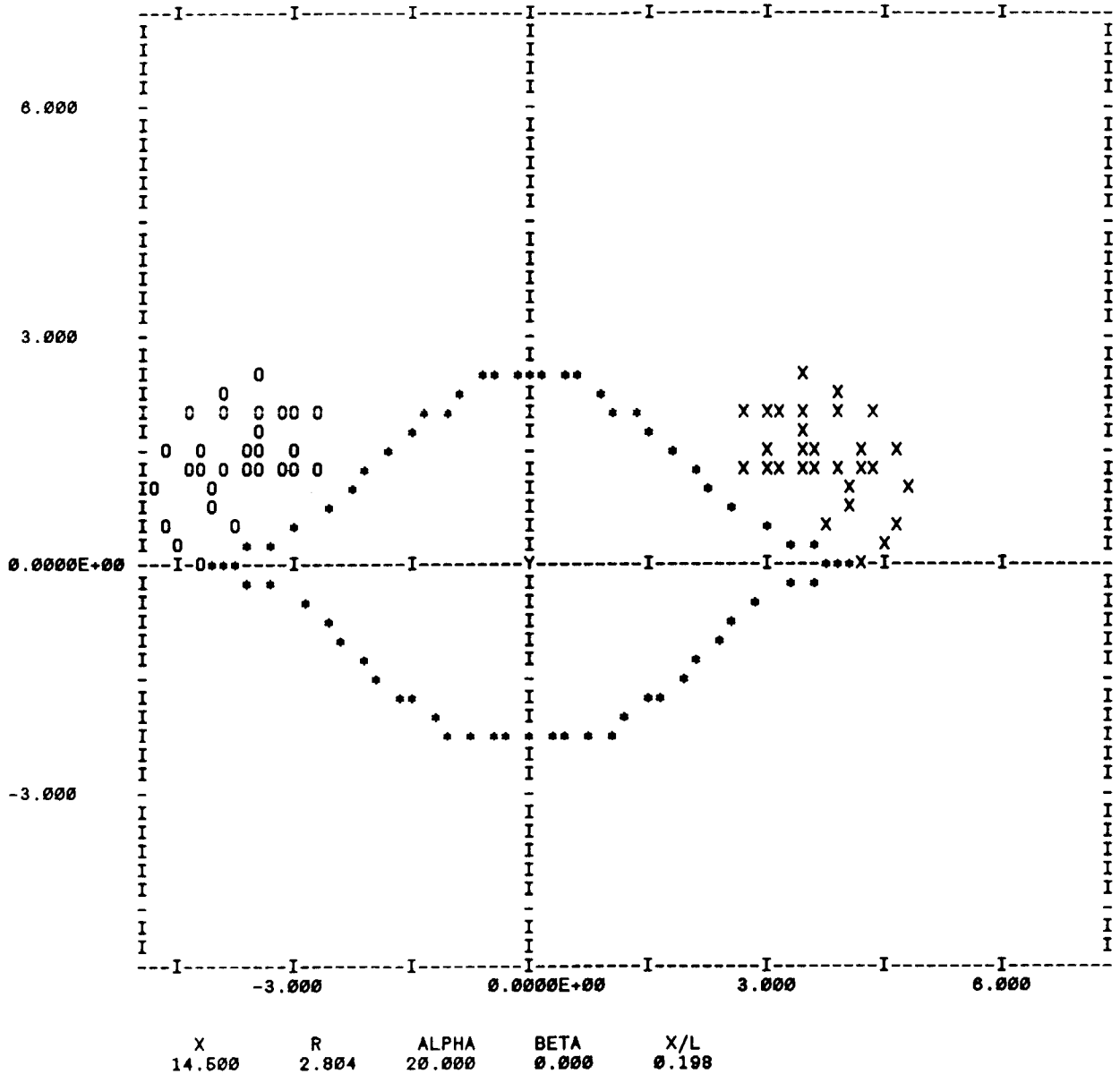

(aj) Page 117

Figure 26.- Continued.

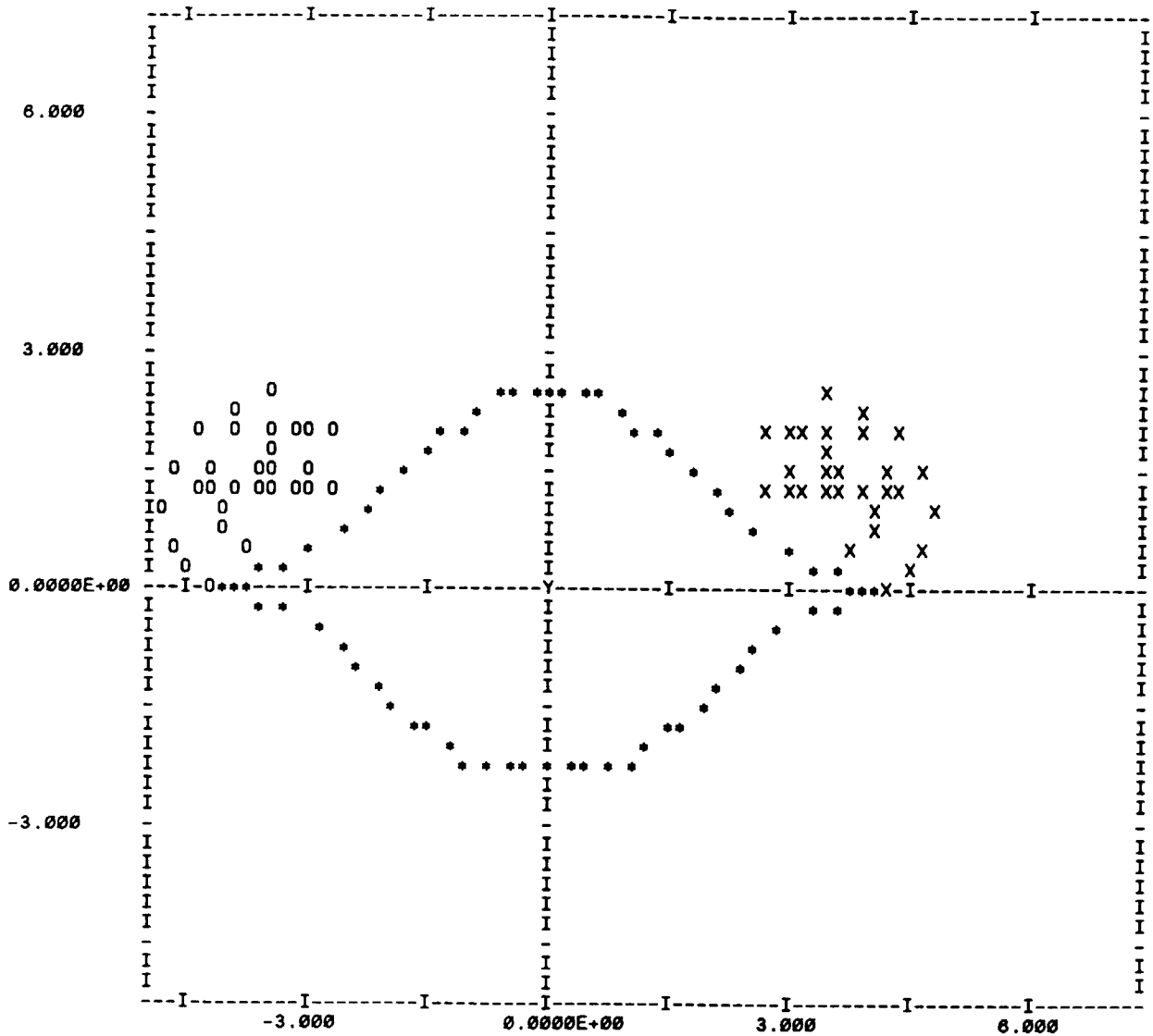

TOTAL FORCE AND MOMENT SUMMARY

X	ALPHA	BETA	CN	CY	CA	CDI	CM	CR	CSL
14.50	20.0000	0.0000	2.3272	0.0000	-0.5967	0.0000	3.6341	0.0000	0.0000

(ak) Page 118

Figure 26.- Continued.

PRESSURE DISTRIBUTION AT FINAL X STATION

Y	Z	CP
0.00000	-2.32548	0.19919
0.25418	-2.31701	0.19436
0.49928	-2.28245	0.18408
0.74289	-2.21663	0.16916
0.98718	-2.12973	0.14908
1.21374	-2.02323	0.12263
1.42502	-1.86607	0.11143
1.66360	-1.66847	0.09813
1.91578	-1.47027	0.07567
2.16476	-1.26502	0.05497
2.39407	-1.06101	0.02629
2.59378	-0.79388	0.05081
2.89655	-0.47380	0.04344
3.27533	-0.28369	-0.01024
3.55982	-0.19420	-0.07905
3.77776	-0.10794	-0.10377
3.94774	-0.05165	-0.17925
4.05477	-0.00992	-0.12241
4.10094	0.00605	-20.25622
4.05280	0.02090	-0.13593
3.94317	0.06491	-0.43514
3.77572	0.12096	-0.67930
3.55855	0.20611	-1.09992
3.28510	0.29785	-1.15542
2.92856	0.45167	-1.06845
2.58570	0.71503	-1.10344
2.31048	0.98208	-0.95261
2.03859	1.22908	-0.62444
1.77261	1.47738	-0.43117
1.51977	1.71002	-0.31740
1.28100	1.93144	-0.26213
1.06269	2.11838	-0.23099
0.84048	2.26883	-0.21526
0.62286	2.39615	-0.20504
0.41310	2.48647	-0.19871
0.20261	2.54333	-0.19591
0.00000	2.56577	-0.19504

(al) Page 119

Figure 26.- Concluded.

NASA
National Aeronautics and Space Administration

Report Documentation Page

1. Report No.	2. Government Accession No.	3. Recipient's Catalog No.
NASA CR-4323		

4. Title and Subtitle	5. Report Date
Prediction of Subsonic Vortex Shedding From Forebodies With Chines	September 1990
	6. Performing Organization Code: 820/C
7. Author(s): Michael R. Mendenhall and Daniel J. Lesieutre	8. Performing Organization Report No.: TR 391
	10. Work Unit No.: 505-68-71-03
9. Performing Organization Name and Address: Nielsen Engineering and Research, Inc., 510 Clyde Avenue, Mountain View, CA 94043	11. Contract or Grant No.: NAS1-17077
	13. Type of Report and Period Covered: Contractor Report
12. Sponsoring Agency Name and Address: National Aeronautics and Space Administration, Langley Research Center, Hampton, VA 23665-5225	14. Sponsoring Agency Code

15. Supplementary Notes
NASA Langley Research Center
Technical Monitor: Robert M. Hall

16. Abstract
An engineering prediction method and associated computer code VTXCHN to predict nose vortex shedding from circular and noncircular forebodies with sharp chine edges in subsonic flow at angles of attack and roll are presented. Axisymmetric bodies are represented by point sources and doublets, and noncircular cross sections are transformed to a circle by either analytical or numerical conformal transformations. The lee side vortex wake is modeled by discrete vortices in crossflow planes along the body; thus the three-dimensional steady flow problem is reduced to a two-dimensional, unsteady, separated flow problem for solution. Comparison of measured and predicted surface pressure distributions, flow field surveys, and aerodynamic characteristics are presented for noncircular bodies alone and forebodies with sharp chines.

17. Key Words (Suggested by Authors(s))
Vortex shedding
Circular bodies
Noncircular bodies
Discrete vortices
Chine forebodies

18. Distribution Statement
Unclassified—Unlimited

Subject Category 02

19. Security Classif. (of this report)	20. Security Classif. (of this page)	21. No. of Pages	22. Price
Unclassified	Unclassified	176	A09

NASA FORM 1626 OCT 86
For sale by the National Technical Information Service, Springfield, Virginia 22161-2171
NASA-Langley, 1990